

INFORMATION TO USERS

This manuscript has been reproduced from the microfilm master. UMI films the text directly from the original or copy submitted. Thus, some thesis and dissertation copies are in typewriter face, while others may be from any type of computer printer.

The quality of this reproduction is dependent upon the quality of the copy submitted. Broken or indistinct print, colored or poor quality illustrations and photographs, print bleedthrough, substandard margins, and improper alignment can adversely affect reproduction.

In the unlikely event that the author did not send UMI a complete manuscript and there are missing pages, these will be noted. Also, if unauthorized copyright material had to be removed, a note will indicate the deletion.

Oversize materials (e.g., maps, drawings, charts) are reproduced by sectioning the original, beginning at the upper left-hand corner and continuing from left to right in equal sections with small overlaps. Each original is also photographed in one exposure and is included in reduced form at the back of the book.

Photographs included in the original manuscript have been reproduced xerographically in this copy. Higher quality 6" x 9" black and white photographic prints are available for any photographs or illustrations appearing in this copy for an additional charge. Contact UMI directly to order.

UMI

A Bell & Howell Information Company
300 North Zeeb Road, Ann Arbor MI 48106-1346 USA
313/761-4700 800/521-0600



Photometric Decomposition of NGC 6166

R. Melvin Blake B. Sc.

November 3, 1997

A thesis submitted in partial fulfillment of the requirements for the degree of

Master of Science

Saint Marys University

Halifax, Nova Scotia

©August 1996



National Library
of Canada

Acquisitions and
Bibliographic Services

395 Wellington Street
Ottawa ON K1A 0N4
Canada

Bibliothèque nationale
du Canada

Acquisitions et
services bibliographiques

395, rue Wellington
Ottawa ON K1A 0N4
Canada

Your file *Votre référence*

Our file *Notre référence*

The author has granted a non-exclusive licence allowing the National Library of Canada to reproduce, loan, distribute or sell copies of this thesis in microform, paper or electronic formats.

The author retains ownership of the copyright in this thesis. Neither the thesis nor substantial extracts from it may be printed or otherwise reproduced without the author's permission.

L'auteur a accordé une licence non exclusive permettant à la Bibliothèque nationale du Canada de reproduire, prêter, distribuer ou vendre des copies de cette thèse sous la forme de microfiche/film, de reproduction sur papier ou sur format électronique.

L'auteur conserve la propriété du droit d'auteur qui protège cette thèse. Ni la thèse ni des extraits substantiels de celle-ci ne doivent être imprimés ou autrement reproduits sans son autorisation.

0-612-22790-1

Canada

Contents

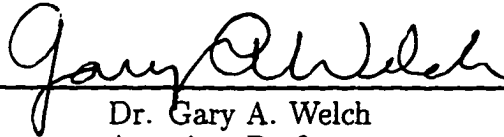
1	Introduction	1
1.1	Properties of cD Galaxies	1
1.2	The Multiple Nuclei of cD Galaxies	2
1.3	NGC 6166: Relevant previous work	4
1.4	The Goals of this Work	8
2	Observations and Photometric Calibration	10
2.1	The data set	10
2.2	Pre-processing	10
2.3	Evaluation of Sky Flatness and Constancy	13
2.4	Preparation of the Sky Flats	14
2.5	Photometric Calibration	16
2.5.1	Transformation Coefficients	16
2.5.2	Calculation of the Transformation Coefficients	17
2.5.3	Comparison with other Extinction and Transformation Coefficients at CFHT	20
2.5.4	Conversion of Surface Photometry to Standard Magnitudes	22
3	Multiple Nucleus Surface Photometry of NGC 6166	23
3.1	Sky Brightness Determination	23
3.2	Testing the Surface Photometry Software	25
3.3	The Final Fitting	32

3.4	The Effect of Sky Error on the Photometry	33
4	Photometry of CFHT Archive images	38
4.1	Motivation for Using Additional Data	38
4.2	Pre-processing and Sky Subtraction	39
4.2.1	Pre-processing of CFHT Archive Data	39
4.2.2	Checking the Flat Fielding	40
4.2.3	Sky Determination	41
4.3	Surface Photometry and Calibration of NGC 6166	
	Archive Images	42
4.3.1	Surface Photometry of the CFHT Archive Images	42
4.3.2	Calibration of CFHT Archive Images	43
5	Aperture Photometry of NGC 6166	46
5.1	Reasons for Performing Aperture Photometry	46
5.2	Performing Aperture Photometry of Nucleus B and C	48
5.2.1	Removal of Unwanted Objects	48
5.2.2	Calculation of Total Magnitudes	49
5.2.3	Calculation of D_n	50
5.3	Photometry of the Tidal Wake Candidate	51
6	Calculation of Dust Mass.	55
6.0.1	Motivation for Calculating the Dust Mass	55
6.0.2	Calculation of Dust Mass for NGC 6166	55

7	Results	58
7.1	Results From Profile Fitting Photometry	58
7.1.1	Averaging the Surface Brightness Profiles	58
7.1.2	Features of the Surface Brightness Profiles	59
7.1.3	Comparison of Surface Brightness Profiles to other Work	60
7.1.4	Position Angle and Ellipticity Profiles	61
7.2	Results From Aperture Photometry	70
7.2.1	Results From D_n Determinations	70
7.2.2	Global Colours Derived from Aperture Photometry.	79
7.2.3	Total Magnitudes and Colours of the Tidal Wake Candidate	82
7.3	Dust Morphology and Mass Estimate.	85
7.3.1	The Dust Morphology of NGC 6166	85
7.3.2	Results of the Dust Mass Calculations	88
8	Conclusions	93
8.1	Summary	93
8.2	Future Work	94
9	Appendix A	103
10	Appendix B	108
11	Appendix C	110

Certificate of Examination

Saint Mary's University
Department of Astronomy and Physics



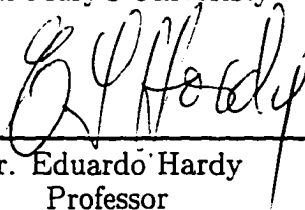
Dr. Gary A. Welch
Associate Professor
Department of Astronomy and Physics
Saint Mary's University
(Supervisor)



Dr. Malcolm N. Butler
Associate Professor
Department of Astronomy and Physics
Saint Mary's University



Dr. David A. Clarke
Associate Professor
Department of Physics and Astronomy
Saint Mary's University



Dr. Eduardo Hardy
Professor
Department of Astronomy and Physics
Laval University
(External Reader)

Photometric Decomposition of NGC 6166

Melvin Blake August 1996

Abstract

We have used CFHT observations in Cousins B and R to probe the structure of the supergiant elliptical galaxy NGC 6166 in Abell 2199. We utilize the isophotal and aperture photometry of nuclei B and C to search for evidence of dynamical interactions with the central galaxy. In addition, we have investigated the dust component of the central galaxy.

The results from our photometry are consistent with the NGC 6166 system being composed of the large central cD galaxy, nucleus A, and two cluster galaxies passing through the center of the cluster. Nucleus B and C show none of the ellipticity or position angle changes, expected if these galaxies are being cannibalised. In addition, nucleus C has an average $B - R = 1.75 \pm 0.15$ which is bluer than nucleus B, which has a $B - R = 1.90 \pm 0.22$. This confirms the previous observations of Lachiéze-Rey et al. (1985). The color of nucleus C, while not ruling out it being a stripped Sb galaxy, is more consistent with it being an elliptical.

The computed dust mass of the central galaxy is $\sim 7.0 \times 10^5 M_\odot$ from optical absorption, and $2.7 \times 10^7 M_\odot$ from IRAS fluxes. The dust mass is high, in any event, and is more like that of a spiral galaxy. This supports the results of Goudfrooij & de Jong (1995) that the IRAS fluxes for ellipticals give dust masses systematically higher by a factor of ten over optical absorption techniques. Our result therefore adds support to their suggestion that the additional dust is in a diffuse component which

is not part of discrete dust clouds. This would seem to be true even for the most massive galaxies.

A Monte Carlo simulation shows that the tidal feature indicated by Lauer is not likely to be a projected cluster galaxy. Its colors $B - R = 1.52 \pm 0.37$ are consistent with it being formed from the halo of Nucleus A which, at the distance of the wake has $B - R = 1.75 \pm 0.07$. The overdensity of this feature computed from our brightness information are consistent with a crude calculation based upon the models of Weinberg (1986) for dynamical wakes. The system, it must be concluded, is physically interacting, but does not represent a bound system with the central galaxy cannibalising its neighbours. The lack of significant structural changes in Nucleus B and C suggest a system in the early stages of merger.

List of Figures

1	A 900 second R-band image of NGC 6166 identifying nucleus A, B, C and D according to the nomenclature of Minkowski (1961)	5
2	Test of the accuracy of SNUC when galaxy centers are a free parameter	27
3	SNUC accuracy when the galaxy is fitted over the entire image and when the center and radius are marked.	29
4	SNUC accuracy when the galaxy is fitted over a boxed region.	30
5	SNUC accuracy when the number of iterations is varied.	31
6	The effect of a 1% sky subtraction error on the fitted blue magnitudes of a 1200 second B image	35
7	The effect of a 1% sky subtraction error on the fitted ellipticities of a 900 second R image	36
8	The effect of a 1% sky subtraction error on the fitted position angles of a 900 second R image	37
9	B-band major-axis surface brightness profiles for nuclei A, B and C .	62
10	R-band profile for nuclei A, B and C computed from photometry of our CFHT images	63
11	B-band major-axis surface brightness profiles for nuclei A, B and C derived from our CFHT Archive images.	64
12	R-band profile for nucleus A, B and C measured on the CFHT Archive images.	65

13	Comparison of our <i>B</i> -band surface brightness profile for nucleus A to that of Lachiéze-Rey <i>et al.</i> (1985)	66
14	Comparison of our <i>R</i> -band profile to nucleus B Lachiéze-Rey <i>et al.</i> (1985)	67
15	The mean ellipticity profiles of the three nuclei of the NGC 6166 system from our CFHT data.	71
16	The mean position angle profiles of the three nuclei of the NGC 6166 system from our CFHT data.	72
17	Comparison of our mean ellipticity profiles to that of Lauer (1986) . .	73
18	Comparison of our mean position angle profiles to that of Lauer (1986)	74
19	The mean ellipticity profiles measured on our CFHT archive images.	75
20	The mean position angle profiles measured on our CFHT archive images.	76
21	Plot of $\log(D_n/0.1')$ versus corrected total apparent B magnitude for nucleus B and C	78
22	A histogram of the <i>B</i> – <i>R</i> values of spiral bulges and elliptical galaxies.	81
23	A comparison of the Johnson <i>B</i> – <i>R</i> colour of Nucleus B and C to ellipticals of the same absolute B magnitude.	83
24	A map of all pixels surviving the dust selection process	89
25	A histogram comparing the IRAS dust mass for spirals and ellipticals.	92
26	The geometry used for the determination of the galaxy contribution to the sky value	111

List of Tables

1	Results of Dome Flat Fielding Tests	13
2	Sky Flat Field Test Results	16
3	Transformation and Extinction Coefficients	21
4	Adopted Sky Brightnesses	24
5	V-Band Flat Field Test Results	41
6	Adopted Sky Brightnesses	42
7	Data for Calibration of Archive Images	45
8	Results of D_n Determinations	77
9	Global Colours of Nucleus B and C	79
10	Global Magnitudes and Colours of the Tidal Wake Candidate	82
11	Properties of Detected Dust Features	86
12	Night 1 May 3/4 1984 Observations	103
13	Night 2, May 4/5 1984	105
14	Detailed information on CFHT Archive data	107
15	M92 Standard Star Data	108
16	NGC 4147 Standard Star Data	109
17	Sky Region Semi-Major Axis Positions	113
18	Adopted Sky Values	115

1 Introduction

1.1 Properties of cD Galaxies

The largest galaxies in the universe are the cD galaxies. Attention was first drawn to these objects by Mathews, Morgan & Schmidt (1965) in their attempt to identify the optical counterparts to radio sources. Many of the radio sources were associated with the D galaxies, which are giant galaxies with elliptical-like cores surrounded by large extended envelopes. The cD galaxies are a special subclass of the D galaxies which were found to dominate the centers of rich Abell clusters. They were much larger than other D galaxies.

Other properties of these galaxies were also intriguing. Nearly 50% of the cD galaxies contained multiple nuclei; (Morgan & Lesh 1965; Schneider, Hoessel & Gunn 1983). cD galaxies are also *never* found in the field, although some candidate cD galaxies have been identified in poorer clusters (Morgan, Kayser & White 1975). Whatever the origin of cD galaxies, a cluster environment seems to be required for the formation of a cD galaxy. The cD galaxies also seem to be related to the global properties of their host clusters. Struble & Rood (1982) showed that cD galaxies were found in more symmetric, centrally concentrated clusters. They suggested that cD galaxies were found in the more dynamically evolved environments assuming the symmetry and central concentration of the clusters represent advanced dynamical evolution. These clusters also have large X-ray luminosities and large cooling flows which may be depositing hundreds of solar masses per year of material into the center of the clusters. cD galaxies are also seen to be connected to large scale matter

distributions in the universe. A number of authors (eg. Porter *et al.* 1991; West 1995 and references therein) have found that the major axes of cD galaxies align with the major axes of their host clusters as well as “pointing” to the nearest neighbouring clusters.

Various theories have been proposed for the formation of cD galaxies. The large number of multiple nuclei led Ostriker & Hausman (1977) and Hausman & Ostriker (1978) to suggest that the formation of cD galaxies takes place through galactic cannibalism, as smaller galaxies merge with the central galaxy in the cluster core. Merritt (1984) has proposed that the cD galaxies start out as normal ellipticals, but because of their position at the center of their clusters, they build up as material is tidally stripped from galaxies passing through the cluster center. Meanwhile Sarazin (1988) and Silk *et al.* (1986), have suggested that if the large cooling flows are long lived, then the flows may have been able to build up most of the mass of the cD galaxies over the Hubble time.

1.2 The Multiple Nuclei of cD Galaxies

In this work we are interested in addressing the possibility of formation of cD galaxies through galactic mergers. In particular, we wish to address the question of whether the multiple nuclei seen in many cDs are simply chance projections of foreground or background galaxies, or if they instead represent current mergers of the central giant cDs with neighbours in the cluster.

The origin of multiple nuclei has been debated for many years. According to one view, most of the multiple nuclei could be easily explained simply by chance

projections of cluster galaxies onto the cDs; (Rood & Leir 1979; Tonry 1985b; Beers & Tonry 1986; Merrifield & Kent 1991; Blakeslee & Tonry 1992). Theoretical studies provide arguments to support this case. For instance, White (1976) performed N-body simulations of merging galaxies which showed that bound elliptical orbits of secondary nuclei will quickly become circular. The result is that the velocities of the nuclei relative to the larger galaxies will decrease. Radial velocity measurements of multiple nuclei (Mikowski 1961; Tonry 1985b) showed that the velocities of the multiple nuclei of cD galaxies relative to the central galaxies were high, around 800 km/s which is comparable to the global velocity dispersion of the clusters. This argues against the multiple nuclei representing galaxies merging with the cDs.

Conversely, there are those who claim that the multiple nuclei represent the present-day mergers of the supergiant ellipticals with those neighbours which come close enough to be captured (Oemler 1976; Ostriker & Hausman 1977 ; Hausman & Ostriker 1978; Lauer 1986, 1988; Bothun & Schombert 1990). According to this argument, cD galaxies started out as normal ellipticals, but because of their position at the center of their respective clusters they grew to their present large sizes through mergers. Theoretical and observational work by Tonry (1985a) showed that the high relative velocities do not necessarily argue against the multiple nuclei being merging galaxies. Tonry (1985a) showed that the orbits of a galaxy completely imbedded in the halo of a larger galaxy will not undergo stronger tidal gravity near perigalacticon than apogalacticon; this was the mechanism which circularizes the orbits in the simulations of White (1976). The models of Tonry (1985a) showed that only a small

percentage of the orbits become circular. Tonry (1985b) measured the relative velocities of a large number of multiple nuclei. He found that the binned distribution of the velocities was best fit by a double Gaussian distribution, with one peak at 300 km/s and one at 800 km/s. The distribution of relative velocities was consistent with 30% of the nuclei being projections, 20% being on circular orbits and 50% being on elliptical orbits. This agreement between the theoretical and observational predictions argued in favor of the multiple nuclei being galaxies merging with the cDs.

1.3 NGC 6166: Relevant previous work

One of the largest cD galaxies is NGC 6166. When Morgan & Lesh (1965) defined the cD galaxies, NGC 6166 was considered to be an archetypal cD galaxy, and they in fact used the properties of NGC 6166 to define the class. NGC 6166 dominates the center of the cluster Abell 2199, and is the brightest galaxy in that cluster. Abell 2199 is a Bautz-Morgan class I cluster with a cooling flow and is spherical and centrally concentrated. NGC 6166 is also associated with the radio source 3C338, an unusual jet-like radio source (Burns *et al.* 1983; Feretti *et al.* 1993).

The first examination of NGC 6166 was done in the pioneering study of Minkowski (1961). This was the first study to identify the three distinct components in the center of NGC 6166 which Minkowski labeled A, B and C, (a fourth component, D, was identified by Minkowski as a probable foreground star). We adopt his nomenclature for simplicity and ease of comparison with other work. Figure 1 shows one of our R-band images of NGC 6166 obtained at the Canada-France-Hawaii telescope with the four nuclei identified by Minkowski labeled. Minkowski (1961) also noted the high

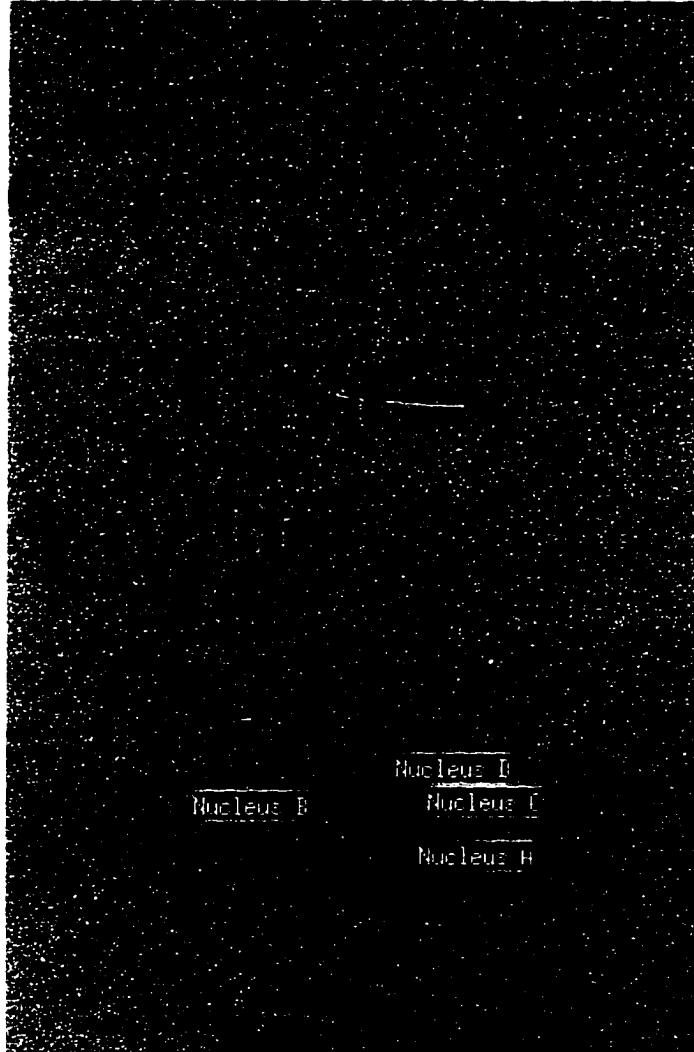


Figure 1: A 900 second R-band image of NGC 6166. Nuclei A, B C and D are identified according to the nomenclature of Minkowski (1961). The field shown is 2.'44 by 3.'9, and North is to the left, east is towards the bottom.

relative velocities of the nuclei and the presence of a dust lane in the center of the central galaxy, Nucleus A.

There have been a number of other studies done of NGC 6166. Oemler (1976) performed a photographic study in B and V. This work showed the large size of the envelope of the NGC 6166 and provided a profile reaching to 360Kpc. Gallagher, Faber & Burstein (1980) performed photoelectric aperture photometry of several normal elliptical galaxies, and NGC 6166. The colour profile shows a strong colour gradient. The halo of the cD galaxy is bluer than its center, and also bluer than the other ellipticals in their sample. These authors suggested that this colour gradient is consistent with NGC 6166 being built up by mergers with smaller, bluer companions.

The previously cited studies focused on global characteristics of the cD galaxy itself, ignoring the secondary nuclei. The first study of NGC 6166 which attempted to study the properties of its multiple nuclei was the spectroscopic work of Tonry (1984) who measured the internal velocity dispersions of nuclei A, B and C. He found that the internal velocity dispersions of nuclei B and C were inconsistent with them being on bound circular orbits around nucleus A. In addition, the mass to light ratios (M/L) for the nuclei were found to be $15.3M_{\odot}/L_{\odot}$, $10.0M_{\odot}/L_{\odot}$ and $15.0M_{\odot}/L_{\odot}$ for nuclei A, B and C respectively, which are typical of normal ellipticals.

Lachi ze-Rey *et al.* (1985) made the first attempt at the photometric decomposition of the components of NGC 6166, based on CCD images in the b and r passbands of the Gunn system. An iterative technique was used to model the light of the central galaxy, which they assumed could be fit by elliptical, symmetric isophotes centered

on nucleus A. Nuclei B and C were masked out during this procedure. The model was then subtracted from the images to leave B and C isolated, which were then examined separately. Global colours and brightness and colour profiles were calculated for all three nuclei. Nucleus A showed a strong increase in ellipticity with radius. The brightness profiles showed that nucleus B appeared to be a tidally truncated satellite galaxy of nucleus A. Based upon the global colours and increasingly blue colour with radius, they suggested nucleus C could be a cluster spiral projected upon the central galaxy.

Perhaps the most important study of NGC 6166 is the work of Lauer (1986) using a single Gunn g-band image. Lauer used a non-linear least-squares algorithm to fit the light from the three nuclei at all pixels. This strategy has the advantage that, other than the assumption of elliptical isophotes, the position angles and ellipticities of the components of a multiple nucleus system are allowed to vary as free parameters. In addition, no masking of pixels of the overlapping galaxies is needed and so all the information on the images is utilized. All three galaxies were fit to a de Vaucouleurs profile, which provided good descriptions of nuclei A and C. Nucleus B, however, appeared to be tidally truncated. In addition no significant isophote twisting or ellipticity changes were seen in nuclei B and C. The large ellipticity changes observed in nucleus A by Lachiéze-Rey *et al.* (1985) were verified. An elongated feature was seen in the residual map after a model based upon the fits was subtracted. Lauer speculated that his feature was a tidal wake caused by the passage of nucleus B through the envelope of A. Large areas of dust absorption were seen in the residual

maps as well. The sinusoidal dust lane identified by Minkowski (1961) was identified, in addition to a larger region of possible dust absorption to the North of the center of Nucleus A. However, since only a single passband was used, no information on the colours of the nuclei could be obtained. No colours of the tidal wake candidate or dust mass could be computed.

1.4 The Goals of this Work

The previous studies of NGC 6166 are limited. Lauer (1986) used a superior algorithm and presents the best attempt to date to determine the structure of nuclei B and C. However, the best photometric effort is that of Lachi ze-Rey *et al.* (1985) which provided the best information on the photometric properties by using $B - R$ colour information. However, their algorithm is limited and does not use all the information on the images. Neither their study, nor that of Lauer (1986) provide information on the colours of the tidal wake or the dust mass.

We build upon both these studies by combining the superior fitting algorithm of Lauer (1986) with the advantages of using colour information in studying the NGC 6166 system. We therefore will use observations in the Cousins B and R filters to determine the mean colours of the nuclei. This should confirm if nucleus C is indeed a spiral galaxy. The work of Lachi ze-Rey *et al.* (1985) used a single image in each passband. We use multiple images in each passband to provide multiple measurements of the position angles, ellipticities, colours and magnitudes of the components of NGC 6166. This provides the advantage that we can average the results to provide a better indication of the uncertainties in our results. We will also provide the first colour

study of the tidal wake candidate to determine if its properties are consistent with a tidal feature. Finally, to address the possibility the nucleus C might be a spiral galaxy stripped of its disk, we will compute a dust mass for the galaxy. We then compare the dust mass to that of a typical spiral galaxy.

2 Observations and Photometric Calibration

2.1 The data set

The data used in this study were obtained by G. A. Welch using the Canada-France-Hawaii Telescope atop Mauna Kea on the nights of May 3/4, 4/5 1984. Cousins B and R filters were used to take the observations and employ a RCA 320X512 CCD. The field of view at prime focus of the CCD was 2'.44 by 3'.9. Observations in both passbands were made of NGC 6166 and sky regions offset by 10'. For photometric calibration, standard star sequences were imaged in the globular clusters NGC 4147 and M92 (Christian *et al.* 1982; Davis 1989). Bias, dark and dome flat images were taken to correct for the readout bias pattern, dark current and detector response variations respectively. The complete log of observations is given in Tables 12 and 13 in Appendix A.

2.2 Pre-processing

Pre-processing of CCD images involves the removal of a DC offset, bias pattern, dark current and pixel-to-pixel sensitivity variations from the “raw” images (Gilliland 1992). First the value of the DC offset is determined from overscan regions on each image. Second the bias pattern is subtracted using the median of many zero second exposure images. The bias pattern is described by Gilliland (1992) as a “stationary, two-dimensional, additive background” which is repeated for each readout of the CCD. Thermal oscillations in the atoms of silicon which make up the CCD chip will cause the chip to collect current even when the chip is not exposed to light. This

“dark current” is linearly dependent upon time. The third pre-processing step is to subtract the dark current using a “dark frame”, which is a long-exposure time image taken in the absence of light. Finally, a uniform source is imaged and the sensitivity variations of the pixels removed by dividing this “flat” image into the program images. This is done to ensure that we measure the light at the same sensitivity levels on all the pixels in order to perform surface photometry. These reductions were performed using the **VISTA** package. The pre-processing steps were performed on the standard star frames as well as the images of NGC 6166 and nearby sky regions.

The DC offset was determined using an “overscan region” in the last 15 rows of the raw image. The overscan region is created by reading out the chip past the last rows and columns containing astronomical data. This results in a region on the image which contains only the DC offset. Bad pixels in the overscan region were identified on the image display and masked out. Overscan regions were then trimmed from the images.

The second step is to remove the bias pattern. The bias pattern is removed by subtracting the median value of each pixel on a number of bias frames – zero-second exposures containing only the bias pattern. Twenty-nine bias images were combined using the **MEDIAN** program in **VISTA**. This program gives each pixel on the final image its median value from all the frames. The median is more representative of the true value for the pixel than the mean. This is due to the fact that the mean is affected by spurious high or low pixel values. Small numbers of spurious data do not affect the median significantly. The median is therefore less affected by a few cosmic

ray hits than the mean.

The third pre-processing step involves dark current subtraction. A median dark frame was computed from 19 dark frames, and subtracted from all images except the bias images. The dark current is linearly dependent on time. Therefore, before subtraction the median dark frame was first multiplied by the ratio of the exposure times of the program image and the dark image. It should be noted here that one third of the dark images (11 out of 30) were rejected. The rejected images exhibited excess charge near the edges along the columns. The origin of these features is uncertain. The affected regions were concentrated in the first 20 rows and the first 30 columns of the chip. As suggested in Section 3, errors in dome flat fielding may have been caused by these charge excesses. The median dark image was calculated from images *least* affected by these contaminating features. Re-examination of the median bias frame showed excesses of 2% in the affected regions.

The next pre-processing step is correction of pixel-to-pixel sensitivity variations. A flat image is an image of a uniform source (in this case the inside of the dome). This enables the correction of sensitivity variations among the pixels of the CCD. The median dome flat image was computed from all the flats for each passband (12 *B*-band and 13 *R*-band flats). Separate processing of *B* and *R* flat images is necessary because sensitivity variations among the pixels of a CCD are known to be wavelength-dependent. The mean of the median dome flat image was computed before performing the flat field division. The ratio of the program image and the median dome flat was then scaled by the mean of the flat image. This ensures the mean of the program

images is preserved. Flat fielding was performed on all NGC 6166 and standard star images.

2.3 Evaluation of Sky Flatness and Constancy

In order to measure only the light from the galaxy, a value for the sky brightness must be subtracted from the NGC 6166 images. For this purpose, blank sky regions were imaged during the observations. However, we must first test that the mean sky value does not change from image to image. This was done by creating five boxes scattered on the blank sky images. Each box was 50 pixels square and each was examined on the display to ensure absence of visible stars or galaxies. Each box was also cleaned of cosmic rays using a boxcar median filter. The mean of the values inside each box was then calculated and the average values for all the boxes was then adopted as the average value for each sky frame. The results are shown in Table 1.

Table 1: Results of Dome Flat Fielding Tests

Image	Region	Filter	Box 1	Box 2	Box 3	Box 4	Box 5	Average Value	σ
162	Sky 1	<i>R</i>	735.83	758.12	747.33	747.30	756.83	749.08	3.83
259	Sky 1	<i>R</i>	481.55	492.49	488.24	486.28	492.52	488.22	1.96
269	Sky 2	<i>R</i>	528.23	534.64	517.62	530.97	533.23	528.94	2.71
163	Sky 1	<i>B</i>	244.00	232.29	229.93	228.35	232.10	229.33	3.39
258	Sky 1	<i>B</i>	191.72	198.48	196.98	195.66	198.26	196.22	1.19
267	Sky 2	<i>B</i>	423.15	429.43	425.35	427.72	424.83	426.10	1.03
277	Sky 2	<i>B</i>	200.71	204.77	203.02	196.47	202.33	201.46	1.26

Since all *B*-frames are 1200 second exposures, and all *R*-frames are 900 seconds,

it is clear that there is a problem: the sky values for the R frames vary by about 40% from one night to the next, and also during the night. It must be concluded that the actual sky brightness is changing from image to image and that these values cannot be used for sky subtraction from the NGC 6166 images. We describe the determination of the sky brightnesses in Section 3.1.

These data also provide a check upon the dome flat fielding process. The variation of the mean values in the boxes shows 10% variation around the images. The sky value should be nearly constant over the small field of view of the images. This indicates that the flat fielding should be improved. Examination of sky images under high contrast showed a possible cause of the variations. The regions which contained brightness enhancements (see Section 2.3) on the bias and dark frames were systematically fainter than other regions on the sky images. This may be explained if the images were over-subtracted by the dark frame and end up systematically fainter as a result. We blinked the dome flat images with the median dark frame and verified that the regions of excess charge on the dark frame corresponded to the fainter regions of the sky images. The pattern was also the same in both passbands, which would not be the case if the effect was due to real sky variations. With this evidence, the decision was made to process our NGC 6166 images further using sky flat field images.

2.4 Preparation of the Sky Flats

A sky flat image is used when the dome flat images do not adequately remove pixel-to-pixel variations. A sky flat is required when large scale variations in the sky

background occur within an image after normal pre-processing. This effect is clearly seen in Table 1. Images of blank sky images taken during the observations were used to remove residual background variations.

As many sky frames as possible were needed to help eliminate contributions from galaxies and stars and reduce the Poisson noise in the final sky flat image. Additional blank sky images near the cD galaxy in Abell 1413 were combined with the NGC 6166 sky images to compute the median sky flats. These additional blank sky images were obtained during the same run as the NGC 6166 data. The Abell 1413 region sky frames were pre-processed in an identical manner to the NGC 6166 images. On all the sky images there are bad columns and, more importantly, field stars and galaxies. Here the Abell 1413 data are particularly valuable. The blank sky images near Abell 1413 and NGC 6166 have no common foreground stars or galaxies. (Taking the median of the two sets of images is therefore very effective at eliminating any unwanted objects.)

On highly stretched displays of the images all field stars, galaxies and cosmetic defects were identified. In order to eliminate these, the regions containing the features to be removed were replaced by interpolations using a first order polynomial. A boxcar filter of width 20 pixels was used to smooth the entire image further. The 20 pixel boxcar median filter was selected since it was twice the size of the largest unwanted feature. The median was calculated of all sky frames so prepared. The calculation of the median was scaled by the means of the images. This procedure yielded a set of sky images with the unwanted features eliminated. No traces of enhancements at

Table 2: Sky Flat Field Test Results

Image	Region	Filter	Box 1	Box 2	Box 3	Box 4	Box 5	Average Value	σ
162	Sky 1	<i>R</i>	748.61	748.28	747.84	750.23	749.15	748.82	0.37
259	Sky 1	<i>R</i>	488.45	487.54	487.39	488.06	486.06	487.50	0.38
269	Sky 2	<i>R</i>	529.01	529.98	529.16	529.98	530.63	529.75	0.28
163	Sky 1	<i>B</i>	228.77	229.02	228.46	228.87	229.07	228.84	0.09
258	Sky 1	<i>B</i>	196.01	194.97	195.89	196.11	195.33	195.66	0.20
267	Sky 2	<i>B</i>	429.03	428.45	428.02	424.47	425.75	427.20	0.80
277	Sky 2	<i>B</i>	200.76	200.63	201.43	200.53	201.67	201.00	0.21

the position of stars and galaxies were seen on the display of the median sky flats for either filter. The original pre-processed sky and galaxy frames were flat fielded with the median sky flat images.

To determine if the sky variation on the images had been reduced, the mean brightness of blank sky regions on the sky frames was determined. For five regions, (not the same as those used previously) the mean values are shown in Table 2. It is clear that the sky background values are changing from image to image and night to night. However, the additional flat-fielding step has reduced the variation of the sky brightness on any individual frame to $\pm 1\%$.

2.5 Photometric Calibration

2.5.1 Transformation Coefficients

In order to compare surface photometry derived in this study to other work it is essential to transform the instrumental system of the observer to a standard astro-

nomical magnitude system. Stars with well known standard magnitudes and colours, taken from Christian et al. (1982) and Davis (1989), were observed during the night and used to calibrate the photometry. VISTA uses the following system of linear equations to accomplish this :

$$R = r + k_r \times X + T_r \times (B - R) + Z_r \quad (1)$$

$$B = b + k_b \times X + T_b \times (B - R) + Z_b \quad (2)$$

In these equations R and B are the standard magnitudes of a photometric standard star having instrumental magnitudes r and b respectively, X is the airmass of the observation, k_r and k_b are the extinction coefficients in R and B , T_r and T_b are colour coefficients for each passband, $(B - R)$ is the standard colour index for each star, and Z_r and Z_b are the photometric zero points in each passband. These enable one to correct for the atmosphere (extinction coefficients) and the instrumental sensitivities (transformation coefficients). One should note that, in equations 1 and 2, the standard magnitude appears on the left side. This particular formulation results in extinction coefficients which are negative, whereas traditionally they are positive.

2.5.2 Calculation of the Transformation Coefficients

The standard magnitudes and colours for the standard stars observed are given in Appendix B. These have been taken from Christian *et al.* (1985) and Davis (1989). On the night of May 3/4 the NGC 4147 field was observed three times, while the M92

field was observed twice. On May 4/5 both were observed at three different times.

The following procedure was used to determine the instrumental magnitudes of the standard stars. First a point spread function (PSF) was determined for each image using the brightest stars on the images. These PSFs model the light of the stars so that companions to the standard stars can be subtracted from the images. With the companion stars subtracted, synthetic aperture photometry was performed on the brightest stars to determine the variation of magnitude with aperture radius for each image – the aperture growth curve. The standard stars were then isolated on the images by using the PSF to remove all other stellar objects from the image. Synthetic aperture photometry was then performed on the standard stars. To obtain total magnitudes of the standard stars the growth curve was used to extrapolate the aperture magnitudes 20 pixels past the last measured aperture. The extrapolated magnitudes were then scaled to a one second exposure time and used to solve for the transformation and extinction coefficients using equations 1 and 2.

Defining a PSF is an iterative procedure which uses the DAOPHOT program of Stetson (1987), as implemented in VISTA. The program PSF within DAOPHOT was used to determine the PSF, which consists of a model (a bivariate Gaussian) and a lookup table of residuals from the model. DAOPHOT scales the PSF to model the brightness of each star. The SUB* program uses this model to subtract the light of stellar objects. We subtracted all stellar objects except the standard stars.

Well isolated stars were picked to derive the PSFs in order to eliminate any distortion caused by neighbours. These PSF stars were not necessarily the standard stars;

the criteria for selection was that a star not have another star within 15 pixels and that it be among the brightest on the frame. For the creation of the PSFs **DAOPHOT** requires three input parameters: (1) a stellar full-width-at-half-maximum (FWHM); (2) a fitting radius, defined as the radius used to fit the Gaussian model; (3) a PSF radius, which defines the extent of the stars (in practice the radius of the brightest star on the image). The derivation of the PSF usually took three iterations. First the PSF stars on each image were identified along with their companions. All other stars were subtracted off and a new, presumably better, PSF was defined. Any stars missed were then added to the list of known stars. After around three iterations, a PSF was judged “satisfactory” by examining a frame with all the PSF stars subtracted.

We then determined the aperture growth curves for the images. All but the brightest stars on all the images were subtracted using the **SUB*** program of **DAOPHOT**. Aperture photometry was performed on these stars. The results were entered into the stand-alone program **DAOGROW** (Stetson 1990) which uses the aperture growth curve method (Howell 1989) to derive magnitudes for stellar objects. The **DAOGROW** routine uses the model of King (1971) to describe the growth curve. The model consists of the sum of three functions: a Gaussian, a Moffat function and an exponential. From the growth curve the total magnitude of a star can be estimated. We take the magnitude of the star within an aperture 20 pixels larger than the last fitted aperture as its total magnitude for the purpose of computing the photometric calibration. All stars but the standard stars were subtracted using **SUB*** and aperture photometry performed on the standard stars. The aperture growth curve for each frame was used

to determine the instrumental magnitudes for use in equations 1 and 2.

The final instrumental magnitude was then entered into the **MAGAVER** routine in **VISTA**, which scales all the observed magnitudes to an exposure time of 1 second. **MAGAVER** also formats the data for input into the **FITSTAR** program of **VISTA**. **FITSTAR** is responsible for the calculation of the transformation and extinction coefficients of equations 1 and 2.

FITSTAR can include extra terms other than the ones shown in equations 1 and 2 but it was decided not to use these terms; they were constrained to have values of zero during the fitting process. Constraining these terms is justified because solutions in which they are included find them to be insignificant. Additional input parameters are the names of the passbands used, and a table containing the standard colours and magnitudes for each standard star in the data set. **FITSTAR** computes the coefficients and plots the residuals. Points which are clearly spurious may then be eliminated before final coefficients are calculated. Plots of the final residuals versus airmass, color, Time (julian Date) and magnitude showed no apparent systematic trends. The extinction and transformation coefficients are given in Table 3.

2.5.3 Comparison with other Extinction and Transformation Coefficients at CFHT

P. Durrell (1995) kindly supplied values of corresponding coefficients for a run at CFHT, and we use these and values from the MOS/SIS manual (Welch 1995) as an initial check upon our procedure. For a three night run Durrell obtains values of *B*-band extinction coefficients of -0.091 , -0.070 , and -0.130 , with uncertainties

Table 3: Transformation and Extinction Coefficients

Coefficient	Night 1	Night 2
k_r	$-0.090 + / - 0.006$	$-0.132 + / - 0.004$
T_r	$-0.022 + / - 0.002$	$-0.042 + / - 0.002$
Z_r	$-2.654 + / - 0.008$	$-2.583 + / - 0.005$
k_b	$-0.206 + / - 0.009$	$-0.246 + / - 0.006$
T_b	$0.090 + / - 0.002$	$0.072 + / - 0.002$
Z_b	$-2.215 + / - 0.011$	$-2.150 + / - 0.008$

between 0.03 to 0.07. In the R -band Durrell finds values of -0.181 , -0.152 and -0.335 respectively for the same nights. Uncertainties here are between 0.03 to 0.07 magnitudes. The MOS/SIS manual for the CCD camera gives typical extinction coefficients of -0.3 and -0.08 in B and R passbands respectively. Our results indicate that the extinction in the B passband is greater than the extinction in R . This differs from the Durrell data, but agrees qualitatively with the manual values. The extinction in the blue passband is expected to be greater than for the red, since shorter wavelength light is more affected by absorption and Rayleigh scattering in the atmosphere.

The colour coefficients T_r and T_b quoted from Durrell are 0.129 in B and 0.006 in R , while the MOS/SIS manual gives 0.04 and 0.05 respectively. Our colour coefficient for the R -band is negative in sign to these results. We find that the absolute value the B colour coefficient less than that of R , which is also true for the Durrell and MOS/SIS manual as well.

Based upon these comparisons we find that our extinction coefficients seem typical

of CFHT, and are qualitatively consistent with the known absorption and scattering affects of the atmosphere. However, the Durrell data are in conflict with what is physically expected. It is difficult to compare our transformation coefficients to those of Durrell or the MOS/SIS manual, since these should depend more upon the detector and filter set used than the photometric conditions. These comparisons give us confidence in our results, although it is clear the transparency of the atmosphere, as measured by the extinction coefficient, was greater on the first night of observation.

2.5.4 Conversion of Surface Photometry to Standard Magnitudes

We must solve equations 1 and 2 for the standard B and R magnitudes in terms of observational quantities only. We find:

$$B = \frac{(1 + T_r)(b + k_b \times X + Z_b) - k_b(r + k_r \times X_r + Z_r)}{1 + T_r - k_b - 2 \times T_r \times k_b} \quad (3)$$

$$R = \frac{1}{(1 + T_r)} \frac{1}{(r + k_r + T_r \times B + Z_r)} \quad (4)$$

We must also note that **DAOPHOT** computes instrumental magnitudes from the intensities through

$$m = 25.0 - 2.5 \log(I) \quad (5)$$

where I is the intensity and the factor of 25.0 originates from the zero point shift used in the **DAOPHOT** program. The galaxy intensities are first scaled to one second exposure times. Thus using equations 3, 4, and 5, and the airmass we can transform surface photometry to those of the Cousins photometric system.

3 Multiple Nucleus Surface Photometry of NGC 6166

3.1 Sky Brightness Determination

We must subtract the sky value before doing surface photometry on the NGC 6166 images. We have already found in Section 2.2 that the blank sky images cannot be used for this purpose. This means we must determine the value of the sky background from each NGC 6166 image. We must choose a sky region far as possible from the galaxy. Unfortunately the halo of the galaxy is large and unavoidably makes a contribution to the brightness values in all pixels of the images. If the galaxy contribution to the sky region brightness is not removed, we will truncate the profiles of the nuclei. We want to subtract only the true sky value from the NGC 6166 images. The true sky value is the brightness remaining after the galaxy contribution to the mean brightness of the sky region is removed.

The detailed method for determination of the sky brightness is given in Appendix C. The method is briefly summarized here. We assume as a first approximation that the galaxy isophotes are concentric ellipses of constant ellipticity, and position angle. We also adopt the brightness profile of Oemler (1976) to estimate the relative brightness of the galaxy at any two points along the major axis. A sky region was chosen near the bottom of the images, as far as possible from the galaxy. The center of the sky region and the galaxy nucleus define a line whose length is easily computed. It is also straight forward to compute the angle between this line and the major axis. The expression for an ellipse in polar coordinates gives the major axis length of the

Table 4: Adopted Sky Brightnesses

Image	<i>Sky</i> (ADU)
161	706.4
164	249.9
255	234.5
257	213.9
260	512.6

isophote which passes through the center of the sky region. Brightness ratios may then be computed from Oemler's photometry for any two points along the major axis. These two points are chosen to be a point near the galaxy center where sky is insignificant and the center of the sky region. The brightness ratio and instrumental brightnesses at these two points enable the galaxy contribution in the sky region to be computed. The estimated galaxy contribution to the sky is subtracted from the raw brightness to give the adopted sky brightness, which is then subtracted from all pixels. The adopted sky brightnesses are given in Table 4.

Our sky region center typically lies on the isophote with semimajor axis length of $160''0$, while the sky region of Lauer (1986) lies near $150''0$. However Lauer (1986) makes no attempt to eliminate the galaxy contribution to the brightness of the sky region. Our sky estimate should therefore be more free of galaxy contamination than that of Lauer (1986). We discuss the effects of error in sky values on the surface photometry in Section 3.4.

3.2 Testing the Surface Photometry Software

In order to study the components of NGC 6166 we utilized the **VISTA** program **SNUC** which is essentially the multiple nucleus fitting routine of Lauer (1986). **SNUC** is flexible and offers various options to the user to modify the fitting process. We use model images to test the effects of the various options on the fits performed by **SNUC**. Since the input parameters of the model galaxies are known, we can use the various options in the **SNUC** program to obtain the best possible fit to the models and these can then be used to fit the program images.

The **IRAF** routine **MKOBJECT** was used to create realistic de Vaucouleurs model galaxies with which to test the accuracy of **SNUC**. **MKOBJECT** takes the centroids, ellipticities and position angles of any number of de Vaucouleurs profile galaxies including the Poisson noise. Initial tests upon a single noise-free model galaxy showed **SNUC** to be reliable in all but the outermost regions. **SNUC** fits performed on models including Poisson noise likewise produced the correct position angle, ellipticity and centroids.

Next, a model with noise was created with three de Vaucouleurs profile galaxies having the appropriate positions, ellipticities, and position angles for NGC 6166 (Lauer 1986). A series of tests were conducted using the various options provided by the **SNUC** routine. The routine allows the following: (1) fits may be performed allowing the centroids of the isophotes to vary; (2) the user may allow for the assumption that each galaxy extends over the entire image or may indicate the maximum size of each galaxy; (3) a box may be used to limit the region of the image fit by

SNUC; (4) the size of the initial centroid box can be varied to allow for error in the initial values of the center positions; (5) the number of iterations used for the fitting process may be varied.

The first test using the multiple component model compared the accuracy of the fits obtained by treating the centers as free parameters (allowing nonconcentric isophotes) with fits obtained by fixing the centers. For artificial galaxy B we plot in Figure 7 the errors in the fitted ellipticity, position angle and centroids as a function of radius along the major axis. The centers varied by up to 10 pixels when allowed to vary. When centers were fixed errors in the fitted centroid were only -0.43 pixels and -0.03 pixels in the x and y coordinates respectively. The best choice is to fix the centers since it would be impossible to separate real physical variations from algorithm-induced effects. All subsequent fits were performed with fixed centers. This eliminates our ability to detect non-concentric isophotes in the real galaxy such as those expected in galaxy interactions.

The second test compared the accuracy of SNUC in the cases when the galaxies are assumed to extend over the entire image as opposed to when their sizes are indicated. Figure 8 shows for artificial galaxy B the results for the ellipticities and position angles. Comparing the two fits, it is clear that the errors rise quickly in the outer regions. Over the region in common to the two fits the errors are less for the fits performed when the sizes are indicated by the user. The regions are different because fitting the galaxy over the entire image will naturally have a larger radial extent than one chosen by the user over only part of the image.

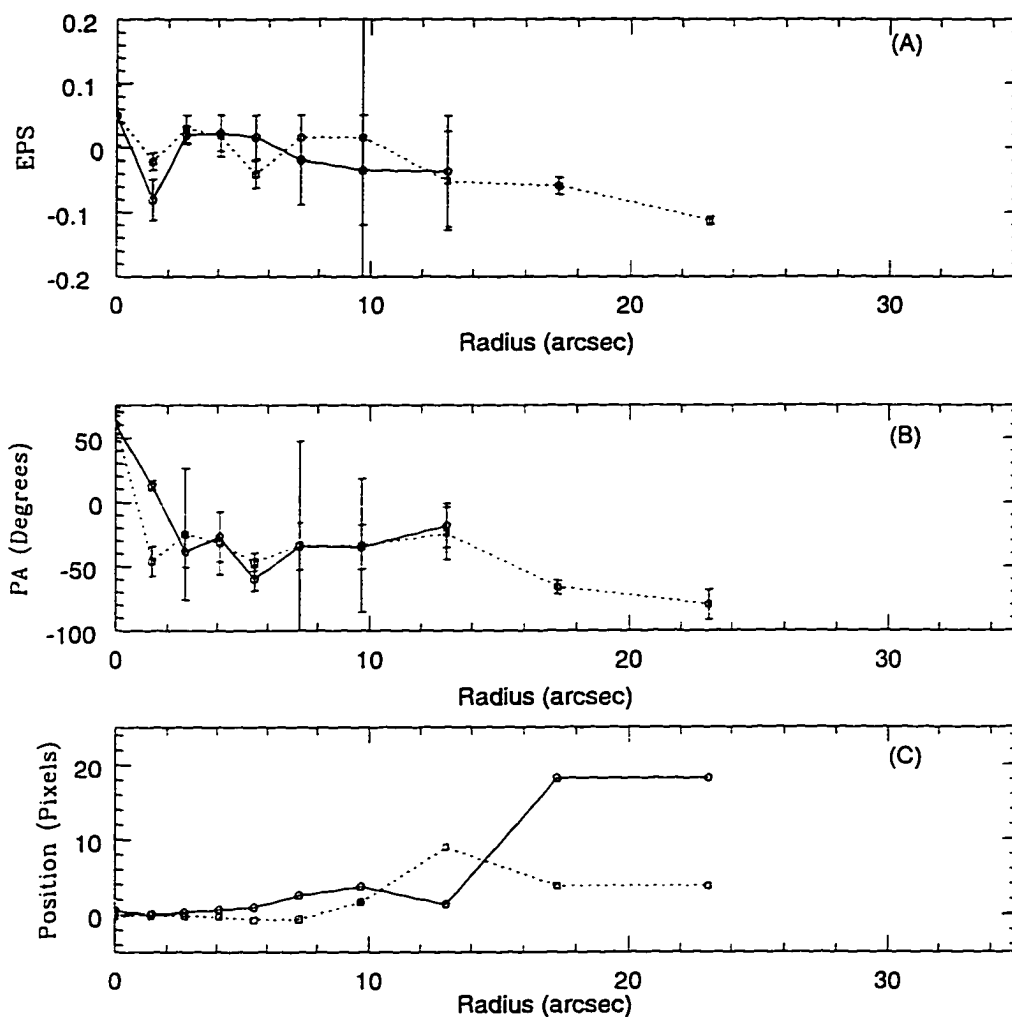


Figure 2: Test of the accuracy of SNUC for model nucleus B when galaxy centers are free parameters. (a) The error in the ellipticities, (SNUC - input) (b) the error in the position angles, (SNUC - input) (c) the error in the centroids, (SNUC - input). For plots A and B the solid line indicates the fits made with centers as a free parameter, while the dotted line is the corresponding fit with the centers fixed. For plot C the solid line shows the errors the x values of the centers and the dashed line shows the errors in the y values. In all cases, the fits with the locked centers are superior.

The third test employed a box around the objects which included only the three nuclei. This would serve to limit the area fitted on the images and reduce overall runtime. Here there are two possible ways to use **SNUC** to fit the galaxies. The first is to fit each galaxy over the entire region within the box; the second is to indicate the position and size of each galaxy within the box. The two methods are compared in Figure 9 where for model nucleus B we show the plots of errors in the fitted ellipticity and position angles as a function of radius. Also included are the results of fits performed after indicating the positions and radii for the three model galaxies with no limiting area indicated. The results are nearly identical at radii where the isophotes are completely within the boxed region. Outside these radii the errors rise. Better fits are obtained when the centers and outer isophotes are identified by the user and no limiting box is used.

The goal of the final tests was to determine the sensitivity of the fits to the number of iterations and the size of initial centroid box. Initial centroid boxes of 3 and 5 pixels were used to test the effect of changing this parameter on the accuracy of the **SNUC** fits. The fits were identical so it was decided to use the default size of three pixels for the fitting procedure. The tests on the number of iterations showed that it was perhaps the single most vital factor in the achievement of accurate fits. Shown in Figure 10 are the errors in the ellipticities and position angles for 3, 5 and 8 iterations. The fits improve as the number of iterations is increased. However, when more than 8 iterations were used the routine became unstable and terminated the fitting process.

In summary, the “best” method for the fitting of multiple nuclei was found to

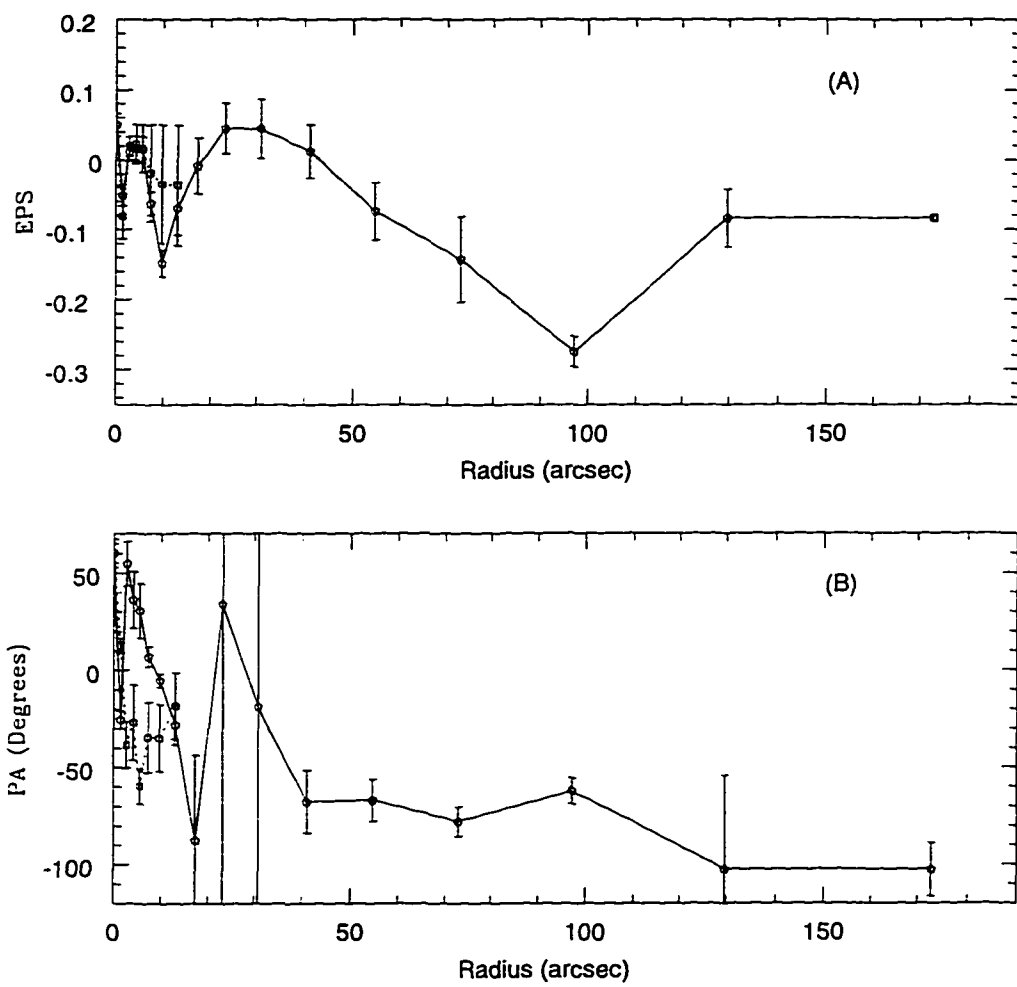


Figure 3: **SNUC** accuracy for model nucleus B when the galaxy is fitted over the entire image and when the center and radius of the fitting region around each galaxy are marked. (a) The error in the ellipticities, (**SNUC** - input) (b) the error in the position angles (**SNUC** - input). For both plots, the solid line indicates the fits made when fitting the entire image, while the dotted line is the corresponding fit with both the center and limiting radius indicated. In both cases, the fits with the centers and limiting radius indicated are superior.

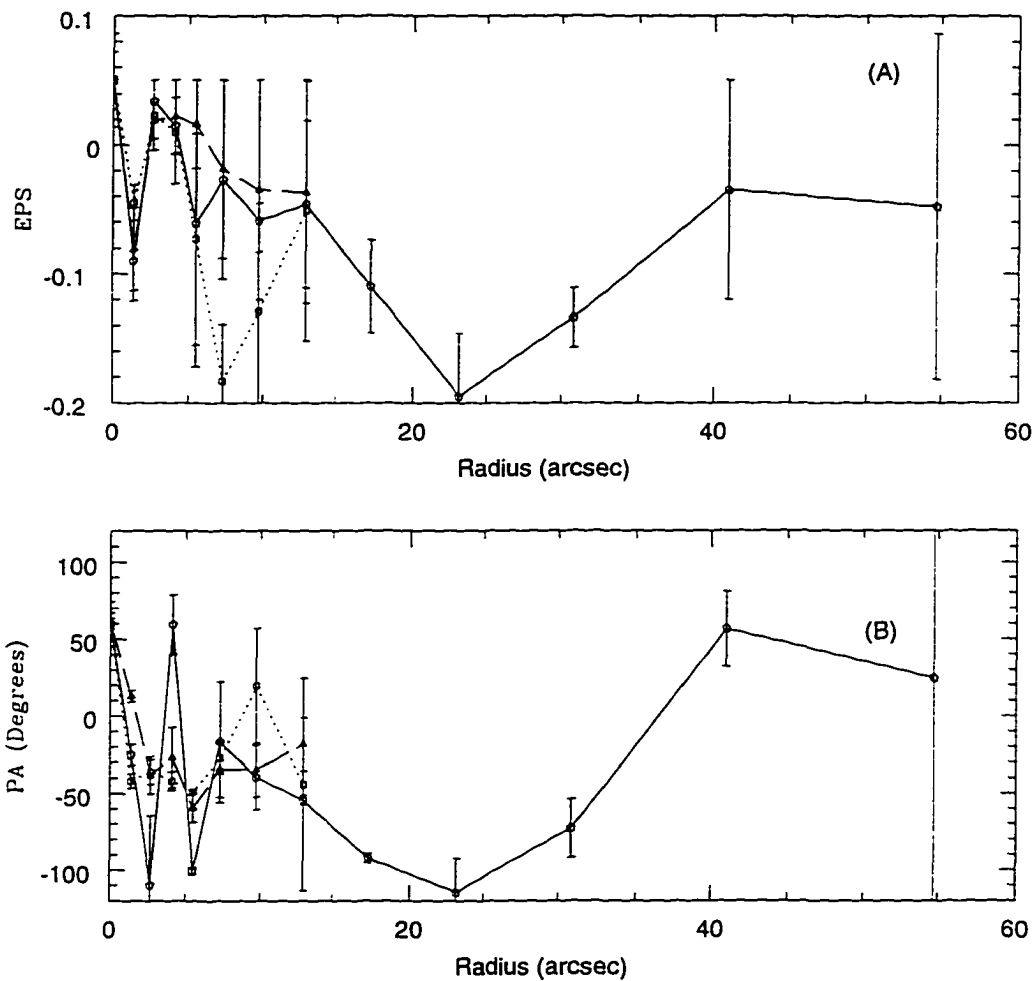


Figure 4: SNUC accuracy for model nucleus B when the galaxy is fitted over a boxed region. (a) The errors in the ellipticities, (SNUC - input) (b) the errors in the position angles (SNUC - input). For both plots, the solid line indicates the fits made when fitting the galaxy within the entire box, while the dotted line is the corresponding fit with both the center and limiting radius indicated within the box. The dashed line indicates the error for fits made when no box is used, but the limiting radius is indicated. In both cases, the fits with no limiting box are superior.

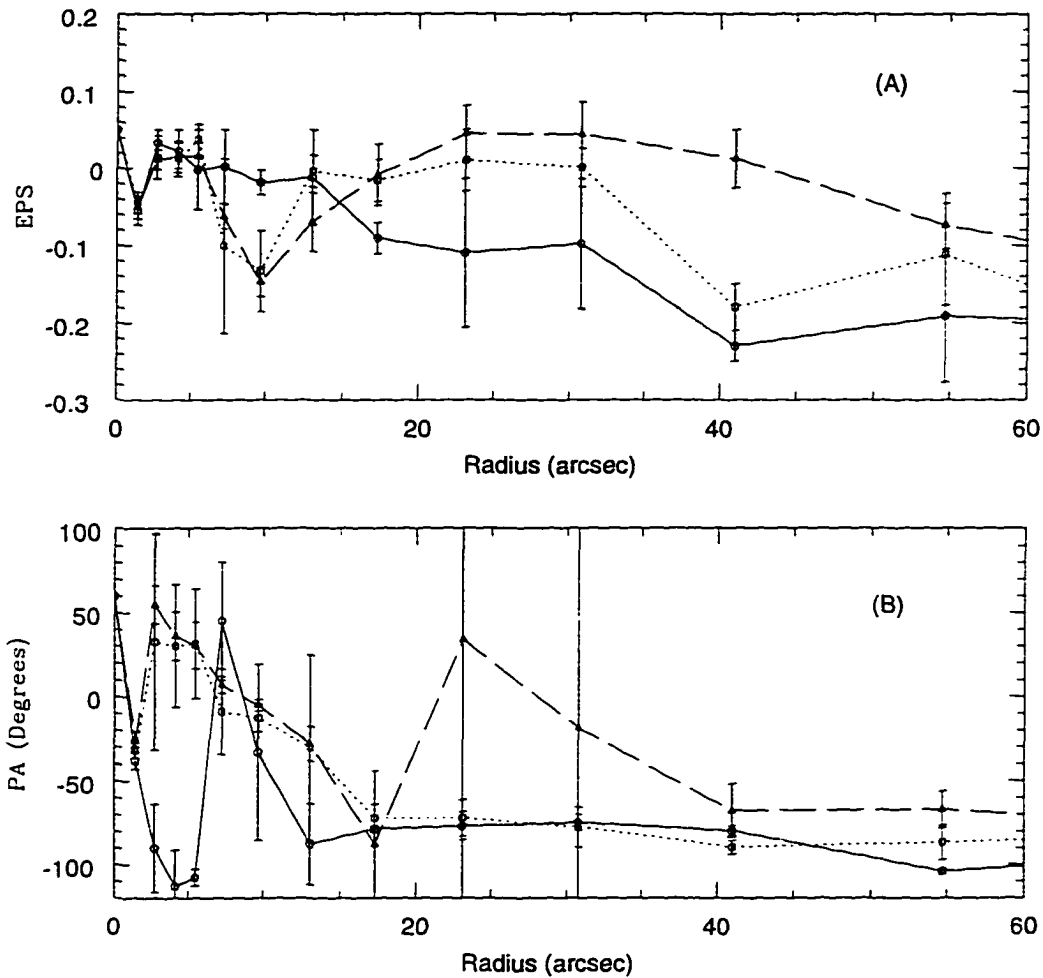


Figure 5: SNUC accuracy for model nucleus B when the number of iterations is varied. (a) The errors in the ellipticities, (SNUC - input) (b) the errors in the position angles (SNUC - input) for 3 iterations (solid line), 5 iterations (dashed line) and 8 iterations (dotted line). It is clear the accuracy improves when the number of iterations is increased. The maximum number of iterations allowed was found to be 8 without the program becoming unstable.

involve fixing the isophote centers, marking both the inner and outer isophotes for all galaxies, using default centroiding and using 8 iterations.

3.3 The Final Fitting

Before the final **SNUC** fitting, cosmic ray hits were removed using the **VISTA** program **ZAP**. **ZAP** is a boxcar median filter, which searches the image for pixels differing by a given amount from the median in a box of specified size. The value of the pixels identified are replaced by the median of the values within the box. The default box size of 5×5 pixels was used. Cosmetic flaws were then identified and masked out on each image. To avoid contamination of the measurements of NGC 6166, any unwanted objects must be masked before the program images are fitted using **SNUC**. Unwanted objects include nucleus D, the dynamical wake candidate (Lauer 1986), foreground stars and galaxies, cosmetic defects and cosmic ray hits. Nucleus D was found by Minkowski (1961) and Lauer (1986) to be a field star. In fact on our images, nucleus D has a full-width-at-half-maximum (FWHM) identical to a stellar object to within 1 pixel in FWHM, and thus nucleus D could not be fit by **SNUC**. When we attempted to do so, the centroiding algorithm locked onto the center of nucleus B in which nucleus D is imbedded. This caused the program to terminate. Therefore a box was used to mask out nucleus D.

The **VISTA RENUC** routine allows reconstruction of the galaxies fitted by **SNUC**. Dust features and the dynamical wake candidate (Lauer 1986) were identified by fitting a blue image and subtracting off a **RENUC** model of the fit. Dust extinction is greater in the blue passband so dust features are more easily identified

using the B -band. The most prominent dust feature was the “S” shaped feature lying near the center of nucleus A. The dynamical wake was also easily identified, along with galaxies and foreground stars. The position of the various features on this blue image were used as reference positions. We wished to mask identical regions on all images. We therefore require the positional shift from the reference image to all other images. These were calculated using the mean differences between the positions of nucleus A, B and C on the reference image and all other images.

In order to provide the best possible centroids, each image of NGC 6166 was fitted using **SNUC**. The **RENUC** routine was then used to reconstruct a model of two of the three galaxies. The model was subtracted and the resultant image was used to find an accurate centroid for the remaining galaxy using the **AXES** program in **VISTA**. The same regions were therefore masked out on all images.

The size of the fitting region for each nucleus was determined with the others subtracted from the image. The same fitting sizes were used on all images. The photometry was calibrated using the transformations in Equation 3. This produced B and R brightness profiles along the major axes of the galaxies, as well as ellipticities and position angles.

3.4 The Effect of Sky Error on the Photometry

We now investigate how errors in the sky determination affect the final fits. To examine this **SNUC** was run on an image with two different sky values subtracted. The first fit was performed on the image with adopted sky value subtracted. The second fit was performed on the image with the adopted sky $\times 1.01$ subtracted. A

1% change was chosen because as seen in Appendix C, the galaxy brightness is about 1% of the total light in the sky region. The results are shown in Figures 11, 12 and 13, which present the difference between the brightness, ellipticity and position angles as functions of radius. Other than the expected lower isophotal magnitudes, no systematic differences can be seen in the results. This would imply that the output ellipticities and position angles are not highly sensitive to errors in the sky values.

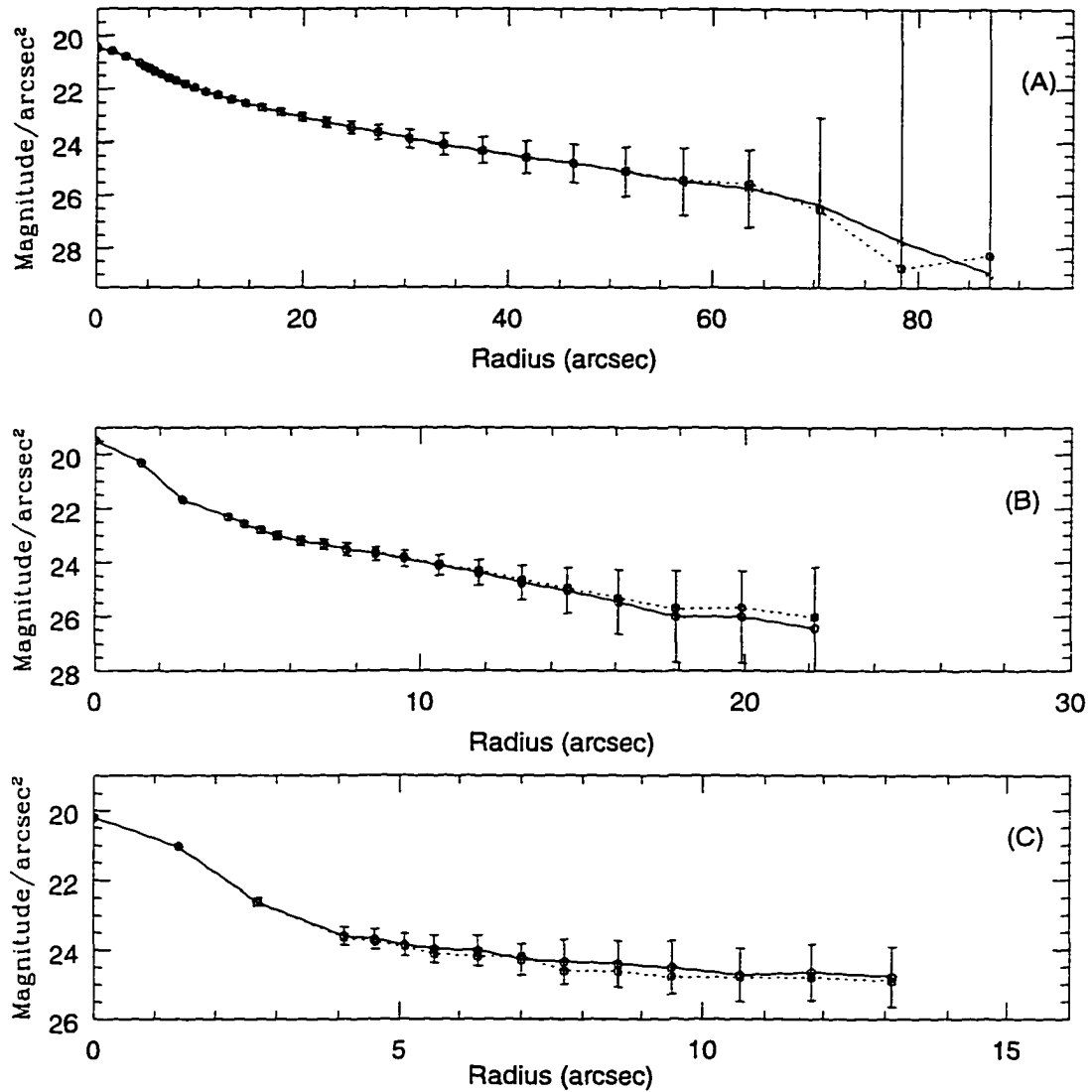


Figure 6: The effect of a 1% sky subtraction error on the fitted intensities of a 1200 second B image, for (a) Nucleus A (b) Nucleus B and (c) Nucleus C. Plotted are the fitted magnitudes for the adopted sky subtraction, (solid line), magnitudes for the *sky* + 1% subtraction (dotted line). It is clear here that the sky subtraction error does not seriously affect the magnitudes of the objects, since in all cases the fits agree within the uncertainties.

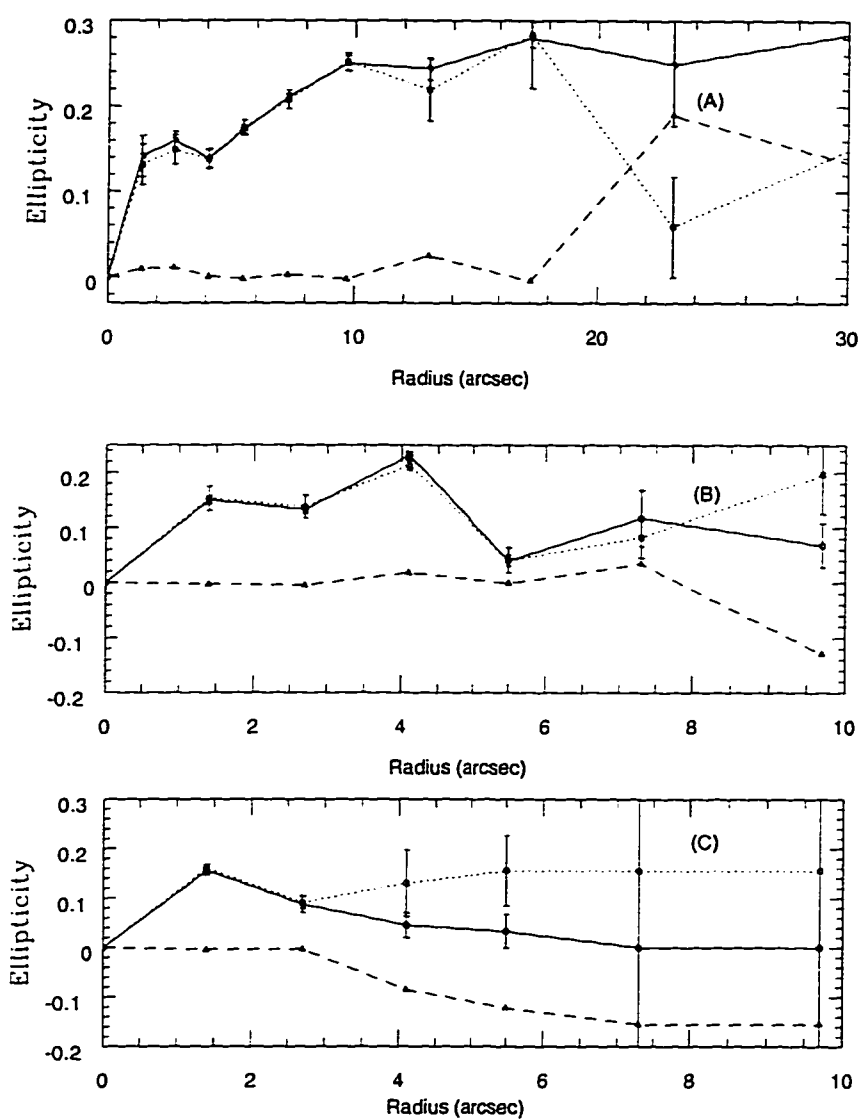


Figure 7: The effect of a 1% sky subtraction error on the fitted ellipticities of a 900 second R image, for (a) Nucleus A (b) Nucleus B and (c) Nucleus C. Plotted are the fitted ellipticities for the adopted sky subtraction, (solid line), the intensities for the *sky* + 1% subtraction (dotted line) and the difference between the two fits (dashed line).

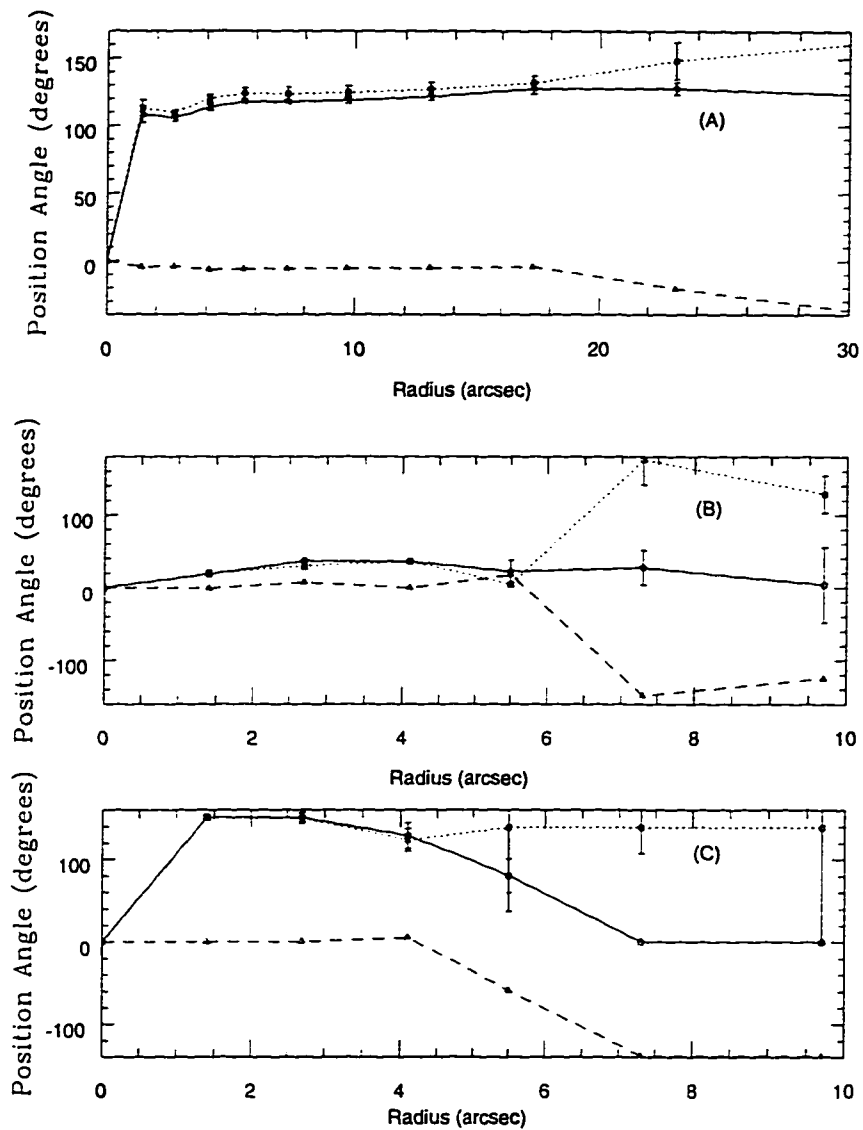


Figure 8: The effect of a 1% sky subtraction error on the fitted position angles of a 900 second R image, for (a) Nucleus A (b) Nucleus B and (c) Nucleus C. Plotted are the fitted ellipticities for the adopted sky subtraction, (solid line), the intensities for the *sky* + 1% subtraction (dotted line) and the difference between the two fits (dashed line).

4 Photometry of CFHT Archive images

4.1 Motivation for Using Additional Data

The spatial resolution of our data is limited near the centers of the nuclei. The seeing during the observations was between $1''.2$ to $1''.78$, which is poor for CFHT. The CCD scale is $0''.457/\text{pixel}$ and as a result there are few pixels sampling the brightnesses near the cores of the nuclei. Both of these factors combine to make it difficult to measure ellipticities and position angles close to the centers of the components of the NGC 6166 system. Our study would benefit from improved resolution near the cores of the nuclei. We used the CFHT Archive of the Canadian Astronomy Data Center (CADC) to obtain additional high resolution data for NGC 6166. Detailed information on the archive data is given in Table 14 in Appendix A. The data obtained from the CADC include bias and flat field images for pre-processing, a 300 second V -band image, a 600 second R -band image and a 1200 second B -band image. The V -band images were taken by Kormendy, McClure & Barton, on April 6, 1991. The B - and R -band images were taken by Nieto, on June 6/7 1991.

The CFHT archive data have the advantage that they were taken using the High Resolution Camera (HRCAM) which provides extremely high resolution images. These data have a scale of $0''.11/\text{pixel}$ and the seeing FWHM is only $0''.6$ on the archive images. This enables accurate determination of position angles and ellipticities closer to the core of the nuclei than possible with our own data. However, the archive images are of lower signal to noise ratio (SNR) than our CFHT data. This is because the smaller pixels cover much less of the sky, and must be integrated about

4 times longer in order to achieve the same SNR. This makes it difficult to obtain accurate information in the fainter outer regions of the nuclei. Our CFHT data are superior in the outer regions since the larger pixel scale makes measuring lower light levels easier; each pixel covers four times more area on the sky than the archive data. The two data sets are therefore complementary.

4.2 Pre-processing and Sky Subtraction

4.2.1 Pre-processing of CFHT Archive Data

The first step in utilizing the CFHT archive images was to pre-process them, using the steps outlined in Section 2.2. The CCD chip used to take the archive data has negligible dark current, so no dark image subtraction is necessary. All other pre-processing steps were the same as described in Section 2.2. The *V*-band images were taken on a different night, and with a different CCD than the *B* and *R*-band images and so were pre-processed independently.

The first step was to remove the DC offset from all images using the mean of the overscan region. The overscan region was located on the last 55 columns of the June 6/7, 1991 images and the last 55 rows of the April 6, 1991 images. The mean value in the overscan region was subtracted from the images. The overscan region was then trimmed from the images.

The second pre-processing step is bias image subtraction. The bias subtraction of the *V*-band images was performed using a different median bias image than the *B* and *R*-band images. The median of 16 bias images was subtracted from the *V*-band images. The median of three bias images which were themselves the median of 20

individual bias images were used to bias subtract the B and R -band images.

The final pre-processing step was the flat fielding of the images. Sky flat field images were used for the V -band images. These sky flat images were obtained by pointing the telescope at a blank region of the twilight sky and then turning the drive motor off. This trails any stars and galaxies in the field. The median of the sky flat images will have these objects efficiently removed since they are on different pixels on every image. The median V -band sky flat field image was the median of three sky flat images. The median V -band sky flat image was blinked with the original sky flat field images to ensure no artifacts from trailed stars or galaxies remained.

The R -band flat field was a median of 10 dome flat field images, which were median combined at the telescope. The median B -band dome flat field image was created from the average of two B -band dome flat images which were combined at the telescope. These two images were the median of 10 B -band dome flat images. The flats were divided into the B , V and R -band NGC 6166 images. The division was scaled by the mean of the flat field images as described in Section 2.2.

4.2.2 Checking the Flat Fielding

One V -band image of a blank sky region near NGC 6166 taken on the same night as the V -band image was obtained from the CADC. This was used to check the flat fielding as in Section 2.3. Five 75×75 pixel boxes scattered around the image were used. These boxes were examined on the display to ensure they contained no stars or galaxies. They were then cleaned of cosmic ray hits and the mean of the boxes computed. The results are shown in Table 5.

Table 5: *V*-Band Flat Field Test Results

Region	Mean (ADU)
Box 1	32.36
Box 2	31.20
Box 3	31.91
Box 4	31.55
Box 5	32.22

The standard deviation of the mean of the boxes is 1 ADU, or about 3%. This is much greater than for our own images. Since no blank sky images are available, the flat fielding cannot be further improved. However, the variation is smaller than the shot noise. There may also be contamination from the halos of objects lying outside the regions measured.

4.2.3 Sky Determination

The sky determination was carried out in the same manner as our own CFHT images. This is because no blank sky images are available in the *B* and *R* passbands, and only one sky image is available in the *V*-band. Therefore we followed the method outlined in Appendix C to determine the sky value to be subtracted from the images. The sky values are given in Table 6.

Table 6: Adopted Sky Brightnesses

Image	Passband	Sky (ADU)
112608o	<i>V</i>	8.03
116613o	<i>R</i>	95.06
116614o	<i>B</i>	110.51

4.3 Surface Photometry and Calibration of NGC 6166 Archive Images

4.3.1 Surface Photometry of the CFHT Archive Images

We have performed the same steps to obtain surface photometry of the archive images as our own CFHT data. These steps have already been described in Section 3.3. The first step was to identify the regions on the images containing any dust features and foreground galaxies. These were identified by first fitting the images using **SNUC**, and subtracting off a **RENUC** model constructed from the fits. The main dust feature identified was the S-shaped feature near the center of nucleus A, and a smaller dust feature to the east. In the case of the *V*-band image, nucleus D was also masked out. In the *B*- and *R*-band images, nucleus D was sufficiently bright and separated from nucleus B that it was possible to fit it along with the other three nuclei. Cosmic ray hits were removed using **ZAP** (see Section 3.3), and bad columns and rows masked.

The centers of the nuclei were identified by reconstructing all galaxies but one, and then using the **AXES** command to compute a precise centroid. The radii used

for nuclei A, B and C were the same used for our own CFHT images. The radius of nucleus D was determined by examining an image with all other nuclei subtracted. SNUC was then run using the input positions and radii determined above.

4.3.2 Calibration of CFHT Archive Images

No standard star images are available in the CFHT archive data. We are left with the problem of transforming instrumental brightnesses into a standard photometric system. Regardless of the photometric conditions, for a given passband a galaxy must have the same total brightness inside a given aperture. We can use this fact to find the zero point difference between the Cousins system and the archive image instrumental system. The zero point is determined by equating a measured instrumental brightness on the archive images to a measured standard magnitude. This allows the intensities measured on the CFHT archive images to be converted to the Cousins system.

The VISTA program **APER** was used to perform synthetic aperture photometry on our own CFHT *B*- and *R*-band images, and the *B*- and *R*-band archive images in a $25''0$ aperture. **APER** calculates the total brightness inside a circular aperture centered upon an image position specified by the user. The center of nucleus A was chosen as the center of this circular aperture. The measured brightnesses were normalized to a one second exposure by dividing by the exposure time. The brightnesses on our CFHT images were converted to the Cousins system using equations 3 and 4. Table 7 gives the intensity within $25''0$ on the archive images and our CFHT images, and the magnitude corresponding to the brightness measured on CFHT images. It should be noted that the brightness data for image 260 may be paired with either

the data from image 255 or 257 in equations 3 and 4 to calculate the R magnitude. Thus two estimates of the R -band magnitude for this image are presented in Table 7. The mean of the B - and R -band magnitudes for our CFHT data were averaged to give the mean magnitude corresponding to the B - and R -band archive brightnesses. This allowed the brightness on the archive images to be transformed to the Cousins system. equations 6 and 7 give the transformations to the Cousin system.

$$R = R_o - 2.5 \times \log(I_r/I_{ro}) \quad (6)$$

$$B = B_o - 2.5 \times \log(I_b/I_{bo}) \quad (7)$$

Where B and R are the standard B and R magnitudes in the Cousins system, R_o and B_o are the B-band and R-band zero points, I_b and I_r are the brightnesses in the B - and R -band, and I_{ro} and I_{bo} are the brightnesses corresponding to R_o and B_o respectively. Taking the average of the magnitudes and brightnesses from Table 7 we get: $R_o = 12.158 \pm 0.065$, $B_o = 14.143 \pm 0.034$, $I_{ro} = 2.16 \times 10^4 \pm 147$, and $I_{bo} = 1.07 \times 10^4 \pm 103$. Using equations 6 and 7 the surface photometry of the archive images was transformed to the standard system.

Table 7: Data for Calibration of Archive Images

Image	Passband	Intensity (ADU)	Magnitude
161	<i>R</i>	8681.11	12.219 ± 0.016
164	<i>B</i>	3276.67	14.065 ± 0.023
255	<i>B</i>	2965.00	14.170 ± 0.022
257	<i>B</i>	2968.33	14.167 ± 0.022
260	<i>R</i>	8513.33	12.226 ± 0.015
116613o	<i>R</i>	95.06	NA
116614o	<i>B</i>	110.51	NA

5 Aperture Photometry of NGC 6166

5.1 Reasons for Performing Aperture Photometry

In addition to surface photometry, aperture photometry was performed on the NGC 6166 images. There are several reasons for this. We wish to make a comparison of the global colours ($B - R$) of nuclei B and C to those of “normal” elliptical galaxies to address the question of whether the multiple nuclei of NGC 6166 represent an interacting system. The global colours can be derived by fitting the measured surface photometry to known functions to give the total intensity. For instance, the well known de Vaucouleurs Law (de Vaucouleurs 1948) is given by:

$$\Sigma(r) = \Sigma_e 10^{\{-3.33[(r/r_e)^{1/4} - 1]\}} \quad (8)$$

Where $\Sigma(r)$ is the brightness at radius r , r_e is the radius enclosing half the total light of the galaxy and Σ_e is the brightness at r_e . By integrating the de Vaucouleurs law to infinity (Mihalas & Binney 1981) we get the total brightness of the galaxy. For a circular galaxy:

$$\Sigma_{total} = 7.22\pi r_e^2 \Sigma_e \quad (9)$$

However, for tidally truncated galaxies, we might expect the de Vaucouleurs law to be unable to match properly the surface brightness profiles of the galaxies resulting in incorrect total magnitudes. This would be true for any of the empirical functions fit to elliptical galaxies. The best way to avoid model-dependent assumptions is to use circular apertures centered on each nucleus to derive a total magnitude for each nucleus.

Aperture photometry may also be used to construct an aperture growth curve for the nuclei. It is also known that elliptical galaxies have a common growth curve, as shown by de Vaucouleurs *et al.* (1976) and more recently by Burstein *et al.* (1987). Tidally truncated galaxies should deviate systematically from the mean growth curve defined by normal ellipticals. The growth curve method may therefore serve a twofold purpose of first providing the total magnitudes of the nuclei directly, and second providing a test of whether nuclei B and C fit the mean growth curve.

Finally, the aperture photometry can provide the structural parameter D_n as defined by Burstein *et al.* (1987). Burstein *et al.* (1987) define the D_n parameter as the diameter of the circular aperture which encloses a mean integrated B-band surface brightness of 20.75 magnitudes/arcsecond². The particular choice was made in such a way as to provide a parameter that was bright enough to be measurable on a large number of galaxies, but was large enough to be relatively free from the effects of seeing.

The D_n parameter can give an important indication as to whether the nuclei B and C are interacting with nucleus A. Recently Weinberg (1996) has shown that a small galaxy which has been captured by a larger galaxy will be affected by three mechanisms: (1) internal heating, (2) mass loss due to tidal forces and (3) orbital decay due to dynamical friction. Weinberg states that a secondary galaxy will experience a periodic force as it moves. If the resulting tidal force changes faster than the timescale of the internal motions in the object, then the galaxy will be shocked and will expand. A captured galaxy will also have material in its outer regions stripped

by tidal forces, reducing its mass. Finally, the orbiting galaxy will cause a concentration of matter behind it in the form of a tidal wake. The gravitational force of this material will slow the orbit of the secondary galaxy and cause the orbit to spiral into the center.

There are two interaction scenarios possible (Schombert 1996). A galaxy undergoing a slow encounter will be tidally truncated by an encounter with a larger galaxy. However, if the orbital time of the secondary is comparable to its internal orbital timescale, then the shocking will not be as severe. A fast encounter will “shock” a galaxy, making it physically larger. Thus, in the plot of $\log D_n$ vs. total B magnitude, the slow encounter galaxy will have a smaller $\log D_n$ for its brightness, while the galaxy undergoing a fast encounter will have a larger D_n value for its total magnitude. Using aperture photometry to measure D_n can therefore provide an important test to check for interaction of the components of NGC 6166.

5.2 Performing Aperture Photometry of Nucleus B and C

5.2.1 Removal of Unwanted Objects

Before performing aperture photometry of the nuclei we must remove all contaminating objects from the images. The other three nuclei must be subtracted from the images in order to measure the fourth. Thus, in order to perform aperture measurements on nucleus B, nuclei A, C and D must be subtracted from the images. We may remove any of the three brightest galaxies by using **SNUC** to fit the galaxies, and then using **RENUC** to model all but one of the galaxies. Then the model may be subtracted from the images.

In order to remove nucleus D and the tidal wake candidate, we first clipped the pixels encompassing these two objects. **RENUC** was then used to reconstruct the galaxy to be measured. The values of the clipped pixels were then replaced by the model values. Photometry of the wake is discussed in Section 5.3.

5.2.2 Calculation of Total Magnitudes

We wish to obtain the total B and R magnitudes of nuclei B and C. In order to remain as consistent as possible to Burstein *et al.* (1987) we follow the steps outlined there to derive the total B magnitude. These are essentially the steps outlined by de Vaucouleurs *et al.* (1976). The first step is to obtain the total magnitude of the galaxy by plotting the magnitude of the galaxy as a function of aperture diameter. The total intensity inside each aperture was normalised to a 1 second exposure time by dividing by the exposure time. Equations 3 and 4 in Subsection 2.5.3 were then used to calculate the aperture magnitudes.

As the aperture radius is increased, the aperture magnitude will asymptotically approach the total magnitude of the galaxy when the difference in the magnitude between successive aperture is zero. This so-called “growth curve” is exactly analogous to the aperture growth curves computed for the standard stars in Section 2.3. The radii for aperture photometry measurements chosen were in 1'' increments up to 50''. It was found that nucleus B reached its asymptotic magnitude at 25'' while nucleus C reached its asymptotic magnitude at 17''. Total magnitudes were derived in both B and R passbands.

There are three corrections which must be made to the raw B -band magnitudes

before D_n is calculated. The first correction made is for galactic extinction, which Burstein *et al.* (1987) find to be zero. The second correction is the K-correction. The light from distant objects is redshifted from the observer by an amount dependent upon its distance. As a result, the photometric passbands used at the telescope will sample a different part of the spectrum of the object if it is far away, than if it is at rest with respect to the observer. If we wish to compare measurements made of different objects at different redshifts, then we must correct the measured magnitudes for the redshift of the spectrum. From de Vaucouleurs *et al.* (1976), the K-correction for NGC 6166, which is at a redshift of 0.03, is 0.14 magnitudes. This is subtracted from all B -band magnitude measurements. The final correction is made for the cosmological dimming. This requires the surface brightnesses to be divided by $(1 + z)^4$, where z is the redshift. This is required by the geometrical size changes caused by the expansion of the universe. (See Sandage, Kron & Longair 1995 for details).

5.2.3 Calculation of D_n

The value of D_n is easily computed from the B -band aperture photometry. The total intensity inside each aperture was divided by the exposure time and the area of the aperture. Equations 3 and 4 then give the total integrated surface brightness for that aperture (corrected as described in Section 6.2). The value of D_n was determined by fitting a cubic spline to the plot of integrated B surface brightness *vs.* aperture diameter. The spline fit was then evaluated at the B -band surface brightness of 20.75 magnitudes per square arcsecond, to give D_n .

5.3 Photometry of the Tidal Wake Candidate

Lauer (1986) identified a tidal wake candidate between nuclei B and C. He speculated it could be caused by the fast passage of nucleus B through the envelope of nucleus A. We are able to perform the first colour study of this feature, in order to determine if the colours are consistent with what is expected from such a feature. A tidal wake is formed behind an object as it gravitationally pulls stars from the halo of a larger object into its path of motion. The result is a density enhancement behind the galaxy. If the tidal wake candidate identified by Lauer (1986) is a true tidal feature, then it should have the same $B - R$ colour as the halo of nucleus A at the distance of the wake. Since we can easily compute a $B - R$ colour from our SNUC photometry of nucleus A, aperture photometry on the wake candidate is valuable.

To perform the photometry, the first step was to remove all possible contaminating objects near the wake candidate. SNUC was used to fit nuclei A, B and C, RENUC was used to model the nuclei, and the models were then subtracted from the original images. A PSF was computed for each image in the same manner as described in Section 2.5.2 was used to subtract nucleus D.

A key problem is that the northern-most edge of the wake candidate overlaps with the large nuclear residuals of nucleus B. To avoid this problem, the region occupied by the wake on all images was first identified. The region of the measuring box was 11×16 pixels wide. The center of the box was located on the blue reference image (see Section 3.3) and the positional offsets used to move the position of the box to the appropriate location on all images. This is the same procedure used to ensure the

same dust regions were masked on all images in Section 3.3. For each region to be measured a histogram of the values inside the box was plotted. The histogram showed a characteristic Gaussian shape, with a small number of large negative and positive residuals about the mean. The values outside the Gaussian were masked using the **CLIP** program inside the **VISTA** package. **CLIP** masks all pixels outside the upper and lower ranges specified. In this manner the high positive and negative residuals near the center of nucleus B were masked. The **ABX** program inside **VISTA** was then used to obtain the total intensity inside the region occupied by the tidal wake. Using equations 3, 4 and the airmass, the intensities were transformed into total *B*- and *R*-band magnitudes.

If the tidal wake candidate is truly a tidal feature, then it should have the same colour as the central galaxy at the same position from the center. We therefore adopted the center of the wake as the center of the box used to measure its light. The major-axis length of the isophote running through the center of the wake was then computed using Equation 22, in Appendix C. We interpolate between the points of our mean *B*- and *R*-band profiles of Figures 9 and 10 to obtain the *B*- and *R*-band brightnesses of the isophote running through the center of the wake. The $B - R$ of this isophote then gives the an estimate of the colour of the galaxy at the location of the wake candidate.

Weinberg (1986) has modeled tidal wakes formed by the passage of a satellite galaxy through a medium of arbitrary density distribution. He defines a quantity called the overdensity, which enables us to compare our tidal feature to his models.

Weinberg (1986) defines the overdensity, as the fractional density enhancement over the background. If ρ_o is the background density, and ρ is the density in the presence of a satellite, then the overdensity is defined as:

$$\xi = \frac{(\rho - \rho_o)}{\rho_o} \quad (10)$$

For a satellite of mass M_s moving with velocity V_t through a medium with internal velocity dispersion σ , Weinberg (1986) gives an analytic expression for the overdensity (see his Equation 3). We may use our aperture photometry to estimate the overdensity of the wake as follows. We adopt the velocity dispersion of the background medium to be the velocity dispersion of nucleus A from Tonry (1985). Tonry (1985) also gives the mass-to-light ratio (M/L) of nucleus B as $10M_\odot/L_\odot$, and the relative radial velocity of nucleus B to nucleus A to be 1285 km/s. We then use the total magnitude of nucleus B from our aperture photometry to calculate its absolute magnitude. The (M/L) then gives the mass of nucleus B. As a first approximation, we assume the radial velocity of nucleus B relative to nucleus A to be the orbital velocity of the orbit of nucleus B. Weinberg (1986) also requires the spatial coordinates used to be given units of $(GM_s)/\sigma$. In order to compute the densities from the brightnesses, we require the (M/L) of the wake and the background. However, we assume that since the material of the wake is supposedly formed from the material of the background, the mass-to-light ratios are the same. In the ratio taken, the (M/L) will therefore cancel and is not required.

The observed overdensity is computed from the added intensity of the wake over the light of Nucleus A at its distance. If the (M/L) is assumed to be the same, then

the ratio of the brightness of the wake at any point to the brightness of nucleus A at that point gives the overdensity. This is because we have measured the brightness of the wake with the light from nucleus A subtracted. This effectively computes $(\rho - \rho_0)$ in equation 10, because we are only measuring the excess light above the background of A. The overdensity is therefore given observationally by:

$$\xi = \frac{I_{wake}}{I_A} = 10^{0.4 \times (M_A - M_{wake})} \quad (11)$$

where I_{wake} and I_A are the intensities of the wake and Nucleus A respectively at any point, M_{wake} and M_A are the apparent magnitudes of the wake and nucleus A at that point. We adopt the center of the wake as our reference point for comparison. We discuss these results in Section 7.2.3.

6 Calculation of Dust Mass.

6.0.1 Motivation for Calculating the Dust Mass

Lachiéze-Rey *et al.* (1985) find that nucleus C is a bluer object than nucleus B. They state that while the central color of nucleus B and C are the same, $B - R \sim 2.0$, the global color of nucleus C is bluer by about 0.4 magnitudes. Thus the global color of nucleus C is $B - R \sim 1.6$. Lachiéze-Rey *et al.* (1985) claim that this is more like the global color of a Sb galaxy, rather than an elliptical. This leads to the question of whether nucleus C is the bulge of a spiral galaxy which has been cannibalised. We attempt to check this as follows. If nucleus C has been stripped of its gas and dust, then it might be argued that the dust component seen in the core of nucleus A represents material stripped from nucleus C. If so, we expect the dust mass of nucleus A to be similar to that of a spiral galaxy.

6.0.2 Calculation of Dust Mass for NGC 6166

We may derive a dust mass using the extinction of the light of the galaxy caused by the dust, Brosch *et al.* (1990); Brosch & Loinger (1991); Veřon-Cetty & Veřon (1988); van Dokkum & Franx (1995). We follow the method outlined by Veřon-Cetty & Veřon (1988) to compute the dust mass. The components of NGC 6166 were modeled by **SNUC** and **RENUC** used to reconstruct the galaxies. The model was then divided into the original images, creating an absorption map. Areas where the model is brighter than the original image should be regions of dust. All dust regions in the core were identified, and the **IRAF** routine **LISTPIX** was used to output the values

of the absorption. For each pixel, the mean B and R absorptions were computed. In some cases, noise might make a pixel seem to be an absorption feature. To eliminate such spurious detections we use the method of Brosch & Loinger (1991) and reject all pixels whose mean B or R absorption is greater than 1.0. This procedure eliminates spurious pixels, and possible emission features.

In addition, the reddening should be larger in the B -band than the R -band. All pixels which had an average absorption greater in the R -band than the B -band were rejected. This also tests to see if the large absorption feature seen to the north of the nucleus by Lauer (1986) is indeed a dust feature, or is due to non-concentric isophotes. The pixels which survived these checks are shown in Figure 24. The large feature seen to the north of the nucleus by Lauer (1986) does appear to be caused by absorption due to dust.

To compute the dust mass we use the result of Veřon-Cetty & Veřon (1988):

$$M_D = \frac{\Sigma \langle A_B \rangle}{\Gamma_B} \quad (12)$$

Where M_D is the dust mass in solar masses, Σ is the area in Kpc covered by a dust feature, $\langle A_B \rangle$ is the absorption in magnitudes in the B -band, and Γ_B is the B -band mass absorption coefficient. It should be noted that this provides a minimum dust mass, since it assumes that all the dust lies in front of the galaxy. The mass increases when the dust is assumed to lie within the galaxy. From Veřon-Cetty & Veřon (1988) $\Gamma_B = 8 \times 10^{-6} \text{magkpc}^{-2} M_{\odot}^{-1}$. This coefficient assumes that the dust mass absorption coefficient is similar to that of dust in the Milky Way. The absorption, $\langle A_B \rangle$, is

given by equation 13.

$$\langle A_B \rangle = -2.5 \times \text{Log}\left(\frac{I_{obs}}{I_{model}}\right) \quad (13)$$

Where I_{obs} is the observed intensity, and I_{model} is the modeled intensity. With an assumed distance of 187 Mpc, each pixel subtends an area of 0.171 kpc^2 . The total dust mass is derived by using equation 13 to compute the absorption in magnitudes for each pixel, and then using equation 12 to compute the dust mass for that pixel. The total dust mass for NGC 6166 is then simply the sum of all the contributions.

7 Results

7.1 Results From Profile Fitting Photometry

7.1.1 Averaging the Surface Brightness Profiles

After performing the SNUC photometry on all NGC 6166 images, average B and R profiles were computed for all three nuclei. The profiles for our CFHT data were first converted to standard magnitudes using equations 3 and 4. This produced three B-band profiles, and two R -band profiles. The profiles in each passband were then averaged to create average B and R profiles for each nucleus. The profile fitting results from the CFHT archive images were not included in the average because they are calibrated with our CFHT images, which could bias the results. We present separate profiles for these data.

The uncertainties for the mean profiles are calculated by computing the brightness of the isophote with its uncertainty in intensity alternately added and subtracted from the computed intensity. This gives uncertainties in the individual measurements in magnitudes. To compute the average magnitude we convert the measured magnitudes to arbitrary intensity units using:

$$I = 10^{-0.4 \times M} \quad (14)$$

where I is the intensity, and M is the magnitude. The upper and lower range of the magnitude is used to calculate the uncertainty in these units. The mean value in intensity is calculated and the uncertainty is calculated, using equation 15:

$$\sigma_{\mu}^2 = \sum [\sigma_i^2 (\frac{\partial \mu}{\partial I_i})^2] \quad (15)$$

Where σ_{μ}^2 is the variance in the mean, σ_i is the variance in measurement i , μ is the mean value, and I_i is the i th intensity measurement. The mean intensity is converted to magnitudes using equation 5. The uncertainty in the mean intensity is converted to an uncertainty in magnitude by computing the magnitude with the uncertainty both added and subtracted from the mean value.

7.1.2 Features of the Surface Brightness Profiles

The computed average B and R brightness profiles for nuclei A, B and C are given in Figures 9 and 10. Here we have plotted the measured surface brightness profiles of nuclei A, B and C as a function of isophote major axis length to the 1/4 power. Plotting the profiles in this manner linearizes the de Vaucouleurs law. These plots show that all three nuclei seem to be well fit to de Vaucouleurs laws outside the seeing FWHM. We do not expect the profiles to fit the de Vaucouleurs law inside the seeing FWHM because the brightness peak in the center is smeared out by the seeing. We have indicated the radius of the average seeing FWHM on our profiles. The truncation of the profile of nucleus B reported by Lachiéze-Rey *et al.*(1985) and Lauer (1986) seems to be marginally detected, with a possible change of slope in the profiles near major axis position $r^{1/4} = 1.''8^{1/4}$. This is near the same position as the change in slope seen in the Lauer (1986) profile (see his Figure 6). While this is suggestive that the truncation is real, within the uncertainties the profile of nucleus B is well fit by a de Vaucouleurs law. It may appear that nucleus C seems to show

a decrease in slope in its outer radii. However, the uncertainties here are very large, and the background caused by nucleus A is also very large. It may be that we are measuring contamination from nucleus A.

Figures 11 and 12 show the B and R -band major axis surface brightness profiles of nuclei A, B and C as measured on the CFHT Archive images. There is higher scatter for all nuclei. However, it is clear that outside the seeing radius, the nuclei are well described by the de Vaucouleurs law. The uncertainties for nucleus C are such that it is difficult to draw any conclusions. However, the profile for nucleus B is very straight and no evidence for truncation is present.

7.1.3 Comparison of Surface Brightness Profiles to other Work

We compare our results to the B and R -band photometry of Lachiéze-Rey *et al.* (1985) in Figures 13 and 14. Here, the same corrections have been applied to both datasets. To transform our Cousins photometry to the Johnson system, we use the transformations given in Davis *et al.* (1985). We do not have uncertainty estimates for the Lachiéze-Rey *et al.* (1985) profiles, so the comparison is uncertain. Further, they published only their B -band photometry for nucleus A, and R -band photometry for nucleus B. Finally, the data were read off photocopies of their plots, and this adds to the uncertainty in the comparison. The profile we derive for nucleus A is brighter in the central regions, and fainter in the outer radii than Lachiéze-Rey *et al.* (1985), but the uncertainties in our outer isophotes are large.

Lachiéze-Rey *et al.* (1985) include nuclei B and D as a single object in their study. With the two objects included, we expect that their combined object would

have a much slower dropoff in light when compared to our work. Yet examination of Figure 14 shows the opposite to be the case. The *R*-band profile of nucleus B shows a shallower profile in our work, while the profile of Lachiéze-Rey *et al.* (1985) shows a sharp drop off. However, it is important to note that our profile also appears much straighter than theirs, which has a curved appearance. Our profile shows that nucleus B is well fit to a de Vaucouleurs law, while Lachiéze-Rey *et al.* (1985) suggest it is not. Once again, however, true comparison is difficult without proper uncertainty estimates for their data. The clean separation of the light of nucleus D and the wake in our study, and the fact that our profile is the result of the average of multiple measurements should make our result more trustworthy.

7.1.4 Position Angle and Ellipticity Profiles

The position angle and ellipticity profiles might be expected to be different in the two passbands because dust absorption will affect the *B*-band profiles to a larger extent than the *R*-band images. However, plots of the position angle and ellipticity profiles show the profiles to be similar within their errors. This agreement lends credibility to our identification and masking of dust lanes before performing the SNUC fitting. All five determinations of the ellipticities and position angles were averaged for each nucleus. Figures 15 and 16 show the average position angles and ellipticities for all three nuclei.

The uncertainties in the mean ellipticities are computed using:

$$\sigma_{\mu}^2 = \sum [\sigma_i^2 \left(\frac{\partial \mu'}{\partial \epsilon_i} \right)^2] \quad (16)$$

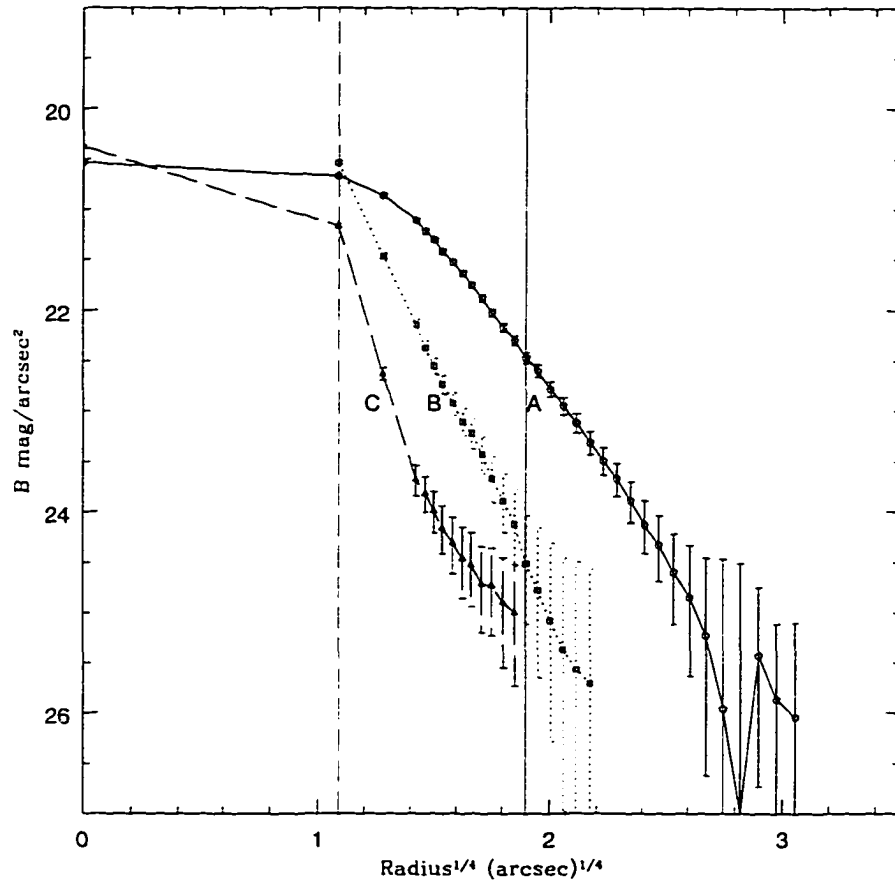


Figure 9: B-band surface brightness profiles for nuclei A, B and C computed from photometry or our CFHT images. The brightness in B magnitudes per square arcsecond is plotted as a function of major axis position to the 1/4 power. This choice linearizes the de Vaucouleur law. Nuclei A, B and C seem well described by a de Vaucouleurs law. The truncation of nucleus B indicated by Lauer (1986) is not evident. Nucleus C seems well fit by a de Vaucouleurs law, but the outer most photometry may suffer from contamination from nucleus A. The vertical dot-dashed line shows the radius of the mean seeing FWHM. The vertical solid line shows the distance of Nucleus B from Nucleus A. The profiles of nuclei A, B and C are labeled.

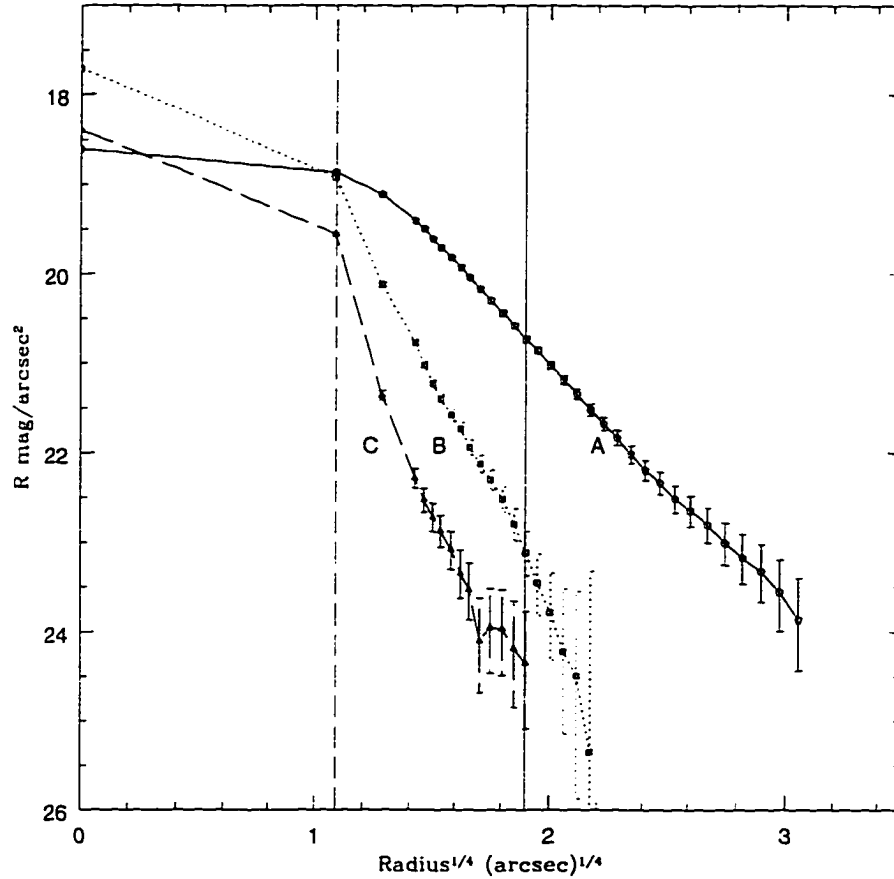


Figure 10: R -band major-axis brightness profile for nuclei A, B and C computed from photometry of our CFHT images. The brightness in R magnitudes per square arcsecond is plotted as a function of major axis position to the $1/4$ power. This choice linearizes the de Vaucouleurs law. Once again all three nuclei seem well described by a de Vaucouleurs law, as indicated by the linear shape of the brightness profile. The vertical dot-dashed line shows the radius of the mean seeing FWHM. The vertical solid line shows the distance of nucleus B from nucleus A. The profiles of nuclei A, B and C are labeled.

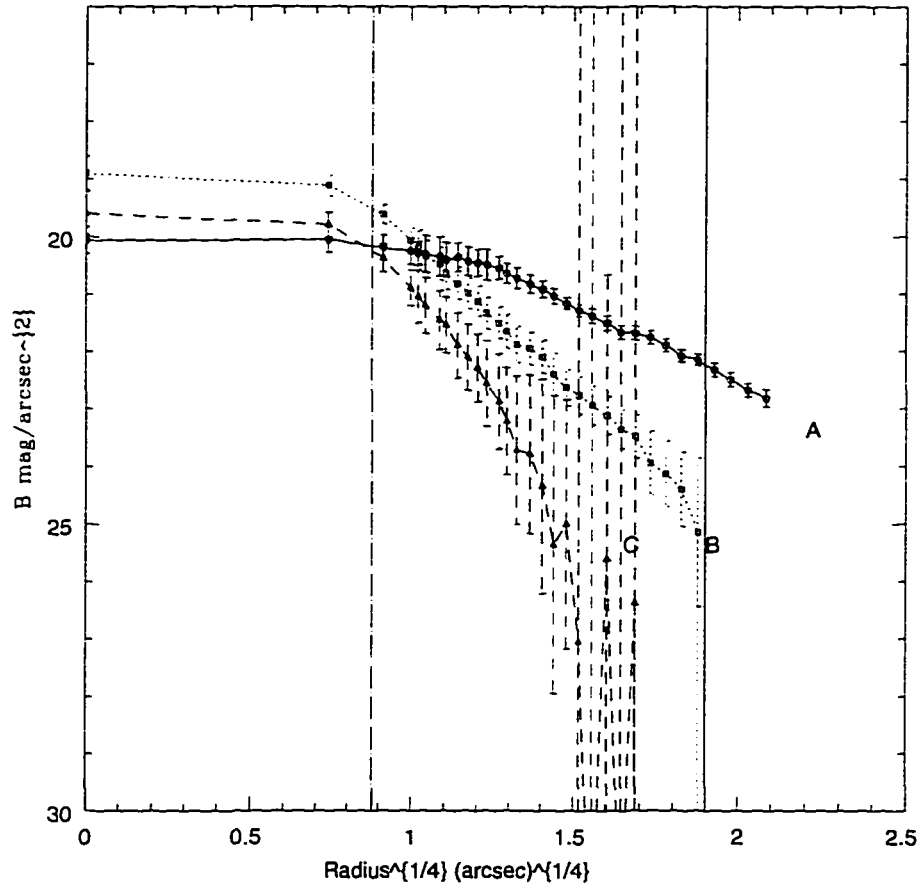


Figure 11: *B*-band surface brightness profiles for nuclei A, B and C computed from photometry of the CFHT Archive images. The brightness in *B* magnitudes per square arcsecond is plotted as a function of major axis position to the 1/4 power. All three nuclei are well fit to de Vaucouleurs laws. The vertical dot-dashed line shows the radius of the mean seeing FWHM. The vertical solid line shows the distance of nucleus B from nucleus A. The profiles of nuclei A, B and C are labeled.

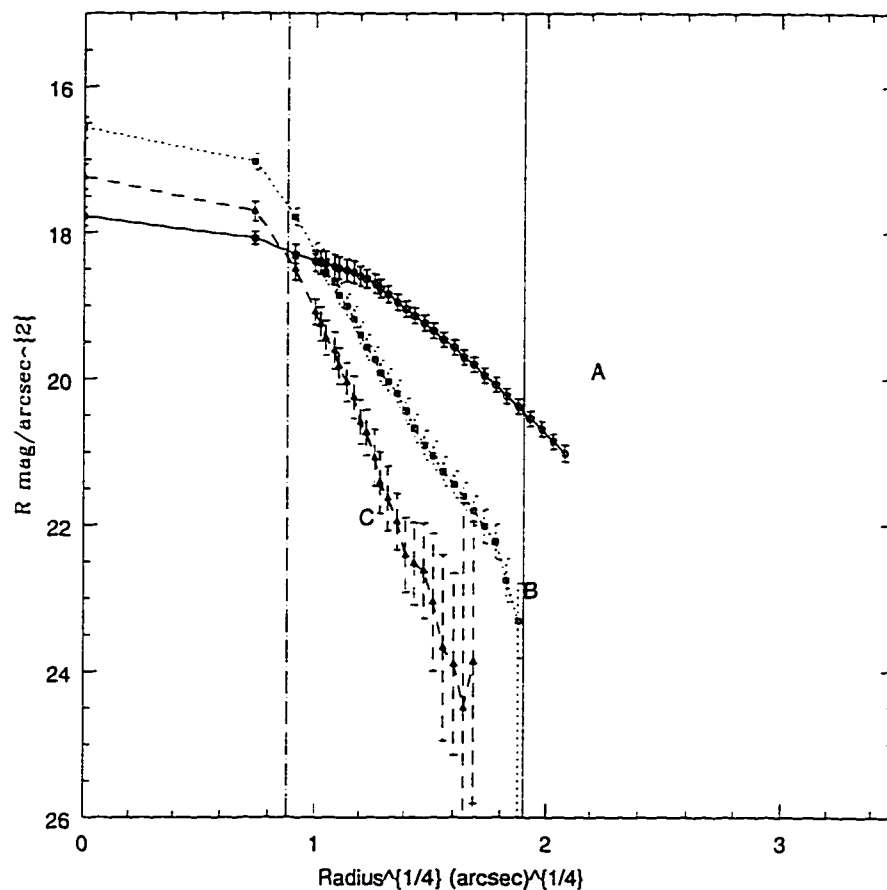


Figure 12: R -band major-axis brightness profile for nuclei A, B and C computed from photometry of the CFHT Archive images. The brightness in R magnitudes per square arcsecond is plotted as a function of major axis position to the $1/4$ power. Once again nucleus A is well fit to a de Vaucouleurs law, as indicated by the linear shape of the brightness profile. Nuclei B and C also are well fit to de Vaucouleurs laws with no significant sign of slope changes. The truncation indicated by Lauer (1986) is not evident. The vertical dot-dashed line shows the radius of the mean seeing FWHM. The vertical solid line shows the distance of nucleus B from nucleus A. The profiles of nuclei A, B and C are labeled.

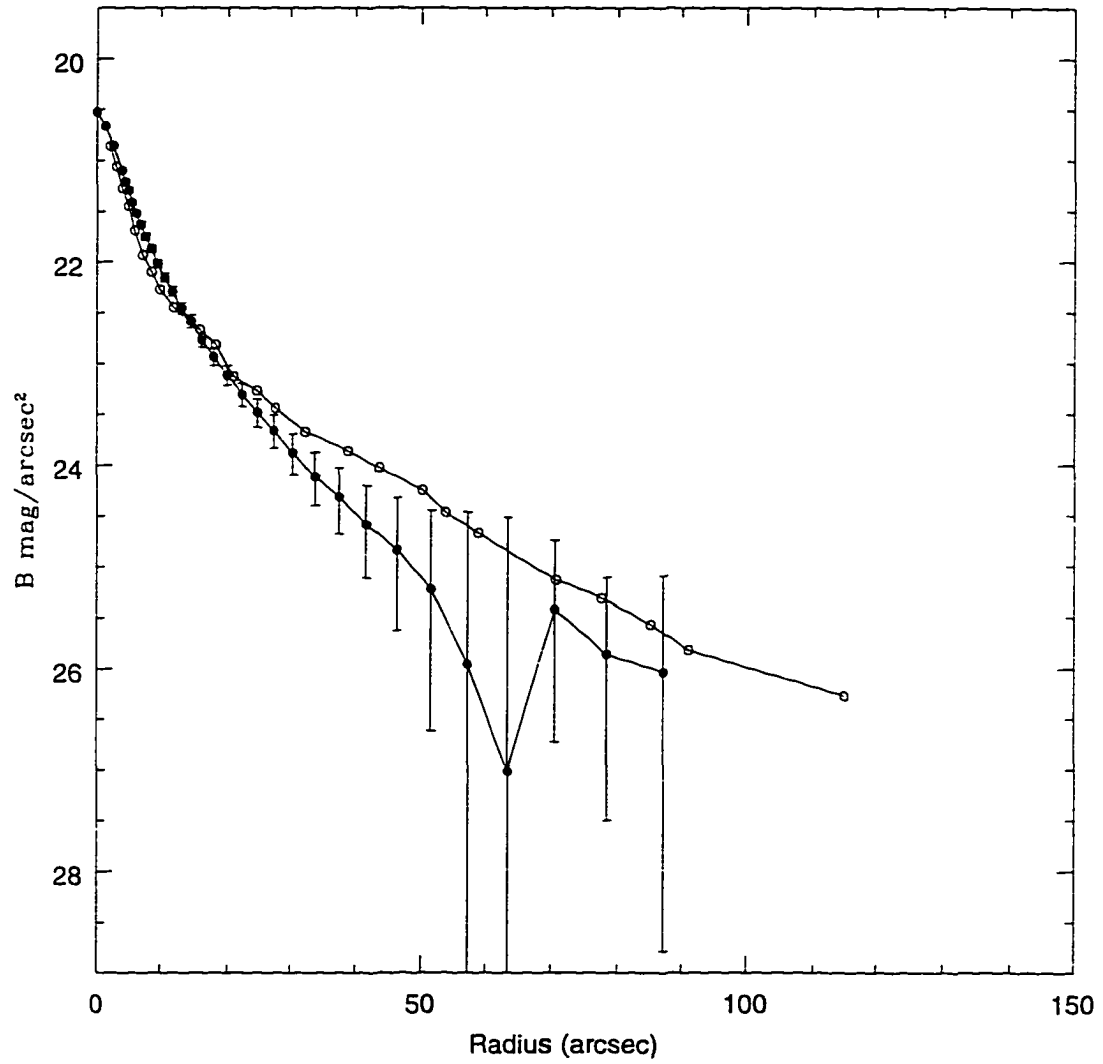


Figure 13: Comparison of our B -band surface brightness profile for nucleus A (filled circles) to that of Lachiéze-Rey *et al.* (1985) (hollow circles). Our profile is brighter in the inner regions, while fainter in the outer parts.

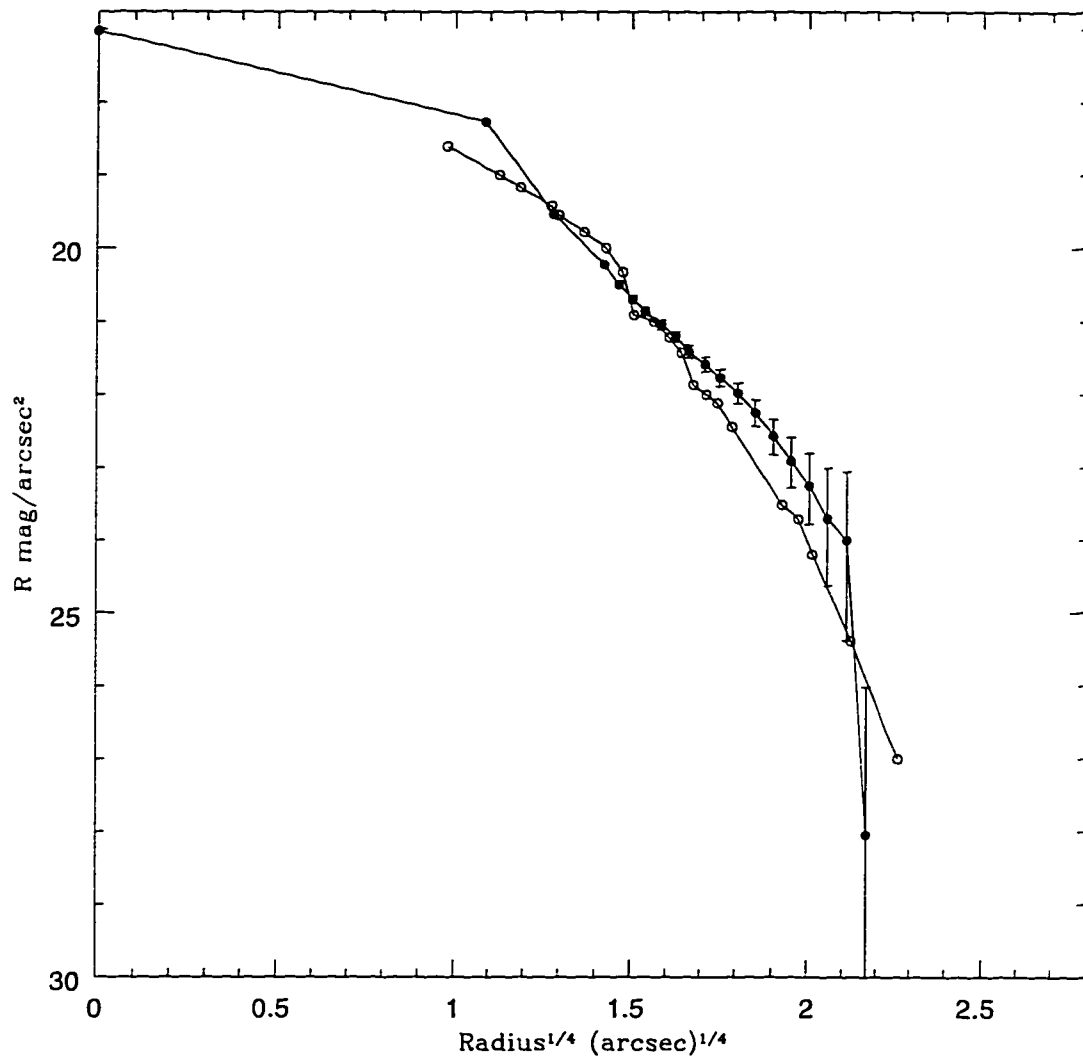


Figure 14: Comparison of our R -band surface brightness profile for nucleus B (filled circles) to that of Lachiéze-Rey *et al.* (1985) (hollow circles) . Our profile has a shallower slope than the Lachiéze-Rey *et al.* result. In addition, our profile is well fit to a De Vaucouleurs law, while their profile has a curved appearance, mimicking a truncated profile.

Where μ' is the mean ellipticity, σ_μ^2 is the variance in the mean ellipticity, and σ_i^2 is the variance in the i th measurement of the ellipticity for an isophote.

The uncertainty in the position angles is calculated using:

$$\sigma_\mu^2 = \sum [\sigma_i^2 (\frac{\partial \mu'}{\partial P_i})^2] \quad (17)$$

Where σ_μ^2 is the variance in the mean position angle, σ_i^2 is the variance in the i th position angle measurement, μ' is the mean position angle, and P_i is the i th position angle measurement.

Figures 17 and 18 compare our ellipticity and position angle profiles to those of Lauer (1986). The ellipticity profiles of nuclei B and C show an initial dip, and then an increase in ellipticity but neither shows changes in ellipticity that are larger than the uncertainties. Such trends are expected since seeing will circularize the isophotes near their centers. For nucleus A, there is excellent agreement in the ellipticity profiles of Lauer (1986) and this work. There is an initial dip and then a rise in ellipticity that continues along the entire profile. Lachiéze-Rey *et al.* (1985) also noted this behavior. Since Lauer's data was read off paper photocopies, there is some uncertainty introduced by us in the comparison. However, if Lauer's uncertainties are comparable to ours, the data would seem to agree in general shape for the three nuclei. However, we once again note that within the uncertainties no significant ellipticity changes are present.

The position angle data are in worse agreement (Figure 18) in the central regions of nucleus A. However, poor sampling of the galaxy because of finite size of the pixels, or seeing, or dust may be a problem. Once again, however, the position angle profiles

for nucleus C agree, assuming similar uncertainties for the Lauer (1986) data.

We expect that if nuclei B and C are interacting with nucleus A, then there would be isophote twisting and ellipticity changes with radius as the smaller galaxies are stretched and twisted in the tidal field of nucleus A. It would seem that there is evidence for ellipticity changes in nucleus C. However, given the large uncertainties, the changes are not greater than the uncertainties, and so may not be significant. Nucleus B shows a very flat position angle profile.

In Figures 19 and 20, we present the mean position angles and ellipticity profiles for all three nuclei measured on our CFHT archive images. These are the unweighted average of the ellipticities and position angles for our *B* and *R* archive images. The uncertainties are computed in the same manner as the uncertainties for our CFHT data. We indicate the seeing FWHM (vertical dot-dashed line) on all plots. Once again, nucleus A has a steadily increasing ellipticity profile with a strong initial decrease. Nuclei B and C show a decrease in ellipticity, as does nucleus C. The results for nucleus C therefore are opposite to that seen in Figure 15. The position angle seems to be constant for both nuclei as well, with large scatter. This leads to the suspicion that we are running into problems of light contamination from nucleus A, which would be a non-uniform background and thus affect the measured isophote shapes. The changes in nucleus C may be because we become more affected by contamination from nucleus A with radius. This makes measuring the ellipticities and position angles more uncertain.

The increase of ellipticity of nucleus C noted by Lauer (1986) may be explained

by the seeing making the isophotes more circular near the center, and the ellipticity then increasing as seeing effects decrease. We summarize by noting the position angle and ellipticity changes are not significant within the uncertainties and the effects of seeing and contamination may better explain them. Detailed modeling and testing would be required to confirm this.

7.2 Results From Aperture Photometry

7.2.1 Results From D_n Determinations

The values of D_n in arcseconds and the corrected total apparent B -band magnitudes, which we call B_{tot} , for nuclei B and C are given in Table 8, computed as described in Section 5.3. Burstein *et al.* (1987) give the values of B_{tot} and $\log(D_n/0.1')$ for 505 galaxies. In Figure 21 we plot these data along with the values determined for nuclei B and C from our study. Included in the Burstein *et al.* (1987) sample is NGC 4486A and its satellite galaxy NGC 4489B (labeled), as well as M32 (labeled), which is a small satellite galaxy of M31. Examining Figure 21, it appears that both M32 and NGC 4486B lie to the right of the mean line. M32 appears to be ~ 0.5 magnitudes away from the mean line, and NGC 4486B lies about 1.0 magnitude to the right of the relation.

While suggestive, there is large scatter in the plot, of the order of the difference in M32 and NGC 4486B from the mean relation. This may suggest that a certain amount of the scatter in Figure 21 is caused by the inclusion of tidally truncated galaxies. To address this issue properly, it would be valuable scientifically to identify those galaxies in the sample which are candidates for tidal truncation and remove

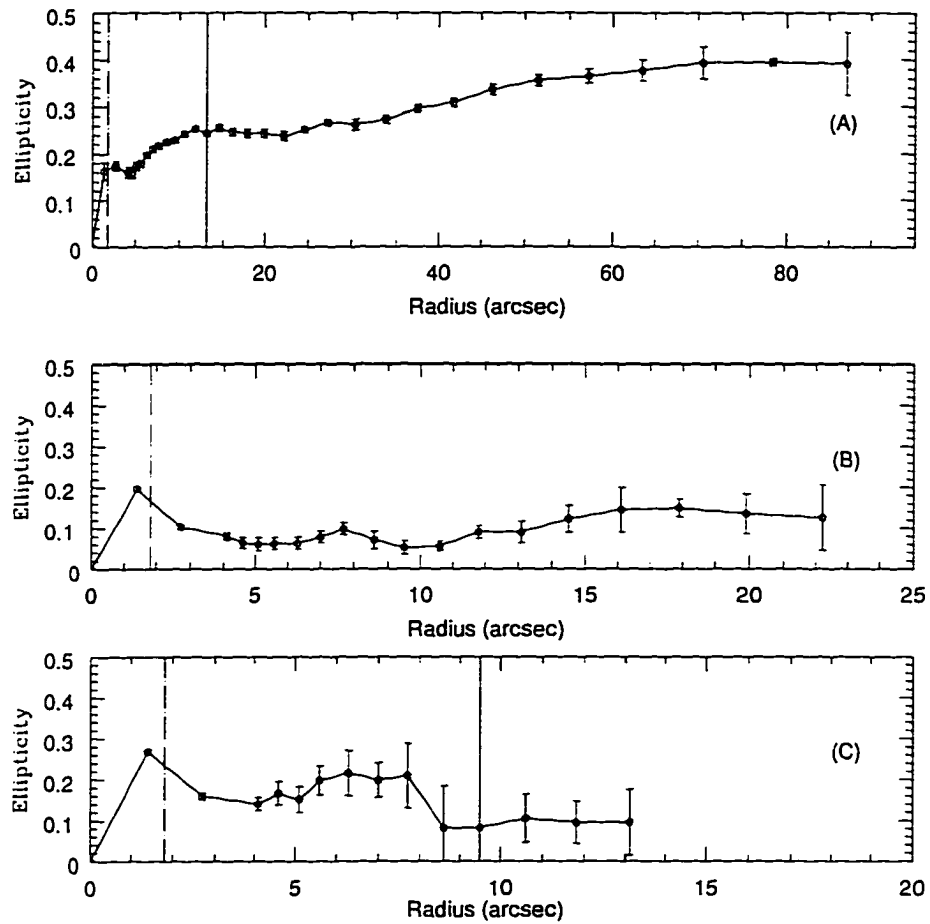


Figure 15: The mean ellipticity profiles of the three nuclei of the NGC 6166 system from our CFHT data; (A) the ellipticity profile of nucleus A, (B) the ellipticity profile of nucleus B, (C) the ellipticity profile of nucleus C. The ellipticity change of nucleus A, as reported by Lachi ze-Rey *et al.* (1985) is confirmed. Neither nucleus B or C show significant changes in ellipticity with radius. The vertical solid line in the plot of nucleus A shows the distance of nucleus B from nucleus A. The seeing FWHM is indicated on all three plots by the vertical dot-dashed line.

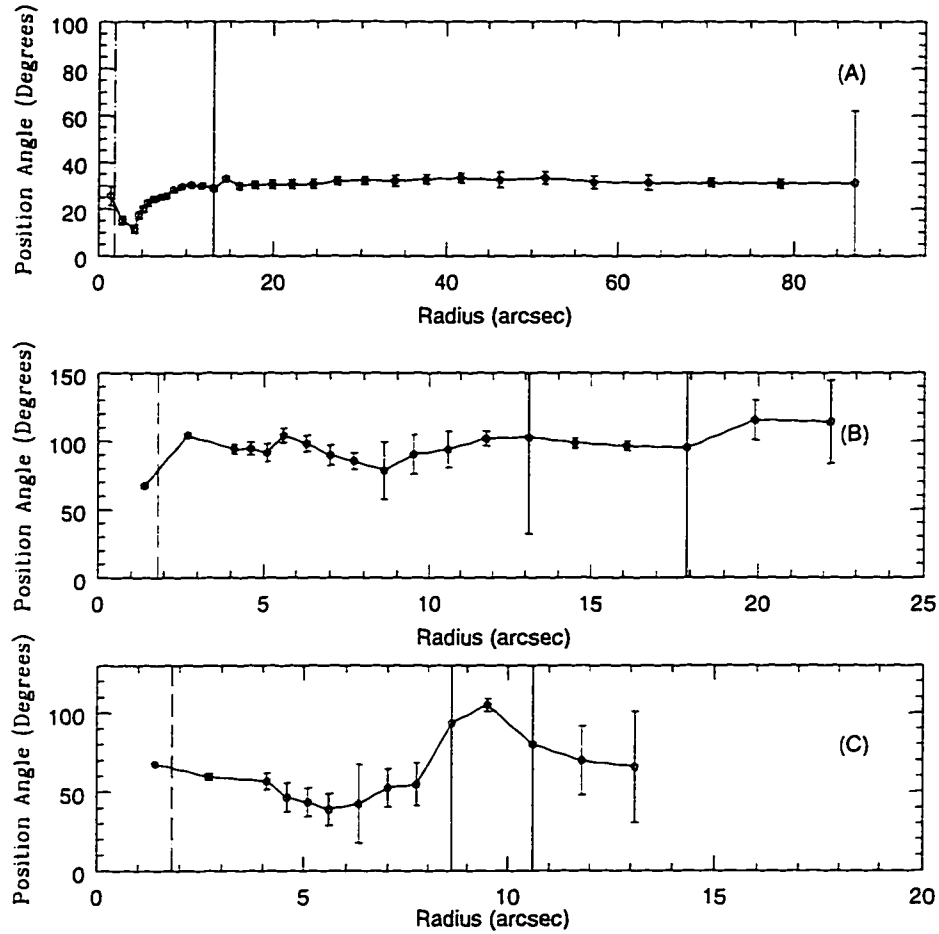


Figure 16: The mean position angle profiles of the three nuclei of the NGC 6166 system; (A) the position angle profile of nucleus A, (B) the position angle profile of nucleus B, (C) the position angle profile of nucleus C. Neither nucleus B or C show significant changes in position angle with radius. The changes in nucleus A may be due to dust absorption since the archive images also show these affects. The vertical solid line in the plot of nucleus A shows the distance of nucleus B from nucleus A. The seeing FWHM is indicated on all three plots by the vertical dot-dashed line.

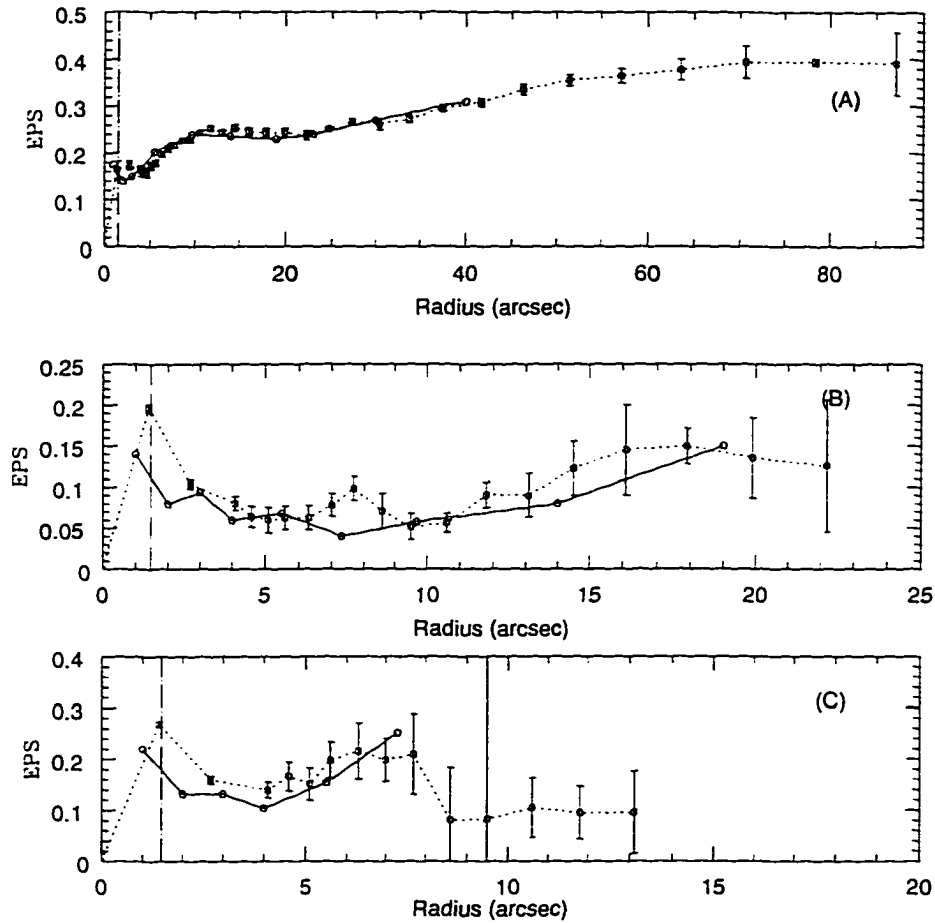


Figure 17: Comparison of our mean ellipticity profiles to that of Lauer (1986); (A) the ellipticity profile of nucleus A, (B) the ellipticity profile of nucleus B, (C) the ellipticity profile of nucleus C. For all three plots, our mean data are indicated by squares and are connected by solid lines. The Lauer (1986) data is indicated by the pentagons and dashed lines. The vertical dot-dashed line is the mean seeing FWHM. There is generally good agreement between our study and Lauer (1986).

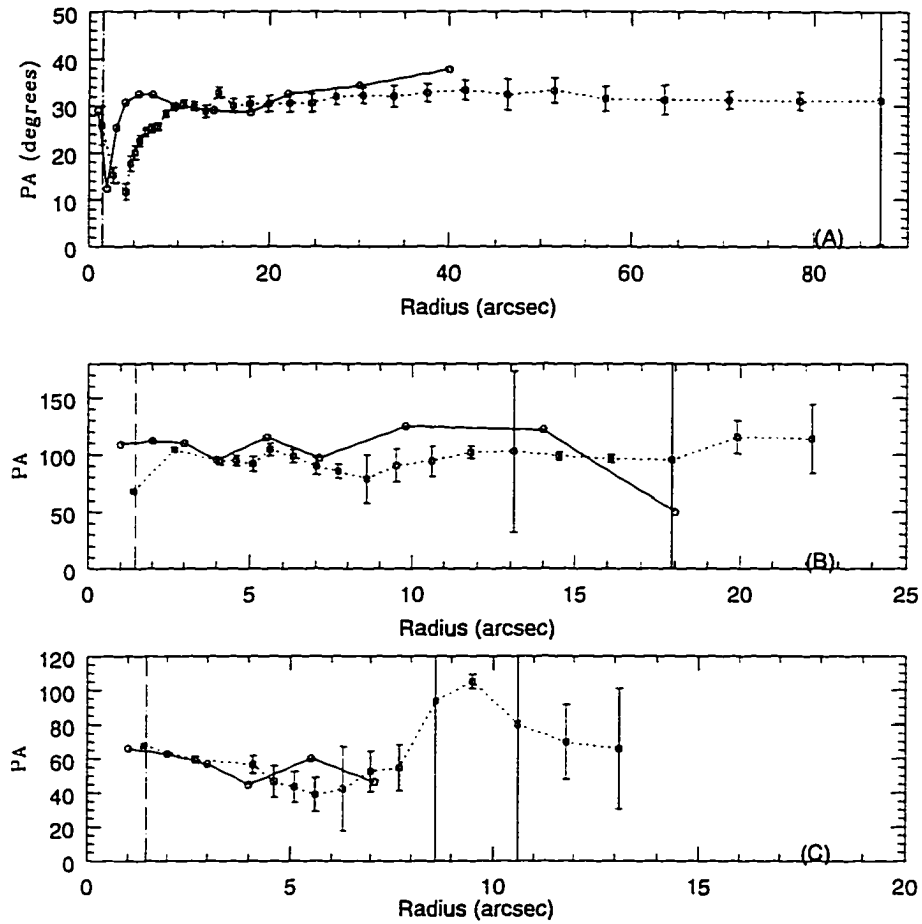


Figure 18: Comparison of our mean position angle profiles to that of Lauer (1986); (A) the position angle profile of nucleus A, (B) the position angle profile of nucleus B, (C) the position profile of nucleus C. For all three plots, our mean data are indicated by squares and are connected by dashed lines. The Lauer (1986) data is indicated by the pentagons and solid line. The vertical dot-dashed line is the mean seeing FWHM. There is poorer agreement between our study and Lauer (1986) than for the ellipticities, particularly in the central region of nucleus A.

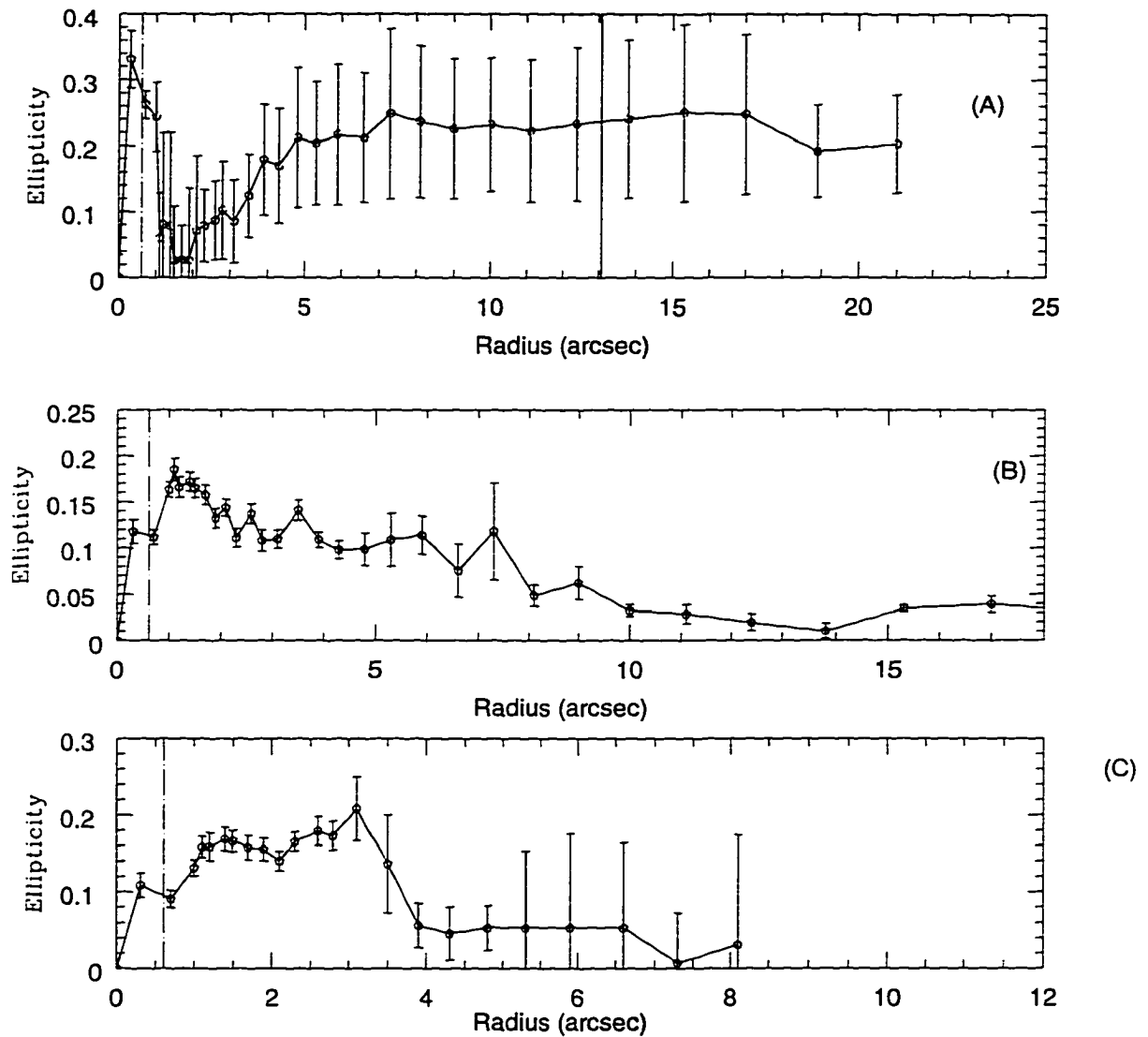


Figure 19: The mean ellipticity profiles measured on our CFHT archive images. (A) the ellipticity profile of nucleus A, (B) the ellipticity profile of nucleus B. (C) the ellipticity profile of nucleus C. The vertical dot-dashed line is the mean seeing FWHM. The vertical solid line in the plot of nucleus A shows the distance of Nucleus B from Nucleus A. The strong dip in the profile of nucleus A is recovered.

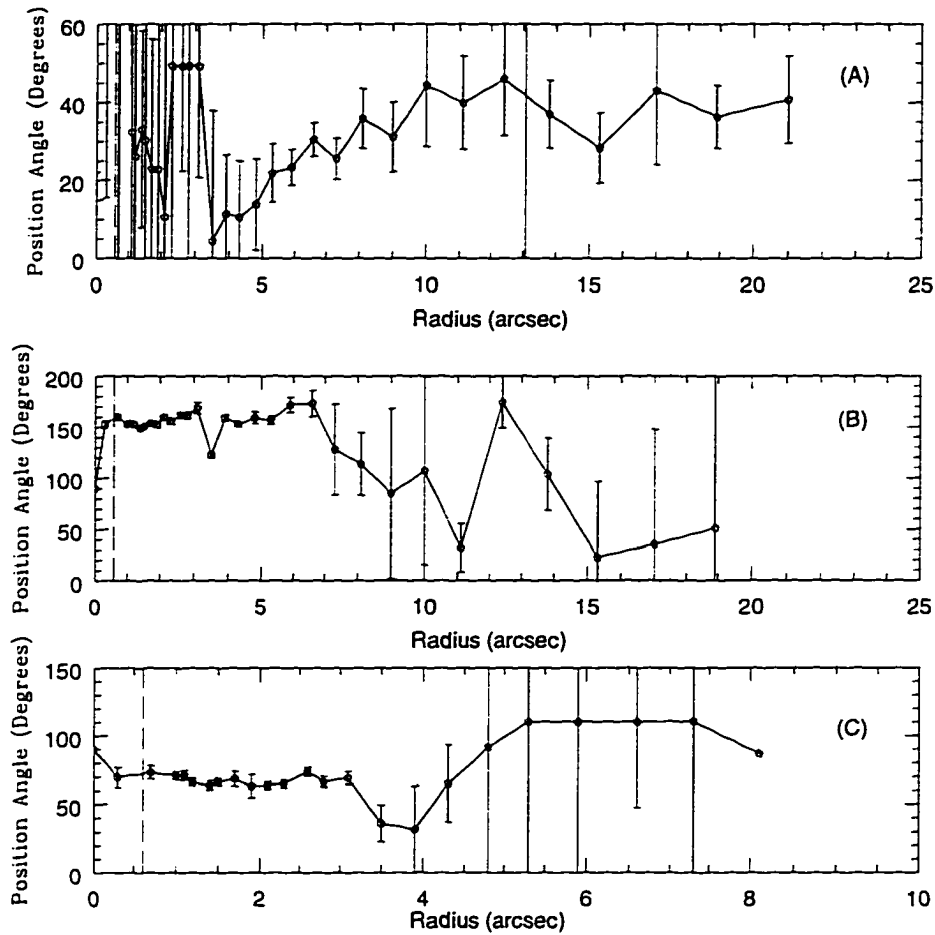


Figure 20: The mean position angle profiles measured on our CFHT archive images. (A) the position angle profile of nucleus A, (B) the position angle profile of nucleus B, (C) the position profile of nucleus C. The vertical dot-dashed line is the mean seeing FWHM. The vertical solid line in the plot of nucleus A shows the distance of Nucleus B from Nucleus A. There are no significant position angle changes in nucleus B or C. The strong dip in the profile of nucleus A is recovered.

Table 8: Results of D_n Determinations

B-image	Nucleus B		Nucleus C		Seeing
	D_n (")	B_{tot}	D_n (")	B_{tot}	FWHM (")
164	5.20	16.33	2.73	17.44	1.39
255	4.70	16.19	2.37	17.36	1.62
257	4.33	16.12	1.92	17.09	1.84

them. Figure 21 could then be replotted with only non-interacting galaxies included. This would be more valuable as a comparison sample for determining the value of the D_n parameter as a useful diagnostic for identifying merging galaxies. However, such a study is beyond the scope of this work.

With this difficulty in mind, it is still useful to examine whether nuclei B and C are similarly placed to the right of the mean relation or whether they are closer to the mean of the relation. From Table 8, we find the $B_{tot} = 16.26 \pm 0.03$ and the average $\log(D_n/0.1') = -0.09 \pm 0.02$ for nucleus B. For nucleus C $B_{tot} = 17.51 \pm 0.04$ and the average $\log(D_n/0.1') = -0.36 \pm 0.03$. Here the uncertainties are simply the standard deviations around the mean value. Inspection of Figure 21 shows that neither nucleus B nor C seems fainter for their D_n value, which suggests they are not being truncated by nucleus A. In addition, they are not too bright for their D_n value either, which suggests they are not being tidally shocked making them too large for their brightness (see discussion in Section 5.3). From this evidence it appears that both nuclei B and C are normal cluster ellipticals, and do not show signs of interaction with nucleus A.

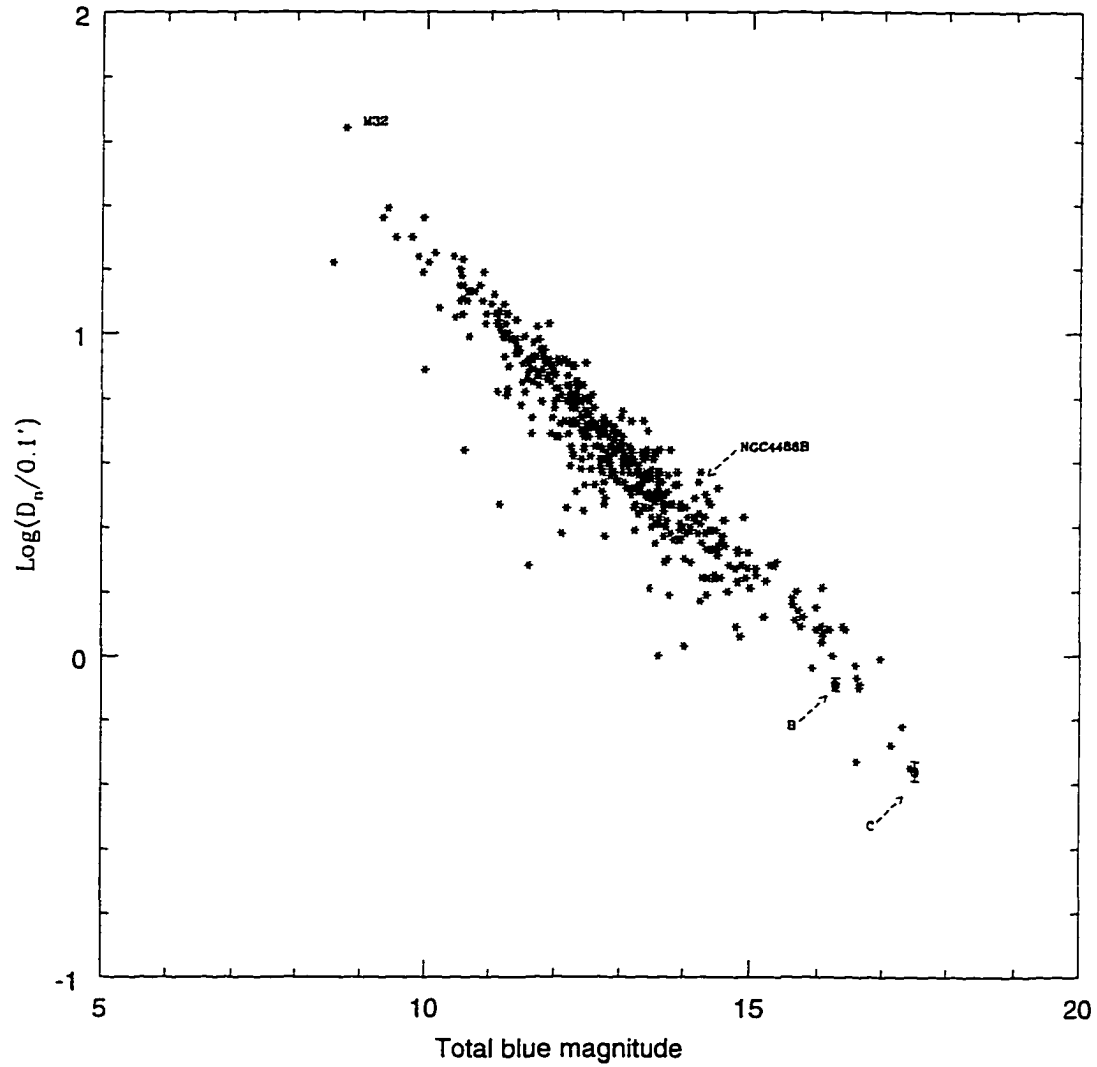


Figure 21: Plot of $\log(D_n/0.1')$ versus corrected total apparent B magnitude, B_{tot} , for nuclei B and C (pentagons), and the sample of Burstein *et al.* (1987). Significantly, nuclei B and C lie close to the relation defined by the Burstein *et al.* (1987) data. This suggests that nuclei B and C seem to internally show no evidence for being enlarged or truncated through interaction with the main galaxy.

Table 9: Global Colours of Nucleus B and C

Image	Nucleus B			Nucleus C		
	B_{tot}	R_{tot}	$B - R$	B_{tot}	R_{tot}	$B - R$
161/164	16.33	14.44	1.89	17.44	15.89	1.55
255/260	16.19	14.62	1.57	17.36	15.71	1.65
257/260	16.12	14.64	1.48	17.09	15.74	1.35

7.2.2 Global Colours Derived from Aperture Photometry.

We may derive global colours for the components of NGC 6166 by performing aperture photometry on the R -band images in an identical manner to that performed on the B -band data. The total R -magnitude for each nucleus is then available directly. Table 9 gives the total Cousins B and R band magnitudes, and the global colours for nuclei B and C.

For purposes of comparison with other authors, we once again transform our Cousins $B - R$ colours from Table 9 to the Johnson system using the transformations given by Davis *et al.* (1985). The colour of nucleus B is $B - R = 1.90 \pm 0.22$ while the global colour of nucleus C is $B - R = 1.75 \pm 0.15$. The uncertainties quoted here are the standard deviations around the mean of three determinations of each quantity. Lachi ze-Rey *et al.* (1985) find $B - R \sim 2$ for nucleus B, while the global colour of nucleus C is bluer by 0.4 magnitudes. We find a smaller difference, of only 0.15 magnitudes, but in the same sense that nucleus C is bluer than nucleus B. Within the uncertainties the two have the same colour. We wish to compare these results to those of typical spiral and elliptical galaxies. Peletier & Balcells (1996)

give $B - R$ determinations for the bulges of 30 spiral galaxies, while Peletier *et al.* (1990) provide $B - R$ colours for 39 elliptical galaxies. Figure 22 shows histograms of the $B - R$ colours of both data sets. The mean $B - R$ colour for the spiral bulges is $B - R = 1.44 \pm 0.13$, while the mean $B - R$ colour of the elliptical galaxies is $B - R = 1.57 \pm 0.09$. The elliptical galaxies are therefore slightly redder than the spiral bulges. There is also less scatter among the values for the elliptical galaxies, which is not surprising since the bulges must be measured separate from their disks – a difficult procedure. Based upon these values, it is not clear that nucleus C has a colour different from other elliptical galaxies. However, both nuclei B and C are redder than the mean for both the spirals and ellipticals.

In Figure 23 we show a colour-magnitude diagram for the sample of ellipticals and bulges. We obtain the total absolute B -band magnitudes for the ellipticals from Peletier *et al.* (1990). The values they quote are in turn calculated from the B -band data of Burstein *et al.* (1987), with $H_0 = 50 \text{ km s}^{-1} \text{ Mpc}^{-1}$. For the spiral galaxies, we obtain total B -band magnitudes and redshifts from de Vaucouleurs *et al.* (1991). Figure 23 shows the position for nuclei B and C so they may be compared to spiral and ellipticals of similar blue luminosities. There is large scatter, making meaningful comparison difficult. We adopt the velocities of Tonry (1984) for both nuclei B and C and compute their absolute magnitudes. Figure 23 shows that nuclei B and C are both very red objects, appearing redder than most ellipticals and spirals. The only spiral galaxy in the sample as red as nucleus C is NGC 6368, which is listed as an Sb galaxy by de Vaucouleurs *et al.* (1991). The results do not suggest that nucleus C is

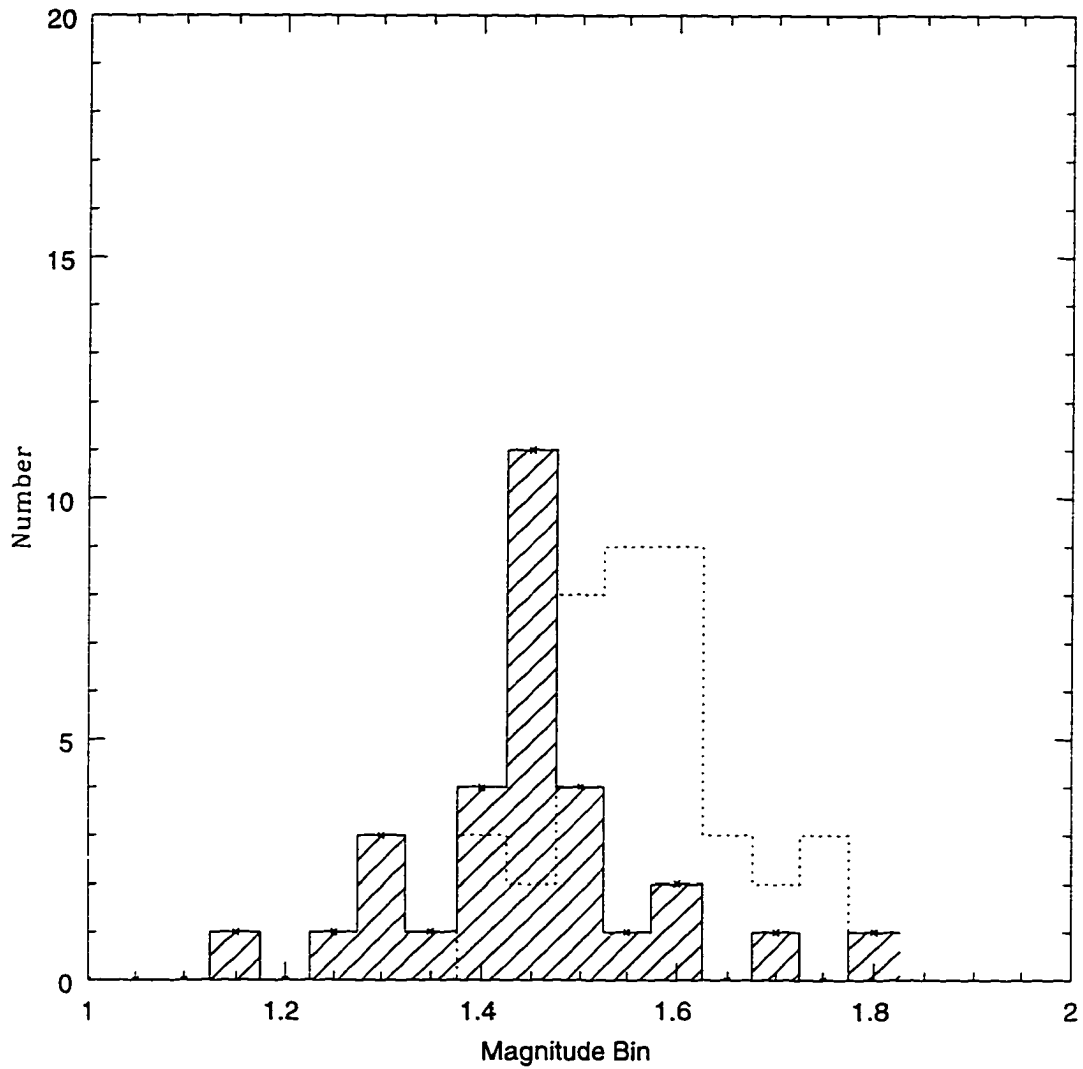


Figure 22: A histogram of the $B - R$ values of spiral bulges and elliptical galaxies. The shaded region delineates the histogram for the spiral galaxies, while the dotted line shows the histogram for the ellipticals. The colours for the bulges and ellipticals are very similar in $B - R$ colour, with the spiral bulges being slightly bluer. The data is plotted in 0.5 magnitude bins.

Table 10: Global Magnitudes and Colours of the Tidal Wake Candidate

Image Pair (<i>B</i> -image/ <i>R</i> -image)	B_{tot}	R_{tot}	$B - R$
161/164	21.62 ± 0.74	20.04 ± 0.47	1.58 ± 0.88
255/260	20.85 ± 0.51	19.23 ± 0.34	1.62 ± 0.61
257/260	20.61 ± 0.46	19.26 ± 0.34	1.36 ± 0.57

a stripped Sb galaxy, but this possibility cannot be ruled out.

7.2.3 Total Magnitudes and Colours of the Tidal Wake Candidate

We averaged the three *B*-band and two *R*-band magnitude determinations of the tidal wake candidate (see Section 5.3) to produce average total *B*- and *R*-band magnitudes and an average $B - R$ colour. Table 10 gives the results of our photometry of the wake.

The average *B*-band magnitude is 21.03 ± 0.30 , the average *R*-band magnitude is 19.51 ± 0.27 and the average $B - R$ is 1.52 ± 0.37 . Here the uncertainty estimates are computed in a similar manner to those of the mean ellipticity and position angle uncertainties. At the position of the wake, NGC 6166 has a $B - R = 1.75 \pm 0.07$. Comparing the mean $B - R$ colour for the wake with that for nucleus A at its position suggests that the cD may be slightly bluer than the wake candidate by ~ 0.22 magnitudes. However, given the large uncertainty in the colors of the tidal wake, this difference is not statistically significant.

Comparing the models of Weinberg (1986) for a dynamical wake, we note that the models require the spatial units to be in terms of GM_s/σ^2 . The absolute *B*-

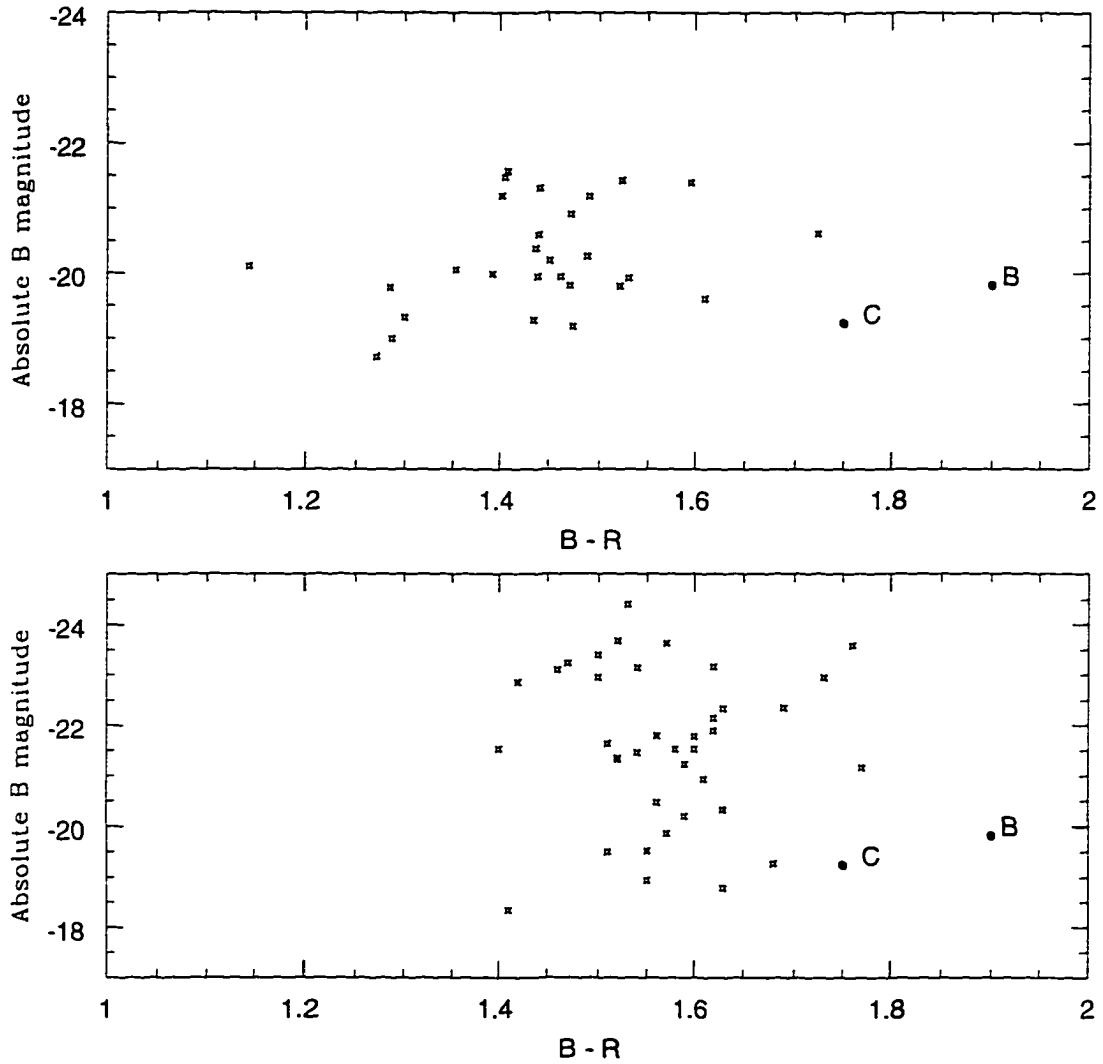


Figure 23: A comparison of the Johnson $B - R$ colour of nucleus B and C to spirals (top) and ellipticals (bottom) of the similar absolute Johnson B magnitude. It is clear here that the $B - R$ colours of nuclei B and C (labeled) are redder than other ellipticals. However, the samples show little trend of $B - R$ with magnitude for either the spirals or the ellipticals. The larger scatter in the spiral galaxies is evident.

band magnitude of nucleus B from our aperture photometry is -19.82 . The absolute blue magnitude of the Sun is 5.48 . Therefore the blue luminosity of nucleus B is $1.32 \times 10^{10} L_{\odot}$. Tonry (1984) uses $(M/L = 10M_{\odot}/L_{\odot})$, which yields a mass for nucleus B of $M_B = M_s = 1.32 \times 10^{11} M_{\odot}$. The velocity dispersion of nucleus A from Tonry (1984) is $\sigma = 303 \text{ km/s}$. Substituting in these quantities and converting meters to parsecs, the spatial unit of Weinberg is therefore equal to 6183 pc . The conversion from arcseconds to parsecs is done assuming a distance of 187 Mpc for NGC 6166. The center of the wake is at a distance of $r = 4.''77$ or 4325 kpc from the center of nucleus B. In the Wienberg (1985) model units $r = 0.699$.

We calculate the observed overdensity of the wake by using equation 11. The brightnesses of nucleus A in the B - and R -band are interpolated between the observed points of the average profiles. At the semi-major axis position corresponding to the center of the wake, $13.''2$, the interpolated B -band surface brightness of nucleus A is $22.48 \text{ mag/square arcsecond}$. The R -band surface brightness at this point is $20.75 \text{ mag/square arcsecond}$. The corresponding overdensities are 3.13 and 3.80 . The average overdensity is therefore $\xi \sim 3.47$. The theoretical model of Weinberg (1985) gives $\xi \sim 1.47$. Given the crudeness of our approximations, this should be considered good agreement.

However, one could argue that the wake could be an elliptical galaxy of the Abell 2199 cluster projected onto the central system. A certain number of such chance projections are expected (Tonry 1984), which is one of the motivating reasons for our photometric study. The key here is that the wake's axis seems to point towards the

center of nucleus B. To see how likely the possibility would be for a chance projection to occur in such a manner we conducted a Monte Carlo simulation. This may be tested using the fact that in order for a projected galaxy to point towards nucleus B, the position angle of the major axis of the projected galaxy must be the same as the position angle formed by the center of the galaxy and nucleus B.

Our Monte Carlo simulation assumed that a cluster elliptical was projected within 90 pixels ($0.''70$) of the center of nucleus A. This is the approximate size of the region enclosing nuclei A, B and C on our images. A random number generator was then used to give a group of 10000 galaxies random positions and position angles. Next, all simulated galaxies which lay in box of the same dimensions and position as our wake candidate were identified. The position angle between each such object and nucleus B was then calculated. All simulated galaxies which had a position angle within ten degrees of that formed by the center of the galaxy and nucleus B were considered to be a match to our wake. It was found that the chances of such a galaxy being projected at the correct orientation was $\sim 0.1\%$. This result argues in favor of the tidal wake candidate being physically associated with nucleus B, possibly a tidal wake formed by the passage of nucleus B through the halo of nucleus A. Similar features have been noted in other multiple nucleus systems (Lauer 1988; Blake & West 1996).

7.3 Dust Morphology and Mass Estimate.

7.3.1 The Dust Morphology of NGC 6166

We show a map of all the pixels which survived our dust selection criteria in Figure 24. The dust seems to lie in three main regions, which we have labeled Dust Blob 1, the

Table 11: Properties of Detected Dust Features

Dust Feature	Mean Absorption	Total Mass (M_{\odot})
Dust Blob 1	0.013	2.1×10^3
Sinusoidal Dust Blob	0.02	2.2×10^4
Dust Blob 3	0.085	6.8×10^4

Sinusoidal Dust Blob, and Dust Blob 3. Examination of the CFHT Archive images suggests that the Sinusoidal Dust Blob may extend further to the southwest, but this is uncertain. Dust Blob 1 is also easily evident in the CFHT Archive images. The Sinusoidal Dust Blob is the dust feature identified by Minkowski (1961) and Lauer (1986). Dust Blob 3 is the largest in size, and was first identified by Lauer (1986). One interesting aspect of this feature is that it seems to lie on the opposite side to nucleus C. This leads to the suspicion that it could be caused by non-elliptical isophotes or an algorithm induced effect created by the **SNUC** fitting and the **RENUC** model reconstruction. We are able to rule out the latter, by examining the residuals left after we fit model images created in Section 3.4 using **SNUC** and then using **RENUC** to reconstruct the model galaxies. Subtracting the **RENUC** model from the original model image shows no such deep oversubtracted region. This leads to the conclusion that the deep oversubtracted region is real structure in NGC 6166.

If the deep absorption region to the north is caused by dust then its mean absorption should be similar to the mean absorption of the two other dust features and dust lanes in other galaxies. Table 11 gives the mean B -band absorption and masses for our three dust features.

It is clear that Dust Blob 3 is the most massive and has the deepest absorption of the three. Its absorption is four times higher than the other two features. This makes it difficult to understand why it is not visible on the images. If smaller, less deep patches of absorption are visible, then a large, deep patch should be readily apparent. The fact that the smaller features have less absorption can be understood perhaps by the fact that seeing will affect smaller, more narrow features more than a larger dust cloud. The absorption of the two smaller dust clouds may therefore be underestimated, as light from the galaxy is smeared into them. Thus their contrast with the galaxy light will be less than if they were larger and less affected by the seeing. However, this still does not explain why the larger dust feature is not seen. It may be because it is more central, where the light from the galaxy is brightest. The seeing smears the light of the galaxy there as well, and since the galaxy is brightest there, the large amount of light smeared around the center makes the dust feature less prominent. However, these arguments are speculation.

Comparing the absorption of our features to those of Gallagher & Hunter (1981) for M31 and NGC 185 dust clouds, they find absorptions in the Johnson *B* band ranging between 0.07 and 0.01 magnitudes for dust in M31 and 0.24 magnitudes for dust clouds in NGC 185. Hodge (1973) provides average absorption values in the Johnson V-band for dust clouds in the galaxy NGC 205 of between 0.10, 0.11 and 0.20 magnitudes for three dust clouds in NGC 205. Thus our absorption values are comparable to those of dust clouds in other early-type galaxies. However, once again, the absorption values may be underestimated because of the effects of seeing.

7.3.2 Results of the Dust Mass Calculations

We have computed the dust mass for NGC 6166 from optical absorption as described in Chapter 6. The dust mass may also be computed from data from the IRAS fluxes measured for NGC 6166. Welch (1996), using the procedure outlined in Fich & Hodge (1991), and the IRAS fluxes of Knapp *et al.* (1989) obtains for the dust mass of NGC 6166:

$$M_D \sim 7.8 \times 10^6 M_\odot \times (D/100)^2. \quad (18)$$

Where M_D is the dust mass in solar masses, and D is the distance in megaparsecs. For an assumed distance of 187 Mpc, we get a dust mass of $2.7 \times 10^7 M_\odot$. Welch (1996) estimates this value to be uncertain by 50%.

We find the total dust mass for NGC 6166 from optical absorption to be $\sim 7.0 \times 10^5 M_\odot$. Van Dokkum & Franx (1995), used a similar procedure based upon optical extinction in the V -band to compute a dust mass for NGC 6166. They estimate a dust mass for NGC 6166 of $\sim 1.2 \times 10^4 M_\odot$, which is 70 times smaller than our value for the total dust mass. However, they measured only the dust from the Sinusoidal Dust Blob (Van Dokkum 1996). Since we also measure the large feature to the north of nucleus A, our estimate is much higher. However, our mass of the Sinusoidal Dust Blob of $2.2 \times 10^4 M_\odot$ is in good agreement with the value of van Dokkum & Franx (1995) for that feature. Van Dokkum (1996) indicates that agreement within a factor of two should be considered as excellent agreement between the two determinations.

It is better to compare dust masses obtained from IRAS measurements to masses obtained for other elliptical and spiral galaxies in the same manner. We compute

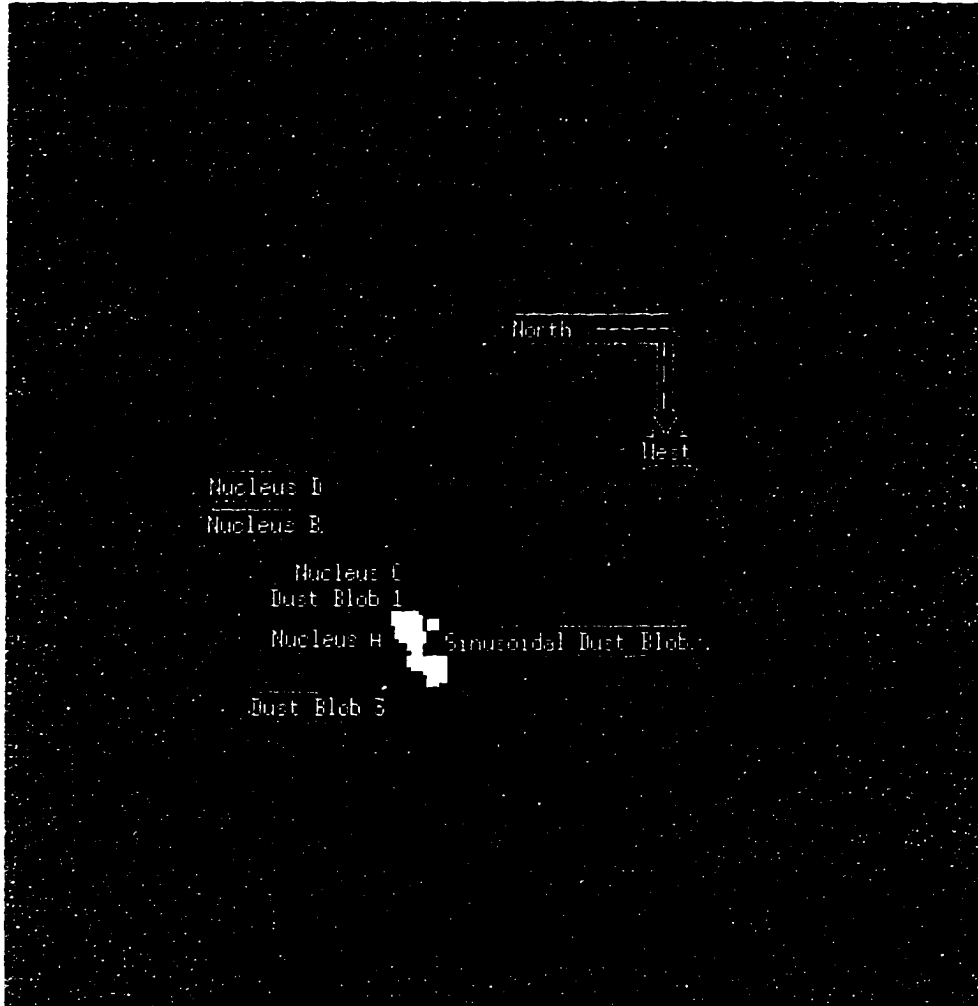


Figure 24: A map of all pixels surviving the dust selection process. The position of Nucleus A, B C and D are indicated. The shaded regions show the extensive dust regions near the center of nucleus A, which appear in three main regions. Dust Blob 1 is light grey, the Sinusoidal Dust Blob is white, and Dust Blob 3 is in dark shading. North is to the left and West is to the bottom. The field shown is $96'' \times 89''$.

an average dust mass for spirals using the data of Devereux & Young (1990), who used IRAS fluxes to compute the dust mass of 58 spirals. We find an average dust mass for their sample of $5.9 \times 10^6 M_{\odot}$. Goudfrooij & de Jong (1995) provide dust mass estimates for 56 elliptical galaxies based upon IRAS fluxes. The mean mass in this sample is $1.3 \times 10^6 M_{\odot}$. Figure 25 shows histograms of the log of the dust mass for the ellipticals and spirals in each sample. It is apparent that NGC 6166 is a very dusty galaxy, and lies outside the range occupied by the ellipticals. We see that NGC 6166 has a very large amount of dust even when compared to spiral galaxies. We indicate the position of NGC 6166 on this diagram. It should be noted that neither van Dokkum & Franx (1995) nor Goudfrooij & de Jong (1995) find any relation between total magnitude of the ellipticals and the dust mass. Therefore our comparison of NGC 6166, a supergiant galaxy to fainter ellipticals is legitimate. The dust mass estimate from IRAS fluxes is high for an elliptical galaxy (van Dokkum 1996) and is more consistent with a spiral galaxy than an elliptical.

It is also interesting to address the question of why the mass from IRAS fluxes is in our case a factor of 10 higher than the mass obtained from optical extinction. Clearly, any identification of dust based upon examination of images on a display is prone to error and small dust blobs of low contrast will be missed. However, Goudfrooij & de Jong (1995) have examined such effects and found that the optically determined dust masses are usually about 10 times less when compared to the IRAS estimates. They suggest that there is a diffuse component to the dust in the ellipticals, in addition to the discrete dust clouds. Our result for NGC 6166 may indicate that this discrete

component exists in NGC 6166.

Of primary interest in our study is the question of whether the dust seen in the center of NGC 6166 could have come from dust captured from nucleus C. Our dust mass estimates of $2.7 \times 10^7 M_\odot$ from IRAS fluxes, and $\sim 7.0 \times 10^5 M_\odot$ from optical absorption should be compared with the dust mass for spirals. As already discussed, we find an average dust mass for the spirals of $5.9 \times 10^6 M_\odot$ from Devereux & Young (1990). Therefore, since we get larger values for the dust mass than for a typical spiral, the data is consistent with some component of the dust being captured. The Sinusoidal Dust Blob alone for instance, which may represent material spiraling into the center of the central galaxy has a dust mass of $2.2 \times 10^4 M_\odot$. This is much smaller than the mass of a spiral. So we find that most of the dust in NGC 6166 is probably from the central galaxy its self. Still, it is more dusty than average, so some amount of captured dust being present cannot be ruled out.

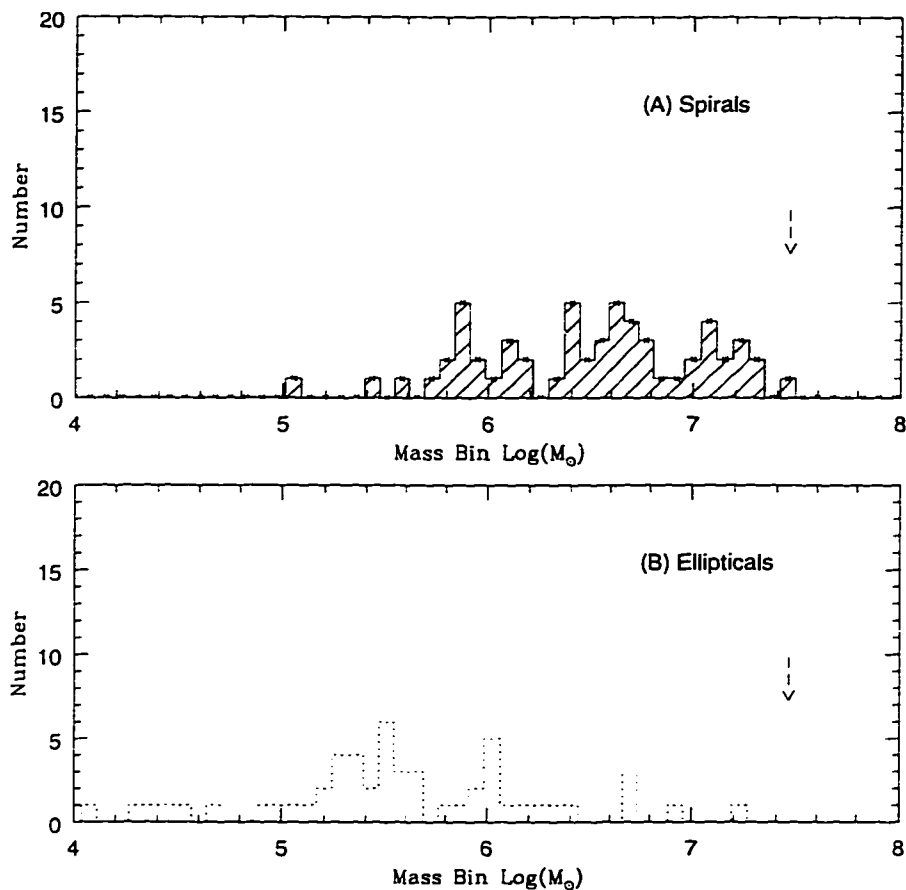


Figure 25: A histogram comparing the IRAS dust mass for spirals and ellipticals. The top plot shows the histogram of $\log(\text{mass})$ for the data of Devereux & Young (1990) for 57 spirals. The bottom plot shows the corresponding histogram for the sample of 56 elliptical galaxies from Goudfrooij & de Jong (1995). The arrow on both plots indicates the position of NGC 6166 from our IRAS dust mass. There is large scatter in both histograms, but the spirals have higher average dust masses than the ellipticals. NGC 6166 must be considered a very dusty galaxy, and lies on the upper limits of both distributions.

8 Conclusions

8.1 Summary

The results from our photometry are consistent with the NGC 6166 system being composed of the large central cD galaxy, nucleus A, and two cluster galaxies passing through the center of the cluster. Nuclei B and C do not show significant ellipticity or position angle changes expected if these galaxies are being cannibalised. While there is marginal evidence for ellipticity changes in nucleus C, they are not at a significant level. In addition, nucleus C is bluer than nucleus B, by about 0.15 magnitudes, which confirms the previous observations of Lachiéze-Rey *et al.* (1985). The colours for both nucleus B and C are more similar to elliptical galaxies than spirals, although we cannot rule out the suggestion that nucleus C is a stripped spiral.

The computed dust mass of the central galaxy is $\sim 7.0 \times 10^5 M_\odot$ from optical absorption, and $2.7 \times 10^7 M_\odot$ from IRAS fluxes. Our optical estimate is larger than previous estimates, which included only the Sinusoidal Dust Blob. Our mass for that feature, $2.2 \times 10^4 M_\odot$ agrees well with the mass determined by van Dokkum & Franx (1990) of $\sim 1.2 \times 10^4 M_\odot$. We find that the dust mass from optical absorption is 40 \times smaller than that computed from IRAS fluxes, which supports the results of Goudfrooij and de Jong (1995) that there may be a diffuse component to the dust in elliptical galaxies.

The large absorption feature to the northwest of nucleus A which was first identified by Lauer (1986) would seem to be the deepest absorption feature, and it is difficult to understand why it is missed by visual inspection. Two smaller, less deep

absorption regions are seen. The dust mass of NGC 6166 very is high, in any event, and is more like that of a spiral galaxy. Our results do not rule out the scenario where nucleus C is a stripped spiral and nucleus A is accreting material from it. Therefore nucleus C could be a cluster spiral which has been stripped of its disk during its passage through the cluster core. The colour of nucleus C is similar to a red Sb galaxy, but is most similar to that of the ellipticals.

Finally, nucleus B is likely creating a tidal wake behind it. The tidal feature indicated by Lauer (1986) is not likely to be a projected cluster galaxy, as our Monte Carlo simulation shows. Its colour is also consistent with it being formed from the halo of nucleus A. Our crude calculation of the overdensity of this feature based upon the models of Wienberg (1986) shows order of magnitude agreement with the values we calculate from our images.

The picture of the system is that of a group of three physically interacting galaxies. Nucleus B seems to be producing a tidal wake behind it, and nucleus C seems to be another cluster elliptical. The lack of internal structural changes in the smaller galaxies argues in favor of an interaction in its early stages, as suggested by Lauer (1986).

8.2 Future Work

In the future, a larger sample of multiple nucleus systems should be studied in detail to examine whether structural changes, if any, are present. It would be useful to examine in detail the effectiveness of the D_n parameter to identify galaxies being cannibalised. Creating a sample of galaxies uncontaminated by possible stripped

systems and comparing multiple nucleus candidates to the uncontaminated sample would be extremely useful in this regard. This might help determine if multiple nucleus systems are systematically different from other ellipticals.

Finally, a systematic study of the correlation of dust in cD galaxies is warranted. NGC 6166 has a large dust mass when computed from IRAS measurements, more like spiral galaxy masses. It would very valuable to see if this is a common property of cD galaxies.

References

Abell, G. O., 1958, ApJSS, **3**, 211.

Beers, T. C., & Tonry, J. L., 1986, ApJ, **300**, 557.

Blake, R. M., & West, M. J., 1997 In Preparation.

Blakeslee, J. P., & Tonry, J. L., 1992, AJ, **103**, 1457.

Bothun, G. D. & Schombert, J. M., 1990, **360**, 436.

Brosch, N., Almozino, E., Grosbol, P., & Greenberg, J. M., 1990., A&A, **233**, 341.

Brosch, N., & Loinger, F., 1991, A&A, **249**, 327.

Burns, J. O., Schwendeman, E., & White, R. A., 1983, ApJ, **271**, 575.

Burstein, D., Davies, R. L., Dressler, A., Faber, S. M., Stone, R. P. S., Lynden-Bell, D., Terlevich, R. J., & Wegner, G., 1987, ApJSS, **64**, 601.

Christian, C.A., Adams, M., Barnes, J.V., Butcher, H., Haynes, D.S., Mould, J.R. & Seigel, M. , 1985, PASP, **97**, 363.

Davis, L. 1989, personal communication.

Davis, L. E., Cawson, M., Davies, R. L., & Illingworth, G., 1985, ApJ, **90**, 169.

de Vaucouleurs, G., 1948, Ann. D'Astrophys., **11**, 247.

de Vaucouleurs, G., de Vaucouleurs, A., & Corwin, H. G., 1976, *Second Reference Catalogue of Bright Galaxies*, University of Texas Press.

de Vaucouleurs, G., de Vaucouleurs, A., Corwin, H. G., Buta, R. J., Paturel, G., & Fouque, P., 1991, *Third Reference Catalogue of Bright Galaxies*, Springer-Verlag.

Devereux, N. A., & Young, J. S., 1990, ApJ, **359**, 42.

Durrell, P., 1995, personal communication.

Feretti, L., Comoretto, G., Giovannini, G., Venturi, T., & Wehrle, A. E., 1993, ApJ, **408**, 446.

Fich, M. & Hodge, P., 1991, ApJ, **374**, L17.

Gallagher, J. S., & Hunter, D. A., 1981, ApJ, **86**, 1312.

Gallagher, J. S., Faber, S. M. & Burstein, D., 1980, ApJ, **235**, 743.

Gilliland, R. L., 1992, In *Astronomical CCD Observing and Reduction Techniques*, ASP. Conference. Series No. 23, P.68.

Goudfrooij, P., & de Jong, T., 1995, A&A, **298**, 784.

Hausman, M.A., & Ostriker, J. P., 1978, ApJ, **224**, 320.

Hodge, P. W., 1973, ApJ, **182**, 671.

Howell, S., 1989, PASP, **101**, 616.

King, I. R., 1971, PASP, **83**, 188.

Knapp, G. R., Guhathakurta, P., Kim, D.-W., & Jura, M., 1989, ApJSS, **70**, 329.

Lachiéze-Rey, M., Vigroux, L., & Souviron, J., 1985, A&A, **150**, 62.

Lauer, T.R., 1986, ApJ, **311**, 44.

Lauer, T.R., 1988, ApJ, **325**, 49.

Matthews, T. A., Morgan, W. W., & Schmidt, M., 1964, ApJ, **140**, 35.

Merrifield, M. R., & Kent, S. M., 1991, AJ, **101**, 783.

Merritt, D., 1984, ApJ, **276**, 26.

Mihalas, D., & Binney, J., 1981, *Galactic Astronomy*.

Minkowski, R. P., 1961, AJ **66**, 558.

Morgan, W. W., Kayser, S., & White, R. A., 1975, ApJ, **199**, 545.

Morgan, W.W., & Lesh, J. R., 1965, ApJ, **142**, 1364.

Oemler, A. 1976, ApJ **209**, 693.

Ostriker, J.P., & Hausman, M.A., 1977, ApJ, **217**, L129.

Peletier, R. F., & Balcells, M., 1996, AJ, **111**, 2238.

Peletier, R. F., Davies, R. L., Illingworth, G. D., Davis, L. E., & Cawson, M., 1990, *AJ*, **100**, 1091.

Rood, R.H., & Leir, A. A., 1979, *ApJ*, **231**, L3.

Rood, H. J., & Sastry, G. N., 1971, *PASP*, **83**, 313.

Sandage, A. R., Kron, R. G., & Longair, M. S., 1995, *The Deep Universe*, Springer Press.

Sarazin, C. L., 1988, *X-ray Emission from Clusters of Galaxies*, Cambridge Press.

Schneider, D. P., Hoessel, J. G., & Gunn, J. E., 1983, *ApJ*, **264**, 337.

Schombert, J., 1996, Private Communication.

Silk, J., Djorgovski, S., Wyse, R. F. G., & Bruzual, G. A., 1986, *ApJ*, **307** 415.

Stetson, P. B., 1987, *PASP*, **99**, 191.

Stetson, P. B., 1990, *PASP*, **102**, 932.

Struble, M. F., & Rood, H. J., 1981, AJ, **87**, 7.

Tonry, J. L., 1984, ApJ, , 13.

Tonry, J.L., 1985a, ApJ, **291**, 45.

Tonry, J. L., 1985b, AJ, **90**, 2431.

van Dokkum, P. G., 1996, Private Communication.

van Dokkum, P. G., & Franx, M., 1995, AJ, **110**, 2027.

Veron-Cetty, M.-P., & Veron, P., 1988, A&A, **204**, 28.

Weinberg, M. D., 1986, ApJ, **300**, 93.

Weinberg, M. D., 1996, Preprint.

Welch, G. A., 1995, Private Communication.

Welch, G. A., 1996, Private Communication.

White, S. D. M., 1976, MNRAS, **174**, 19.

9 Appendix A

Journal of Observations

Table 12: Night 1 May 3/4 1984 Observations

Image	UT	Exposure	Filter	Target
129xxx.fits	04:30:12.3	60	R	flat
130xxx.fits	04:30:12.3	60	R	flat
131xxx.fits	04:30:12.3	90	B	flat
132xxx.fits	04:30:12.3	90	B	flat
133xxx.fits	04:30:12.3	0	NA	Bias
134xxx.fits	04:30:12.3	0	NA	Bias
138xxx.fits	07:08:38.6	30	B	NGC4147
139xxx.fits	07:19:12.3	90	B	NGC4147
140xxx.fits	07:26:06.8	60	R	NGC4147
144xxx.fits	04:30:12.3	0	NA	Bias
145xxx.fits	04:30:12.3	0	NA	Bias
146xxx.fits	04:30:12.3	0	NA	Bias
155xxx.fits	11:15:33.8	60	B	NGC4147
156xxx.fits	11:19:30.1	60	R	NGC4147
157xxx.fits	04:30:12.3	60	NA	Bias
158xxx.fits	04:30:12.3	60	NA	Bias
159xxx.fits	12:07:29.8	60	R	NGC6166
160xxx.fits	12:35:11.9	60	R	NGC6166
161xxx.fits	12:40:20.9	900	R	NGC6166
162xxx.fits	13:01:34.8	900	R	Sky1
163xxx.fits	13:19:02.4	1200	B	Sky1
164xxx.fits	13:42:35.3	1200	B	NGC6166
165xxx.fits	04:30:12.3	60	NA	Bias
167xxx.fits	14:18:59.4	120	B	M92
168xxx.fits	14:24:31.0	120	R	M92
169xxx.fits	14:28:37.6	60	R	M92
170xxx.fits	14:31:07.9	0	NA	Bias
171xxx.fits	04:30:12.3	0	NA	Bias
172xxx.fits	04:30:12.3	0	NA	Bias
173xxx.fits	04:30:12.3	0	NA	Bias

Table 8 May 3/4 1984 Observations (Continued)

Image	UT	Exposure	Filter	Target
174xxx.fits	04:30:12.3	0	NA	Bias
185xxx.fits	04:30:12.3	0	NA	Bias
186xxx.fits	04:30:12.3	0	NA	Bias
187xxx.fits	04:30:12.3	0	NA	Bias
188xxx.fits	04:30:12.3	0	NA	Bias
189xxx.fits	04:30:12.3	1	B	flat
191xxx.fits	04:30:12.3	90	B	flat
192xxx.fits	04:30:12.3	90	B	flat
193xxx.fits	04:30:12.3	90	B	flat
194xxx.fits	04:30:12.3	90	B	flat
195xxx.fits	04:30:12.3	60	R	flat
196xxx.fits	04:30:12.3	60	R	flat
197xxx.fits	04:30:12.3	60	R	flat
198xxx.fits	04:30:12.3	60	R	flat
199xxx.fits	04:30:12.3	900	NA	Dark
200xxx.fits	04:30:12.3	900	NA	Dark
201xxx.fits	04:30:12.3	900	NA	Dark
202xxx.fits	04:30:12.3	900	NA	Dark
203xxx.fits	04:30:12.3	900	NA	Dark
204xxx.fits	04:30:12.3	900	NA	Dark
205xxx.fits	04:30:12.3	900	NA	Dark
206xxx.fits	04:30:12.3	900	NA	Dark
223xxx.fits	04:30:12.3	0	NA	Bias
224xxx.fits	04:30:12.3	0	NA	Bias
225xxx.fits	04:30:12.3	0	NA	Bias
226xxx.fits	04:30:12.3	0	NA	Bias
227xxx.fits	04:30:12.3	900	NA	Dark
228xxx.fits	04:30:12.3	60	R	Flat
229xxx.fits	04:30:12.3	60	R	Flat
230xxx.fits	04:30:12.3	60	R	Flat
231xxx.fits	04:30:12.3	90	B	Flat
232xxx.fits	04:30:12.3	90	B	Flat
233xxx.fits	04:30:12.3	90	B	Flat
234xxx.fits	04:30:12.3	10	B	Flat

Table 13: Night 2, May 4/5 1984

Image	UT	Exposure	Filter	Target
235xxx.fits	04:30:12.3	60	B	Flat
237xxx.fits	06:34:10.8	60	B	NGC4147
238xxx.fits	06:41:35.6	120	B	NGC4147
239xxx.fits	06:46:45.4	120	R	NGC4147
246xxx.fits	04:30:12.3	0	NA	Bias
247xxx.fits	04:30:12.3	0	NA	Bias
248xxx.fits	08:36:21.0	120	B	NGC4147
249xxx.fits	08:41:02.1	120	R	NGC4147
250xxx.fits	04:30:12.3	900	B	Dark
253xxx.fits	09:21:41.6	60	R	M92
254xxx.fits	09:28:03.6	60	B	M92
255xxx.fits	09:34:04.8	1200	B	NGC6166
256xxx.fits	10:01:24.8	120	B	NGC6166
257xxx.fits	10:04:57.2	1200	B	NGC6166
258xxx.fits	10:27:35.0	1200	B	Sky1
259xxx.fits	10:49:00.2	900	R	Sky1
260xxx.fits	11:07:20.5	900	R	NGC6166
261xxx.fits	04:30:12.3	0	NA	Bias
262xxx.fits	11:29:19.6	120	R	NGC4147
263xxx.fits	11:33:40.9	120	B	NGC4147
264xxx.fits	04:30:12.3	0	NA	Bias
265xxx.fits	11:48:17.6	120	B	NGC6166
266xxx.fits	11:54:42.5	1200	B	Halo
267xxx.fits	12:18:31.8	1443	B	Sky2
268xxx.fits	12:46:33.0	900	R	Halo
269xxx.fits	13:05:09.9	900	R	Sky2
270xxx.fits	04:30:12.3	0	NA	Bias
271xxx.fits	13:26:26.0	60	R	M92
272xxx.fits	13:30:02.1	60	R	M92
273xxx.fits	13:32:42.5	60	B	M92
274xxx.fits	04:30:12.3	0	NA	Bias
275xxx.fits	13:38:51.3	120	B	NGC6166
276xxx.fits	13:44:07.0	1200	B	Halo

Table 9 May 4/5 1984 observations (continued)

Image	UT	Exposure	Filter	Target
277xxx.fits	14:40:10.2	1200	B	Sky2
278xxx.fits	14:30:40.2	60	B	M92
279xxx.fits	14:33:23.9	60	B	M92
280xxx.fits	14:38:12.9	30	R	M92
281xxx.fits	14:40:18.6	30	B	M92
282xxx.fits	04:30:12.3	0	NA	Bias
283xxx.fits	04:30:12.3	0	NA	Bias
284xxx.fits	04:30:12.3	90	B	Flat
285xxx.fits	04:30:12.3	90	B	Flat
286xxx.fits	04:30:12.3	90	R	Flat
287xxx.fits	04:30:12.3	60	R	Flat
288xxx.fits	04:30:12.3	60	R	Flat
289xxx.fits	04:30:12.3	60	R	Flat
290xxx.fits	04:30:12.3	900	B	Dark
291xxx.fits	04:30:12.3	900	B	Dark
292xxx.fits	04:30:12.3	900	B	Dark
293xxx.fits	04:30:12.3	900	B	Dark

Table 14: Detailed information on CFHT Archive data

Image	Filter	Exposure (seconds)	Date DD/MM/YY	Target
112544b		0.0	16/04/91	Bias
112545b		0.0	16/04/91	Bias
112546b		0.0	16/04/91	Bias
112547b		0.0	16/04/91	Bias
112548b		0.0	16/04/91	Bias
112549b		0.0	16/04/91	Bias
112550b		0.0	16/04/91	Bias
112551b		0.0	16/04/91	Bias
112552b		0.0	16/04/91	Bias
112553b		0.0	16/04/91	Bias
112554b		0.0	16/04/91	Bias
112592o	V	30.0	16/04/91	Focus
112608o	V	300.0	16/04/91	NGC6166
112610o	V	60.0	16/04/91	NGC6166
112611o	V	300.0	16/04/91	Sky Flat
112612o	V	120.0	16/04/91	Sky Flat
112611o	V	300.0	16/04/91	Sky Flat
112619b		0.0	16/04/91	Bias
112620b		0.0	16/04/91	Bias
112621b		0.0	16/04/91	Bias
112622b		0.0	16/04/91	Bias
112623b		0.0	16/04/91	Bias
116430Bb		0.0	06/06/91	Median 20 Bias
116442F	R	7.0	06/07/91	Median 10 Dome Flats
116448F	B	10.0	06/07/91	Median 10 Dome Flats
116459F	B	10.0	06/07/91	Median 10 Dome Flats
116612o	R	30.0	06/07/91	NGC6166
116613o	R	600.0	06/07/91	NGC6166
116614o	B	1200.0	06/07/91	NGC6166
116706Bo		0.0	06/07/91	Median 20 Bias
116727Bo		0.0	06/07/91	Median 20 Bias

10 Appendix B

Standard Star Data

Table 15 and 16 present the magnitudes of the standard stars in the Cousins photometric system.

Table 15: M92 Standard Star Data

Star	V	B-V	V-R
M92-1	13.078 ± 0.012	0.612 ± 0.016	0.257 ± 0.060
M92-2	14.579 ± 0.014	0.800 ± 0.021	0.485 ± 0.009
M92-3	14.694 ± 0.019	0.788 ± 0.033	0.485 ± 0.017
M92-4	14.618 ± 0.014	0.783 ± 0.019	0.486 ± 0.014
M92-5	16.052 ± 0.009	0.534 ± 0.016	0.313 ± 0.008
M92-6	16.331 ± 0.021	-0.112 ± 0.018	-0.038 ± 0.010
M92-7	16.437 ± 0.020	-0.112 ± 0.016	-0.041 ± 0.010
M92-8	15.932 ± 0.021	0.574 ± 0.030	0.351 ± 0.015
M92-9	16.986 ± 0.010	1.146 ± 0.012	0.722 ± 0.008
M92-10	14.036 ± 0.010	0.798 ± 0.026	0.516 ± 0.014
M92-11	15.146 ± 0.023	1.025 ± 0.018	0.630 ± 0.020
M92-12	15.982 ± 0.027	0.637 ± 0.072	0.433 ± 0.013
M92-13	15.078 ± 0.018	0.589 ± 0.022	0.360 ± 0.015
M92-14	14.311 ± 0.011	0.590 ± 0.030	0.372 ± 0.006
M92-15	17.153 ± 0.009	0.629 ± 0.029	0.396 ± 0.019
M92-16	15.264 ± 0.018	0.107 ± 0.034	0.058 ± 0.017
M92-17	14.475 ± 0.000	0.567 ± 0.028	0.403 ± 0.016
M92-18	17.966 ± 0.012	0.488 ± 0.027	0.320 ± 0.005
M92-19	18.211 ± 0.017	0.415 ± 0.018	0.286 ± 0.018
M92-20	18.047 ± 0.041	0.878 ± 0.029	0.494 ± 0.047
M92-21	17.925 ± 0.009	0.497 ± 0.007	0.340 ± 0.009
M92-22	17.542 ± 0.015	0.550 ± 0.017	0.357 ± 0.017
M92-23	16.791 ± 0.023	0.636 ± 0.015	0.403 ± 0.006

Table 16: NGC 4147 Standard Star Data

Star	V	I	B-V	R-I
6	16.783 ± 0.030	15.811 ± 0.016	0.810 ± 0.000	0.490 ± 0.015
9	18.263 ± 0.022	17.407 ± 0.093	0.706 ± 0.037	0.426 ± 0.030
11	16.795 ± 0.017	15.824 ± 0.049	0.783 ± 0.012	0.489 ± 0.019
12	17.708 ± 0.077	16.290 ± 0.022	1.055 ± 0.035	0.650 ± 0.040
14	17.424 ± 0.024	17.457 ± 0.016	0.000 ± 0.000	0.068 ± 0.014
15	16.651 ± 0.015	16.386 ± 0.018	0.163 ± 0.020	0.187 ± 0.029

11 Appendix C

The Procedure for Sky Determination

As seen in Section 4.1, the sky brightness is not constant. This indicates that the sky value on the NGC 6166 images must be estimated from the images themselves. Here a problem arises. The envelope of NGC 6166 is large, (Oemler 1976) and contributes to the brightness values in every pixel of the image. The images contain no true sky region.

We adopt as the sky region the last 50 rows of each image. This region was selected because it is the region furthest from NGC 6166. In each image this region was cleaned of hot pixels and cosmic rays. Cosmetic defects, background stars and galaxies were then masked out. The mean of the counts in the sky region was then computed. To check that the mean was a good statistic for the sky region value, histograms were plotted of the values inside the region. In all cases the peak of the histogram was indistinguishable from the mean. To determine the contribution of the galaxy to any pixel, we need knowledge of how the brightness of the galaxy changes with distance from the center. The geometry is shown in Figure 30.

We assume that the isophotes of the main galaxy have constant position angle (PA) and ellipticity. The true brightness of the cD at semi-major axis position A_1 is B_1 . The cD brightness is B_2 at semi-major axis position A_2 , which lies on the isophote containing the center of the sky region. The center of the sky region is at angle θ from the major axis and distance r from the center of the galaxy. For elliptical isophotes we have in polar coordinates:

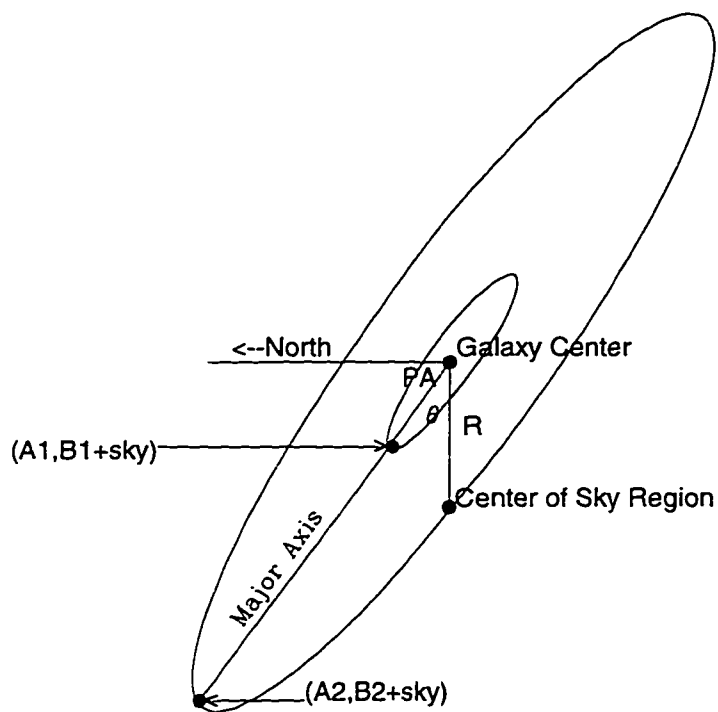


Figure 26: The geometry used for the determination of the galaxy contribution to the sky value. The position (r, θ) of the sky region with respect to the center is known, giving the semi-major axis distance A_2 using equation 9. Knowing the galaxy surface brightness at A_1 and A_2 , from Oemler (1978), and the instrumental brightness at both points, the contribution of the halo to the counts at the center of the sky region may be found. B_1 , and B_2 are the sky intensities at A_1 and A_2 respectively in ADU.

$$r^2 = \frac{a^2 b^2}{a^2 \sin^2 \theta + b^2 \cos^2 \theta} \quad (19)$$

Here a is the major axis length and b is the minor axis length. The major to minor axis ratio is defined as

$$\epsilon = b/a \quad (20)$$

Solving for b and substituting into equation 8 we get :

$$r^2 = \frac{a^2 \epsilon^2}{a^2 (\sin^2 \theta + \epsilon^2 \cos^2 \theta)} \quad (21)$$

Solving for the semi-major axis position a , corresponding to the position (r, θ) :

$$a = \left(\frac{r}{\epsilon}\right) \sqrt{\sin^2 \theta + \epsilon^2 \cos^2 \theta} \quad (22)$$

The position along the major axis of the point corresponding to the center of the sky region may then be determined from Equation 11. Table 12 gives the radii, θ and semimajor axis position, in kiloparsecs, corresponding to the center of the sky region. Since we wished to use the surface brightness data of Oemler (1976) to estimate the galaxy contributions, the semimajor axis values are converted to kiloparsecs, assuming a distance of 187 Mpc for NGC 6166 (Oemler 1976). To use Oemler's plot, it must be noted that he defines $r = \sqrt{ab}$, where a and b are the minor and major axis lengths. I give this the symbol R_o in Table 12.

The geometry of Figure 30 indicates the brightness of the galaxy at point A_1 , close to the nucleus, is given by B_1 . At A_2 , the corresponding brightness is B_2 . From

Table 17: Sky Region Semi-Major Axis Positions

Image	Radius (Kpc)	θ (Degrees)	A_2 (Kpc)	R_o (Kpc)
161	153.795	55.22	569.461	284.730
164	151.901	53.62	557.597	278.799
255	129.941	70.55	510.255	255.128
257	135.922	55.86	504.999	252.500
260	141.277	50.85	510.166	255.083

Oemler's data we know the surface brightness in magnitudes per unit area, M_1 and M_2 at these points then:

$$M_1 - M_2 = 2.5 \log(B_2/B_1). \quad (23)$$

The ratio of the galaxy brightness at A_2 to that of A_1 is C and is given by:

$$C = B_2/B_1 = 10^{0.4(M_1 - M_2)} \quad (24)$$

The total brightness in ADU at A_1 and A_2 , are B_{t1} and B_{t2} and are given by:

$$B_{t1} = B_1 + S \quad (25)$$

$$B_{t2} = B_2 + S \quad (26)$$

Where S represents the true sky brightness for the image. From equation 25 and solving for B_1 using equation 24 we get:

$$B_1 = \frac{B_{t1} - B_{t2}}{1 - C} \quad (27)$$

Solving equation 25 for the sky:

$$S = B_{t1} - B_1 \quad (28)$$

Substituting our expression for B_1 from equation 27 into equation 28 we get an expression for the sky in terms of known quantities:

$$S = B_{t1} - \frac{B_{t1} - B_{t2}}{1 - C} \quad (29)$$

B_{t1} and B_{t2} are determined directly from the NGC 6166 frames in ADU. If $B - V$ and $B - R$ values are assumed constant the ratio of the brightness at A_1 and A_2 is the same in the V , B and R passbands. This allows the V -band surface photometry of Oemler (1976) to be used to compute C . With C , B_{t1} and B_{t2} known, the sky brightness is computed from equation 29.

To determine the correct major-to-minor axis ratio, and position angle, SNUC multiple nucleus fits were performed on the images (see Section 3.3). These fits gave the run of brightness in ADU as a function of semi-major axis distance, the position angles and ellipticities. A position angle of 30° , and an ellipticity of 0.20 were adopted, giving $\epsilon = 0.80$.

The sky values for the frames are listed in Table 18. The first column gives the image number, the second column gives the semi-major axis distance in kiloparsecs, the third column gives the surface brightness in magnitudes per square arcsecond

Table 18: Adopted Sky Values

Image	R_o (kpc)	M_1	M_2	C	B_{t1} (ADU)	B_{t2} (ADU)	Sky (ADU)
(1)	(2)	(3)	(4)	(5)	(6)	(7)	(8)
161	284.730	19.79	26.95	1.36E-3	3575	710.26	706.4
164	278.799	19.79	26.84	1.51E-3	1725	252.17	249.9
255	255.128	19.79	26.80	1.57E-3	1562	236.56	234.5
257	252.500	19.79	26.74	1.66E-3	1543	216.10	213.9
260	255.083	19.79	26.80	1.57E-3	3396	516.55	512.6

at the inner isophote. This is adopted as the innermost point on Oemler's profile, which is at $3''6$. Column four gives the surface brightness in magnitudes per square arcsecond from Oemler at the sky region, column five gives C , column six gives B_{t1} , column seven gives B_{t2} , and column eight gives the adopted sky value. The adopted sky values were subtracted from the respective NGC 6166 images, which were then ready for final SNUC profile fitting.

Curriculum Vitae

R. Melvin Blake

Personal Information

Name: Ronald Melvin Blake

SIN Number: 121 137 194

Date of Birth: May 12, 1968.

Phone Number (Home): 422-8483. (Office): 496-8769.

Permanent Address: 109 Midland row, Pasadena, Newfoundland. A0L 1K0

Current Address: Apt. 412, 6 Assiniboine Road, York University, North York,
Ontario, M3J 1L3

Education:

B. Sc. (Physics Conc.) April, 1991

Saint Mary's University

Halifax, Nova Scotia

B3H 3C3

Relevant Work Experience

Employer	Dates of Employment	Duties
Astronomy & Physics Dept. St. Mary's U. Halifax, Nova Scotia.	Sept 1994 - April 1995 Sept 1995 - April 1996	Telescope operator for 40 cm telescope. Marked introductory Physics labs.
Dr. P. Bergbusch University of Regina Physics Dept.	May 1994-Aug 1994 June 1995 - Aug 1995	Crowded Field Photometry of NGC 362, M55. Upgraded Telescope dome.
Chemistry Department St. Mary's U. Halifax, Nova Scotia.	Sept 1990 - April 1991 Sept 1991 - April 1992 Sept 1992 - April 1993 Sept 1994 - April 1995	Lab demonstrator for introductory Chemistry labs.
Astronomy Department St. Mary's U. Halifax, Nova Scotia.	June 1990 - July 1990 Sept 1990 - Dec 1990	Telescope operator for introductory astronomy.
Physics Department St. Mary's U. Halifax, Nova Scotia.	Sept 1990 - April 1991	Introductory lab demonstrator.